DYNAMIC DEFORMATION AND TEMPERATURE FIELD MEASUREMENT OF METALLIC MATERIALS

by

Yizhou Nie

A Dissertation

Submitted to the Faculty of Purdue University

In Partial Fulfillment of the Requirements for the degree of

Doctor of Philosophy

School of Aeronautics and Astronautics

West Lafayette, Indiana

December 2019

THE PURDUE UNIVERSITY GRADUATE SCHOOL
STATEMENT OF COMMITTEE APPROVAL

Dr. Weinong Chen, Chair
School of Aeronautics and Astronautics
School of Materials Engineering

Dr. Terrence Meyer
School of Mechanical Engineering

Dr. Michael Sangid
School of Aeronautics and Astronautics

Dr. Wenbin Yu
School of Aeronautics and Astronautics

Approved by:
Dr. Gregory Blaisdell

To Yicheng Z.,

Without whom I would not have determined to become a Ph.D..

ACKNOWLEDGMENTS

This dissertation was possible thanks to the participation and assistance of so many people whose names may not all be enumerated. First and foremost, I would like to express my gratitude to my major advisor Dr. Weinong Chen for the constant source of knowledge and support. Furthermore I would like to thank Prof. Terrence Meyer, Prof. Michael Sangid, and Prof. Wenbin Yu for their constructive feedbacks on this research project and serving as my committee members. I also want to sincerely thank Dr. Tao Sun, Dr. Kamel Fezzaa, Dr. Xianghui Xiao and Aaron Greco from Argonne National Laboratory for their professional help with our X-ray beam time and infrared experiments in this research, the funding supported from the U. S. Army Research Laboratory (ARL) and the U. S. Army Research Office (ARO).

Last but not least, I would like to thank all of my colleagues from Impact Science Laboratory and Zucrow Laboratory, especially Zach Ayers and Alex Brown for their knowledge of laser techniques and unreserved support during our late night experiments in the test cell, Dr. Hangjie Liao, Dr. Boon Him Lim, Dr. Ben Claus and Dr. Jou-Mei Chu for their willingness to help me with the experimental setup and data analysis which were essential for the completion of this dissertation, Dr. Niranjan Parab, Dr. Waterloo Tsutsui, Zherui Guo, Xuedong Zhai, Nesredin Kedir, Jinling Gao, and Shane Paulson for their time to give me precious advice that helped my work go smoothly.

TABLE OF CONTENTS

LIST OF TABLES 7
LIST OF FIGURES 8
ABSTRACT 12
1. INTRODUCTION 13
1.1 Adiabatic shear band 13
1.2 High-speed temperature measurement techniques 20
1.3 Phosphor thermometry 26
1.4 Objectives and research approach 31
2. IN SITU OBSERVATION OF ADIABATIC SHEAR BAND FORMATION 33
2.1 Materials and Methods 33
2.1.1 Materials and specimens 33
2.1.2 Kolsky bar 34
2.1.3 High speed synchrotron X-ray phase contrast imaging 37
2.1.4 Infrared thermal imaging 38
2.2 Experimental Results 40
2.2.1 Aluminum 7075-T6 40
2.2.2 Aluminum 6061-T6 44
2.3 Discussion 48
2.4 Summary 51
3. DYNAMIC TEMPERATURE EVOLUTION USING LASER PHOSPHORESCENCE THERMAL IMAGING: LIFETIME METHOD 52
3.1 Experimental Methods 52
3.1.1 Specimen preparation 52
3.1.2 Phosphor thermography 53
3.1.3 Dynamic loading with laser phosphorescence thermal imaging 55
3.1.4 Temperature calibration and image processing 57
3.1.5 Image processing 58
3.2 Experimental Results 59

3.3 Discussion 63
3.4 Summary 65
4. DYNAMIC TEMPERATURE EVOLUTION USING LASER PHOSPHORESCENCE THERMAL IMAGING: INTENSITY RATIO METHOD 67
4.1 Materials and Methods 67
4.1.1 Materials and specimens 67
4.1.2 Phosphor thermography 69
4.1.3 Synchronization of the Kolsky bar and the laser phosphorescence thermal imaging 70
4.1.4 Temperature calibration 72
4.1.5 Image processing 75
4.2 Dynamic Compression of Copper 76
4.2.1 Experimental results 76
4.2.2 Discussion 79
4.3 Dynamic Shear of Aluminum Alloys 80
4.3.1 Experimental results 80
4.3.2 Discussion 84
4.4 Summary 90
5. FUTURE WORKS 91
6. CONCLUSION 96
REFERENCES 98
PUBLICATIONS 105

LIST OF TABLES

Table 1.1. The response time of type-J thermocouples reported by OMEGA [24]..... 21
Table 2.1 Dimensions of the hat-shaped specimen (mm)..... 34
Table 4.1 Material properties of C101 copper..... 68

LIST OF FIGURES

Figure 1.1. Adiabatic shear band and an associated crack during dynamic compression of a martensitic steel. Reproduced from [3]..... 14

Figure 1.2. Deformation and failure process of tungsten fiber/metallic glass composite rod and steel target under the penetration. Reproduced from [4] 15

Figure 1.3. The geometry of a steel specimen for use in a torsional Kolsky bar [8]. 16

Figure 1.4. A stress-strain curve showing the three stages of plastic deformation in Figure 1.5. Reproduced from [8]..... 16

Figure 1.5. Grid patterns on the specimen showing the deformation corresponding to the three stages. Reproduced from [8]. 17

Figure 1.6. The polymer specimen with the embedded thermocouple used in [26]. 21

Figure 1.7. Temperature rise and strain gage signals for a polycarbonate. Reproduced from [26]. 22

Figure 1.8. A schematic representation of the high speed infrared detector array focused on a specimen in a Kolsky bar [13]. 24

Figure 1.9. Calibration of infrared detectors with steel for different surface finishes. Reproduced from [13]. 25

Figure 1.10. Classification of different methods of phosphor thermometry [33]. 26

Figure 1.11. Intensity decay of La_2O_2S:Eu phosphor [35]. 27

Figure 1.12. 100 kHz pixel intensity history of La_2O_2S:Eu phosphor at 260 °C [35]. 28

Figure 1.13. Normalized BAM:Eu emission spectral. Reproduced from [49]. 30

Figure 1.14. The experimental setup used by Abram *et al.* [49]. 30

Figure 2.1. The geometry of hat-shaped specimen and the compression-shear region 34

Figure 2.2. A schematic of the compression Kolsky bar setup..... 35

Figure 2.3. A photograph of the specimen section of the Kolsky bar setup 35

Figure 2.4. Dynamic compression setup with high-speed X-ray phase contrast imaging..... 37

Figure 2.5. A photograph of experimental setup of high-speed infrared camera and Kolsky bar.39

Figure 2.6. The true temperature–emissivity relationships at radiance temperature of 450 K and 480 K..... 39

Figure 2.7. (a) The force-time graph and (b) the corresponding image sequence of a representative dynamic shear experiment on aluminum 7075-T6. Lines are tracked and marked to show the shear deformation. 41

Figure 2.8. A representative force-time relationship and the corresponding thermal image sequences of aluminum 7075-T6. (a) The location of the camera window. (b) The force-time graph. (c) The thermal image sequence showing the temperature field on the material surface. 43

Figure 2.9. The force-displacement curves of aluminum 7075-T6. 43

Figure 2.10. (a) The force-time graph and (b) the corresponding image sequence of a representative dynamic shear experiment on aluminum 6061-T6. Lines are tracked and marked to show the shear deformation. 45

Figure 2.11. A representative force-time relationship and the corresponding thermal image sequences of aluminum 6061-T6. (a) The location of the camera window. (b) The force-time graph. (c) The thermal image sequence showing the temperature field on the material surface. 46

Figure 2.12. The force-displacement curves of aluminum 6061-T6. 47

Figure 2.13. Temperature distribution in aluminum 7075-T6 at different time after the adiabatic shear band formation. *d* is half of the shear band width. 49

Figure 2.14. A detailed view of the temperature distribution in aluminum 7075-T6 at 10 μs and 100 μs after the adiabatic shear band formation. *d* is half of the shear band width. 49

Figure 3.1. Excitation spectra of the (a) 594 nm, (b) 616 nm, (c) 624 nm and (d) 704 nm emission lines of La_2O_2S:Eu [65]. 54

Figure 3.2. Fluorescence decay time vs temperature for La_2O_2S:Eu. Reproduced from [34] 54

Figure 3.3. Kolsky bar setup with high-speed laser phosphorescence thermal imaging. 56

Figure 3.4. A photograph showing the laser and imaging system setup with Kolsky bar. 57

Figure 3.5. The setup for temperature calibration of lifetime method. 58

Figure 3.6. A typical experimental record showing strain gage, load cell and laser signals. 59

Figure 3.7. A representative force-time relationship of aluminum 7075-T6. 60

Figure 3.8. A representative force-displacement relationship of aluminum 7075-T6. 60

Figure 3.9. A representative temperature field image sequences of aluminum 7075-T6. (a) The location of the camera window. (b) The thermal image sequence showing the temperature field. 62

Figure 3.10. The rotation of the rotor causes the fluorescing spot to move with respect to the fluorescence collection fiber's input aperture. Reproduced from [37]. 64

Figure 3.11. Qualitative oscilloscope signals of the fluorescence intensity from a stationary phosphor target and from the rotating target. Reproduced from [37]. 64

Figure 4.1. A microscopic image showing the phosphor coating layer. 68

Figure 4.2. A schematic and a photograph showing the image doubler 69

Figure 4.3. Dynamic compression setup with high-speed laser phosphorescence thermal imaging. 70

Figure 4.4. A photograph of compression Kolsky bar setup for laser phosphorescence thermal imaging. 71

Figure 4.5. The timing sequence of the Kolsky bar experiment with laser phosphorescence. 72

Figure 4.6. Calibration curve acquired at 93 μJ/cm^2 with a 4 μs camera exposure. 73

Figure 4.7. Ratio measurements at different average pulse fluence levels. 74

Figure 4.8. Ratio measurements using different camera exposures and constant pulse fluence. . 74

Figure 4.9. A representative image used for image registration. 75

Figure 4.10. A typical experimental record showing strain gage, load cell and camera frame signals. 76

Figure 4.11. A representative sequence of raw images captured from the high-speed camera. ... 77

Figure 4.12. A representative image sequence of the temperature field of copper during dynamic compression. 78

Figure 4.13. A representative force – time relationship of copper during dynamic compression. The time is in accordance with the high-speed images. 78

Figure 4.14. The average temperature history inside the boxed area shown in Figure 4.12 78

Figure 4.15. Temperature – time history of the thermocouple attached to the copper during a dynamic compression experiment. 80

Figure 4.16. A representative sequence of raw images showing material deformation and phosphorescence of 7075-T6 81

Figure 4.17. A representative force-time relationship and the corresponding thermal image sequences of aluminum 7075-T6. (a) The location of the camera window. (b) The force-time graph. (c) The thermal image sequence showing the temperature field evolution. 82

Figure 4.18. A representative sequence of raw images showing material deformation and phosphorescence of 6061-T6 83

Figure 4.19. A representative force-time relationship and the corresponding thermal image sequences of aluminum 6061-T6. (a) The location of the camera window. (b) The force-time graph. (c) The thermal image sequence showing the temperature field evolution. 84

Figure 4.20. The three stages of transient thermal conduction with an increasing T_0. 86

Figure 4.21. A scanning electron microscopic image showing the phosphor coating on an aluminum specimen 87

Figure 4.22. The average temperature – time history of aluminum 7075-T6 in the boxed area shown in Figure 4.17 (a) before the temperature correction. (b) after the temperature correction. 88

Figure 4.23. The average temperature – time history of aluminum 6061-T6 in the boxed area shown in Figure 4.19 (a) before the temperature correction. (b) after the temperature correction. 89

Figure 5.1. A microscopic image showing the size distribution of BAM:Eu phosphor particles. 91

Figure 5.2. Synthesis process of nano-sized BAM:Eu phosphor..... 92

Figure 5.3. A TEM image and morphology of the BAM:Eu annealed at 1200 °C [70]..... 93

Figure 5.4. Temperature rise vs time at outside surface of the phosphor with different coating thickness, given T_0 = 700 K at t = 0 and room temperature T_s = 300 K. 94

Figure 5.5. A detailed view of the Temperature rise vs time at outside surface of the phosphor with different coating thickness, given T_0 = 700 K at t = 0 and room temperature T_s = 300 K..... 95

ABSTRACT

In this dissertation, we first used high-speed X-ray phase contrast imaging and infrared thermal imaging techniques to study the formation processes of adiabatic shear bands in aluminum 7075-T6 and 6061-T6 alloys. A modified compression Kolsky bar setup was developed to apply the dynamic loading. A flat hat-shaped specimen design was adopted for generating the shear bands at the designated locations. Experimental results show that 7075-T6 exhibits less ductility and a narrower shear band than 6061-T6. Maximum temperatures of 720 K and 770 K were locally determined within the shear band zones for 7075-T6 and 6061-T6 respectively. This local high temperature zone and the resulting thermal instability were found to relate to the shear band formation in these aluminum alloys. Secondly, a high-speed laser phosphorescence thermal imaging technique is developed and integrated with the compression Kolsky bar setup. The temperature field measurement during dynamic loading are performed at 100 – 200 kHz frame rate with a spatial resolution of 13 μm/pixel. The dynamic compression of copper shows 312 K temperature rise among the material surface. Experiments with thermocouple are also conducted and the results verifies the laser measurement. In the dynamic shear of aluminums, the temperature evolution during adiabatic shear band formation was observed and the results are compared with infrared measurements. The shear band was found forming at approximately 400 K and 440 K for 7075-T6 and 6061-T6, respectively, while the maximum temperature is measured as 650 K for 7075-T6 and 800 K for 6061-T6. Although the maximum temperature agrees with the infrared results, thermal softening is not considered as the main cause of the ASB formation due to the low temperature when the shear band forms.

1. INTRODUCTION

Adiabatic shear banding is a critical energy dissipation mechanism in materials under impact. However, the fundamental mechanisms are still not well understood. Due to the limitations in experimental methods, the dynamic deformation field and the associated temperature field have not been investigated in real time at high spatial resolutions. In this chapter, the previous research work on adiabatic shear band formation and high-speed temperature measurement techniques will be reviewed. The basics of phosphor thermometry will be introduced. Finally, the current challenges and limitations on the high-speed deformation and temperature field measurement will be identified.

1.1 Adiabatic shear band

When subject to dynamic loading, many materials frequently exhibit localized shear deformation. This intense shearing is localized in a narrow band of highly deformed material, associated with local temperature rise resulting from plastic deformation accumulation over a short time, which is called an adiabatic shear band (ASB). The adiabatic shearing is first introduced by Zener and Hollomon [1], which indicates that the thermal softening dominates over the effect of strain hardening. The mechanism that results in shear band formation is considered as a local thermo-mechanical instability of the material. During plastic deformation, the plastic work is mainly converted into heat over a very short time period, leading to temperature increase within the material. If localized deformation at a high rate exists, thermal softening becomes locally significant. Under dynamic deformation, the heat dissipation is not fast enough and thermal softening will dominate over the effect of work hardening. Therefore, the deformation becomes unstable and will grow within a narrow band forming the ASB [2].

Although an ASB is not a crack, it is closely related to the initiation of cracks and can further result in catastrophic material failure during dynamic loading. Figure 1.1 shows an example of an ASB in martensitic steel, which is observed by Dormeval and Stelly [3] in 1981. The researchers conducted dynamic compression experiments on martensitic steel specimens with different hardness. The strain rate was reported as 2700 /s. In the experiment, the loading was controlled to stop just before the overall rupture of the material, offering the opportunity to

examine the adiabatic shear bands. In the particular specimen shown, the shear band can be seen about 45° to the loading axis. The white color indicates martensite forms within the ASB, which is called transformed band. A crack is propagating along the same track of the shear band from the upper right corner, but has not cause the catastrophic failure of the entire specimen.

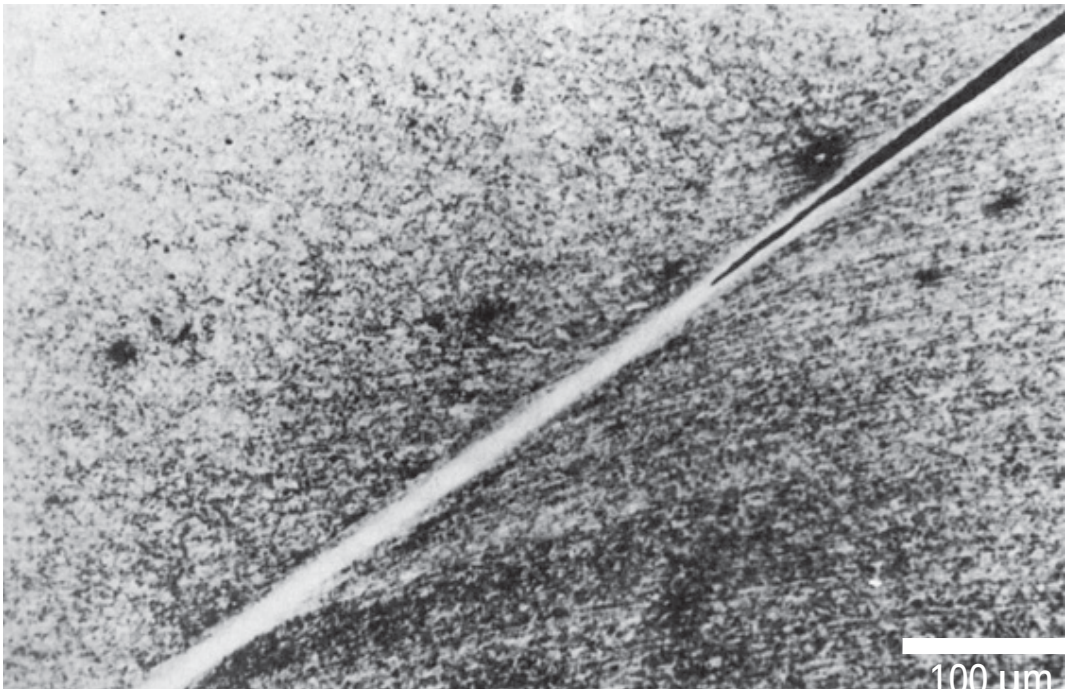

Figure 1.1. Adiabatic shear band and an associated crack during dynamic compression of a martensitic steel. Reproduced from [3]

There are also applications where controlled shear bands are desired. Li *et al.* [4] performed FEM study on the penetration behaviors of tungsten fiber / metallic glass (WF/MG) composite rod into steel target, as shown in Figure 1.2. During the penetration, there is an edge layer forming in the front of the projectile. The matrix of MG fails earlier than the WFs, causing the pre-deformation of the surrounding WFs. As the projectile moves forward, the nose exhibits localized shear deformation around it and some materials separate from the projectile after fracture, leading to the formation of a new sharp nose. This self-sharpening process continues and repeats itself, remarkably improving the penetration performance of the projectile.

Figure 1.2. Deformation and failure process of tungsten fiber/metallic glass composite rod and steel target under the penetration. Reproduced from [4]

In the past decades, the formation of ASB has been found in many metals, including steel, titanium alloys, aluminum and aluminum alloys. Numerous efforts have been undertaken to determine the critical conditions under which ASB forms, as documented by reviews and books, such as Timothy [5], Xu *et al*. [6] and Dodd and Bai [7]. However, most of the early studies are based on the post-mortem experimental observations that are after the shear band formation. It is until the use of high-speed imaging techniques with the dynamic loading setup that the ASB formation is observed in real time. Marchand and Duffy [8] conducted dynamic torsional experiments on a low alloy structural steel HY-100 using a torsional Kolsky bar setup. The specimen geometry is shown in Figure 1.3. The advantage to study ASB formation with torsional experiments is that the specimen is only under a pure shear stress state in a designated area. As illustrated in Figure 1.4, the researchers showed three distinct stages of the plastic deformation of the specimen. The grid patterns represent each stage are presented in Figure 1.5. Stage 1 is homogenous deformation up to 23% of strain. All the grid lines can be seen deforming with uniform slopes. Stage 2 is inhomogeneous deformation with curved lines presenting. Stage 3 represents the ASB. The lines are discontinuous in the middle, indicating the existence of highly localized shear deformation. In this stage, the stress starts to drop rapidly. A set of infrared detectors were also used in this study to capture the temperature rise. Results showed that within the shear band, the maximum recorded temperature rise was 590 °C.

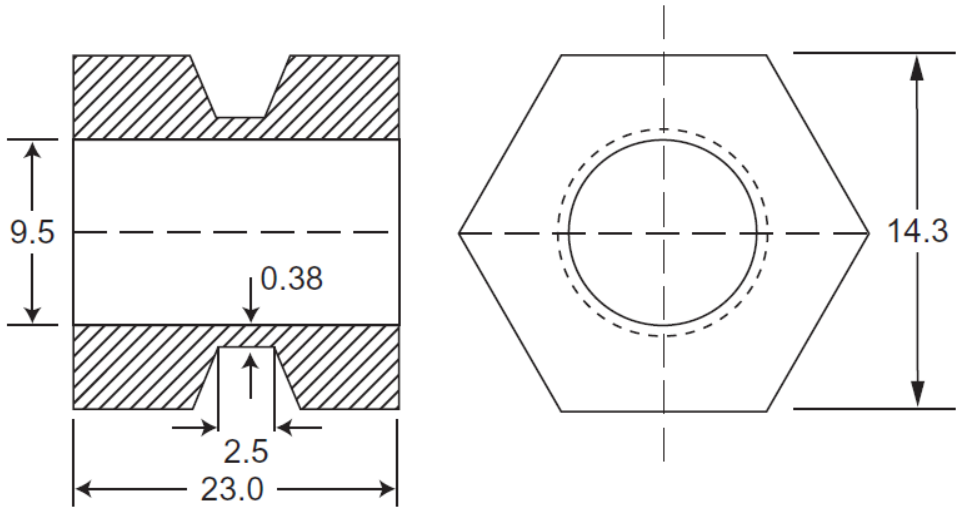

Figure 1.3. The geometry of a steel specimen for use in a torsional Kolsky bar [8].

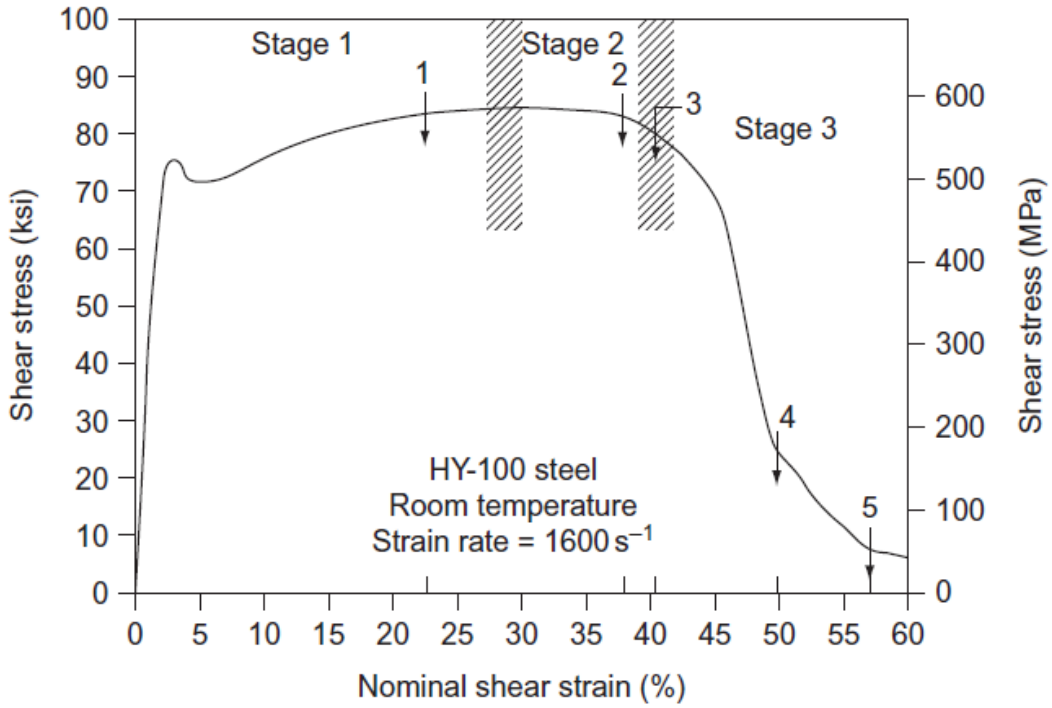

Figure 1.4. A stress-strain curve showing the three stages of plastic deformation in Figure 1.5. Reproduced from [8].

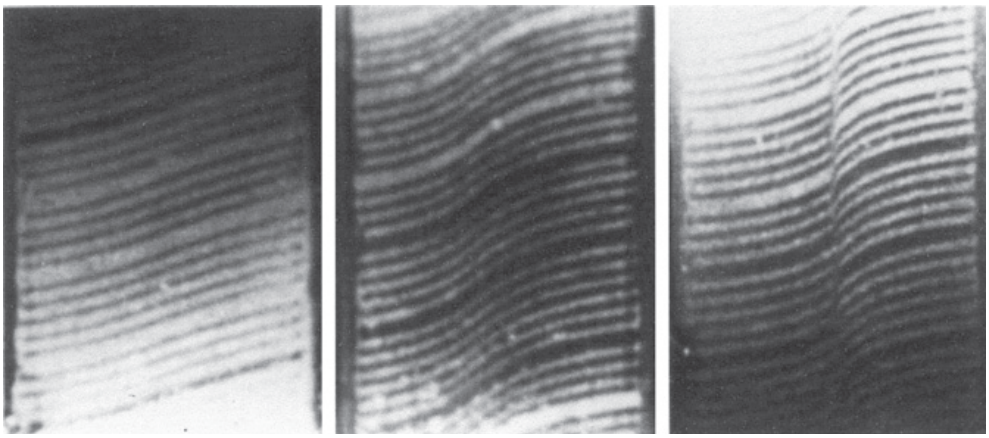

Stage 1 Stage 2 Stage 3

Figure 1.5. Grid patterns on the specimen showing the deformation corresponding to the three stages. Reproduced from [8].

Besides steel, ASB are also reported in aluminum and its alloys. The latter are widely used as structural materials in aerospace industries due to their light weight and design flexibility. Aluminum plates are also used in armor design as protective layers [9]. In these applications, the materials are commonly subjected to impact loading. The involved shear banding behavior can be a significant concern for structural integrity under dynamic loading conditions. Early experimental approaches regarding ASB formation were mostly focused on analyzing the specimens after shear band formation. Leech [10] confirmed the occurrence of ASBs in 7039 aluminum alloys during plate impact experiments. Owolabi *et al.* [11] performed dynamic compression experiments using a Kolsky bar apparatus on AA 6061 and compared the shear banding behavior with 6061/Al_2O_3 composites. The probability of ASB formation was found to increase when alumina was added as reinforcement. Li *et al*. [2] conducted impact experiments on aluminum alloy 7075 with a thick-walled cylinder-external explosive collapse technique. The researchers examined the microstructure of post-mortem specimens and identified the deformed and the transformed shear bands.

The non-uniform plastic deformation under dynamic loading leads to localized temperature increase, which further results in a coupled thermomechanical condition. The following heat conduction equation (1.1) is used by Rosakis et al. [12] and Mason et al. [13], which expresses the relationship between the heat generation and the temperature change:

$$\alpha \nabla^2 T - \dot{T} = -\frac{\beta \sigma \cdot \dot{\varepsilon}^p}{\rho c_p} + \frac{\kappa}{\rho c_p} \frac{E}{(1-2\nu)} T_0 \, \mathrm{tr}(\dot{\varepsilon}^e) \tag{1.1}$$

where α is the thermal diffusivity, T is the temperature field, ρ is the density, c_p is the heat capacity, σ is the stress, $\dot{\varepsilon}^p$ is the plastic strain rate, κ is the coefficient of thermal expansion, E is Young's modulus, ν is Poisson's ratio, $\dot{\varepsilon}^e$ is the elastic strain rate, T_0 is the initial temperature and β is the coefficient of plastic work converted to heat. The first term on the right stands for the heat from plastic deformation while the second term represents the heat from elastic deformation. By assuming adiabatic condition with only plastic deformation, Equation (1.1) can be simplified as follows [12 – 15]:

$$\beta = \frac{\rho c_p \dot{T}}{\int \sigma \, d\varepsilon} \tag{1.2}$$

The investigation of β is largely based on the loading and temperature history, as well as the material properties. Therefore the accurate measurement has been a challenge. Early research usually assumed β as a constant of 0.85-1.0 [16], which means almost all the plastic work are converted to heat. Later it was claimed that β may be dependent on strain [17] and most recent work showed β is also dependent on strain rate [14]. Also different values of β are reported in the previous works, ranging from 0.3 to 0.9 under dynamic loading. Since the plastic work to heat coefficient serves as a bridge between the material deformation and the temperature. A better understanding of β during adiabatic shear banding will certainly assist in the study of its mechanism.

Due to the difference in thermal and mechanical properties, materials exhibit different shear band behaviors. To better understand shear banding mechanism, it is crucial to know not only the deformation, but also the temperature field within a propagating ASB. Hartley *et al*. [18] performed temperature measurements when loading tubular steel specimens with torsional Kolsky bar. They found a band width of 250 μm with a temperature rise of approximately 450 °C for low carbon steel. Duffy and Chi [19] and Marchand and Duffy [8] reported real time measurement of strain using grid observation and temperature fields using an infrared camera. The alloy steels they studied exhibited shear bands roughly 20 μm in width. However, the spatial resolution for both

temperature measurements were about the same as the width of the shear band, meaning the temperature measured was actually an average temperature around the band tip. This average can be regarded as a lower bound of the local temperature peak. By tracking the temperature field, they were able to estimate an ASB propagation speed of ~500 m/s. Later, Zhou *et al*. [20] conducted an in-depth study on impacting notched C300 steel and Ti-6Al-4V. Both high-speed photography and temperature detection were used during the experiments. The maximum shear band speed of steel was found to be 1200 m/s and was strongly dependent on the impact velocity. The maximum temperature rise was approaching 1400 °C for C300 steel at an impact velocity of 43 m/s, while only 450 °C for Ti-6Al-4V at an impact velocity of 64.5 m/s. Based on the experimental findings, Mercier and Molinari [21] proposed an analytical model to describe the dynamic ASB propagation in mode II. In contrast to the shear band formation studies on steel and titanium alloys, temperature measurements on aluminum alloys are rarely reported. Hence, studies on the conditions under which shear bands initiate and propagate as well as the evolution of temperature fields within the shear bands are required for determining the structural integrity of aluminum alloys under dynamic loading conditions.

Guduru *et al*. [22] also investigated the strain and temperature fields in a fully developed ASB of C300 steel, but with the coherent gradient sensing technique and a self-developed high-speed infrared camera. The results showed a non-uniform temperature distribution along the shear band. Multiple high temperature areas were observed with the spacing in the range of 0.25 mm to 1 mm. The high-speed infrared camera technique provided a possibility for measuring the temperature rise with higher spatial and temporal resolutions. More recently, Guo *et al.* [23] reported shear banding experiments on commercial titanium using a compression Kolsky bar setup with both high-speed camera and infrared camera. The group of researchers claimed the temperature rise in the titanium occurs after ASB formation, which was considered to be the consequence of ASB. The plastic work to heat coefficient β was found to be between 0.25 – 0.55 and was also strain rate dependent, which was below the traditionally used value of 0.8 – 1.0. This result raised a new concern towards the relationship between the mechanical and thermal behaviors of shear banding.

1.2 High-speed temperature measurement techniques

During plastic deformation of ductile materials, the external work is converted as heat and dissipated, leading to temperature rise within the materials. This temperature increase can be intense if the material is loaded dynamically. Localized deformation associated with thermal-mechanical instability will occur. With the increasing need in studying the material thermal behaviors during dynamic loading, temperature measurement techniques that can be operated to capture the high-speed events are of particular interest. There are a large variety of methods reported in the literature in different applications, including both contact and noncontact methods.

Contact methods generally rely on the thermal conduction between the specimen material and the measuring device at a contact location, either inside the material or at the surface level. A good contact of the interface and a balanced thermal state are the keys to accurate temperature measurement. One of the contact methods is using thermocouples. Due to the nature of the dynamic loading, the temperature change occurs within very short period of time (10^0 – 10^2 μs). The thermocouple is required to have a response time in a smaller scale than the dynamic event, leading to challenges in high-speed temperature measurement. Since a thermocouple measure correct temperature only when it reaches the thermal balance with the object, the dimension of the thermocouple plays an important role. Table 1.1 shows typical response time of fine type-J thermocouples calibrated in the moving air of 18.3 m/s [24]. It can be found that these thermocouples with diameter less than 1 mm takes 4 – 3200 ms to respond to temperature. Farahmand *et al.* [25] also reported a mean overall response time of 55 ms using the thermocouples in the similar dimensions. Generally the response time of thermocouples are too large for the application to the real-time temperature measurement during dynamic loading. It is also not enough to reveal the temperature revolution during the shear band formation.

There are literature showing the high-speed temperature measurement with ultra-fine thermocouples. Rittel [26] embedded thermocouples with 127 μm in wire diameter inside polycarbonate, PMMA and polystyrene disk specimens, as shown in Figure 1.6. Then the researcher performed dynamic compression experiments with a Kolsky bar. The recorded strain gage signal and temperature response during dynamic loading are presented in Figure 1.7. Since the thermocouple is placed inside the material within a small hole, it will take time for good contact to set up after the deformation begins. Therefore a small delay in the temperature curve can be

found at the beginning of the loading before the temperature is measured. Regardless of the delay, the response time of the embedded thermocouple was reported in the order of 10 μs. However, thermocouples are limited to measure temperature at certain attached locations. If the exact location of interest is unknown prior to an experiment or attaching/embedding the thermocouple will result in changes in material properties, thermocouples may not be a good choice.

Table 1.1. The response time of type-J thermocouples reported by OMEGA [24].

Wire size (in.)	Response time (ms)
0.001	4
0.005	80
0.015	800
0.032	3200

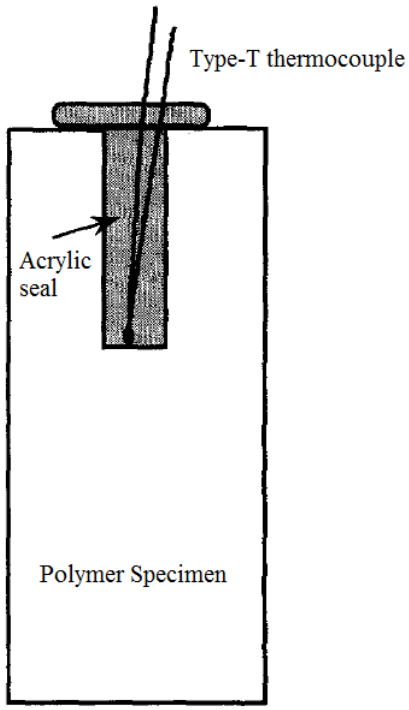

Figure 1.6. The polymer specimen with the embedded thermocouple used in [26].

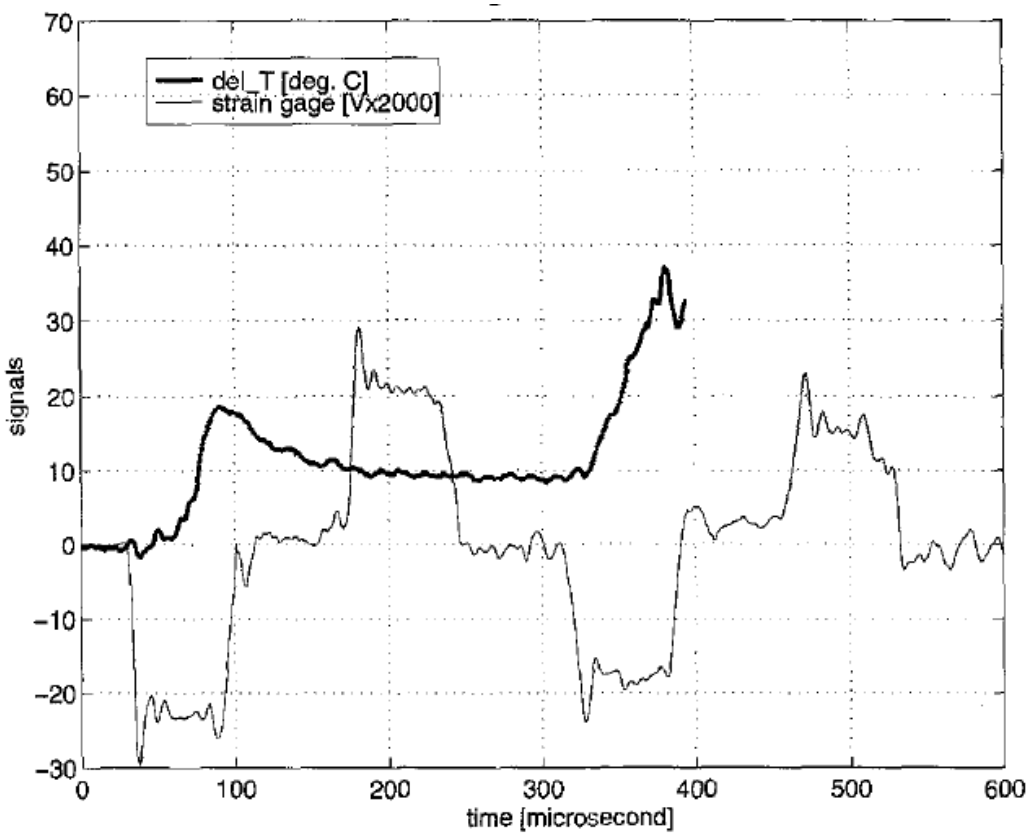

Figure 1.7. Temperature rise and strain gage signals for a polycarbonate. Reproduced from [26].

Noncontact temperature measurement methods are the techniques not based on thermal conduction, e.g. infrared sensing, optical pyrometry and phosphor thermometry. Because of the fast response and wide sensitive range, infrared techniques become widely adopted in dynamic experiments, including both infrared detectors and high-speed infrared cameras [19 – 23]. Mason *et al.* [13] used an 8-detector array to record the temperature response during dynamic compression of 4340 steel, 2024 aluminum and Ti-6A1-4V titanium alloys. This infrared detector array was formerly introduced by Zehnder and Rosakis [26, 27]. The experimental apparatus is presented in Figure 1.8. The indium antimponide (InSb) infrared detectors used are sensitive to 1 – 5.5 μm wavelength of the radiation, which covers the emission wavelength of 1 – 2 μm when the temperature is between 100 – 1000 °C. The rise time of the system is primarily determined by the frequency response of the detectors and the amplifier, which is able to reach microsecond scale. This rise time is sufficient in response to the temperature rise during a dynamic experiment and is also faster than most of the thermocouples available commercially. Technically this system can

measure temperature increase as low as 20 °C. But the accurate recording can only be obtained above 50 °C temperature increase, as claimed by the group of researchers, due to the large signal to noise ratio when measuring low temperature difference, The eight measuring areas are designed along the loading direction with each one in the size of 0.16 × 0.16 mm with 0.2 mm spacing between each detector. The total length of temperature can be measured is 1.56 mm, which covers the entire area of interest in this study. With magnification of one for the optical systems, the measured area are the same in the dimension as the array of detectors. The maximum temperature are documented as 120 – 150 °C for aluminum 2024 at 3000 /s strain rate and Ti-6A1-4V titanium alloy at 1500 /s. Give the size of each detector, the measured result is the average temperature over each square area [13]. Normally an infrared detector or an infrared camera need to be calibrated with a black body before being applied to other different materials. In this paper, the infrared detectors are directly calibrated with a heated specimen at controlled temperature while infrared records are taken. This calibration procedure reduces the uncertainty caused by the emissivity change of different material surfaces. Figure 1.9 shows the calibration results of 4340 steel with 600 and 120 grit surface finish. The measurement is observed fairly consistent and the emissivity is not sensitive to the surface finishes of the same material. Therefore the experimental error resulted from emissivity change due to the material deformation is negligible. Later Guduru *et al.* [32] developed a high-speed infrared microscopic camera to image the propagating shear bands. The camera features 64 HgCdTe IR detectors in an 8×8 array, with each of the signal amplified and recorded simultaneously. The infrared images show discrete hot spots in a developed shear band with temperature over 600 K. Among all of the researches mentioned above, the reported frame rates are generally within $10^1 – 10^2$ kHz with a spatial resolution in the order of 10^2 μm. Considering that some of the important impact related events, such as dynamic cracking and shear banding, can be in the scale of $10^0 – 10^2$ μm, the aforementioned spatial resolution results in the temperature being averaged over a certain area. Therefore the measured temperature is always a lower bound of the real local temperature.

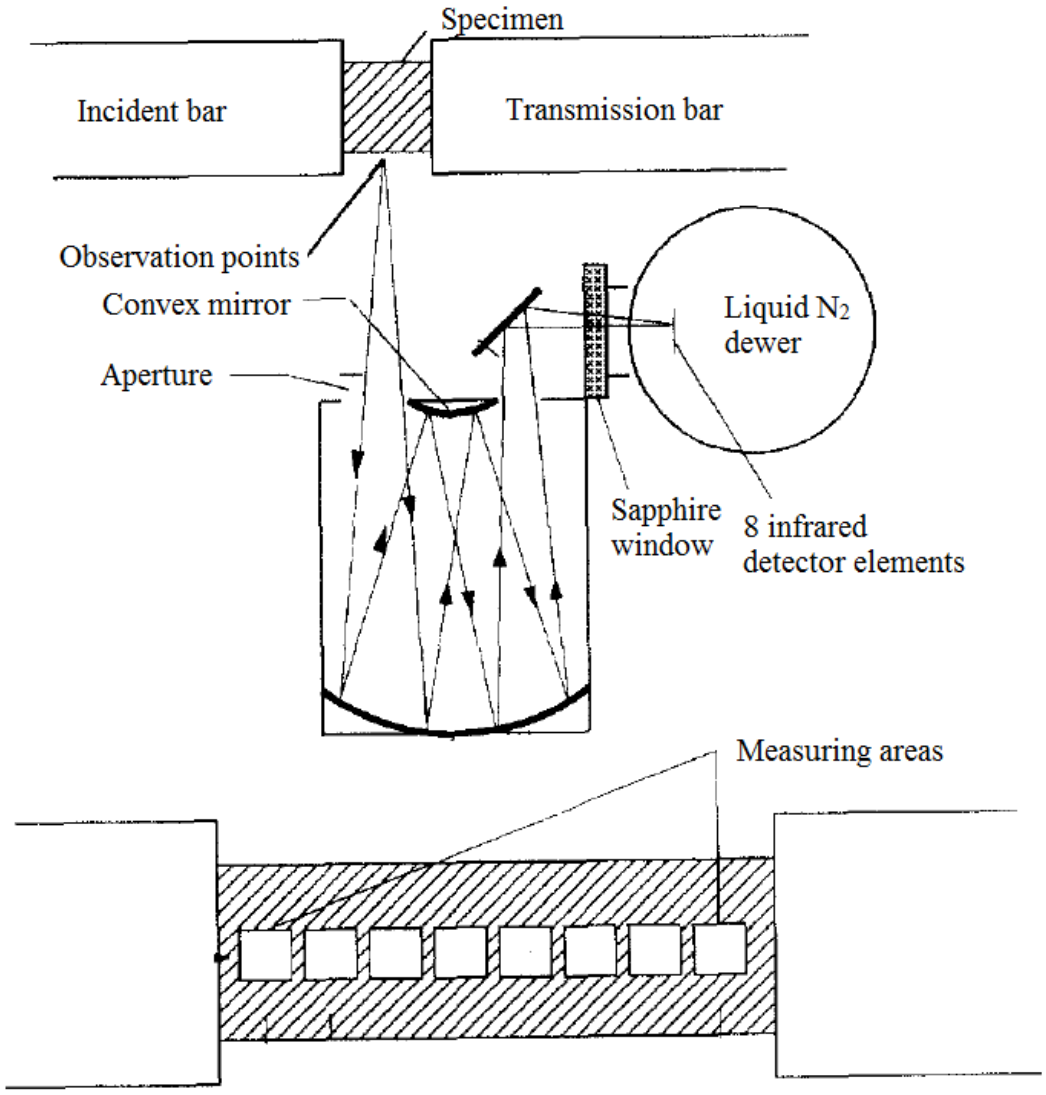

Figure 1.8. A schematic representation of the high speed infrared detector array focused on a specimen in a Kolsky bar [13].

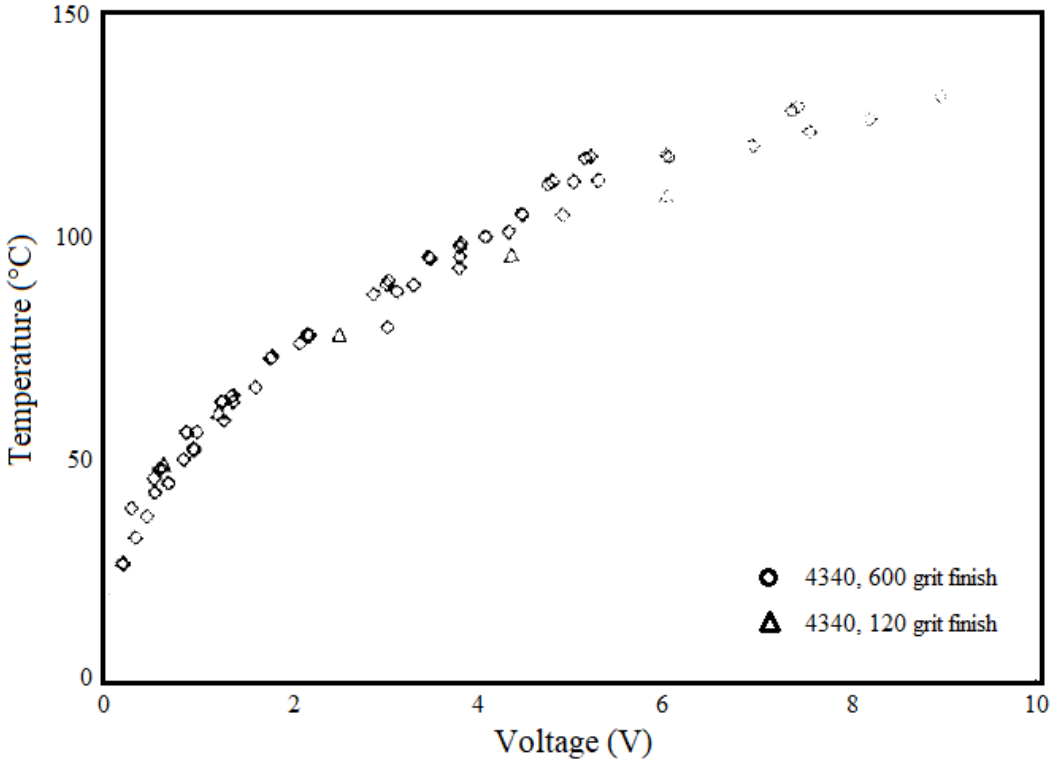

Figure 1.9. Calibration of infrared detectors with steel for different surface finishes. Reproduced from [13].

Phosphor thermometry is another noncontact optical method for surface temperature measurement. The method exploits luminescence emitted by phosphor material. Phosphors are fine powders which may be stimulated to luminesce. This method will be discussed in details in the Chapter 1.3.

1.3 Phosphor thermometry

Phosphor thermometry is a non-intrusive, emissivity-independent, optical diagnostic tool for measuring temperature fields on short times scales. With careful handling, the method offers both high sensitivity and accuracy measurement [33]. It can be applied to solid surfaces if the materials are coated with phosphors or fluid flow if phosphors are pre-mixed with the fluid. In the past forty years, the improved camera technology has made two-dimensional temperature imaging more feasible. On the other hand, the versatility of phosphor thermometry has tremendously motivated the exploration of new thermographic phosphors as well as the development of different temperature measuring techniques.

Thermographic phosphors are luminescent materials that emit light after absorbing energy from electrons. The excitation source can vary from X-rays, ultraviolet (UV) light, visible light to neutrons [34]. The differences in time-dependent luminescence behaviors and material characteristics enable the phosphors to be used with different methods, which can be generally categorized into time-resolved and time-integrated strategies. There are various methods under each strategy, as shown in Figure 1.10 [33].

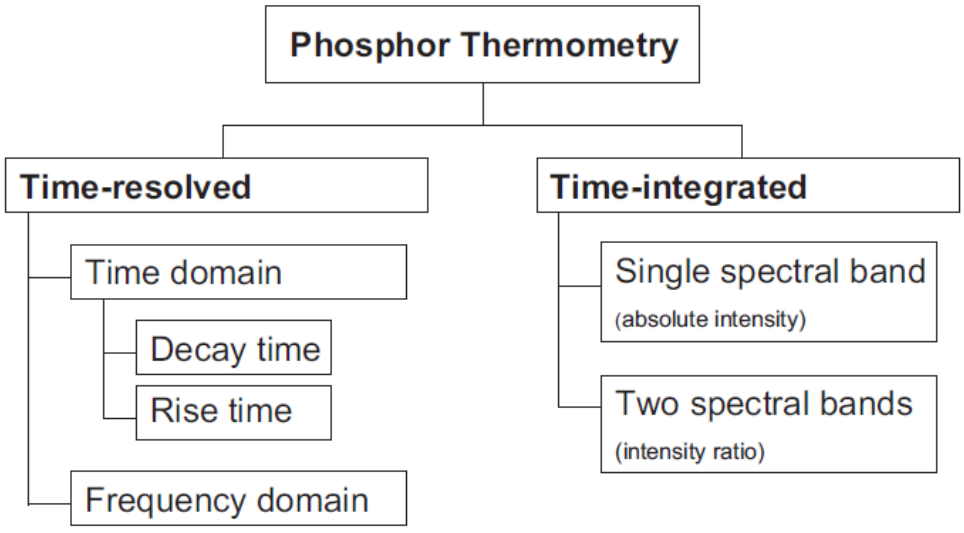

Figure 1.10. Classification of different methods of phosphor thermometry [33].

One of the time-resolved methods under time domain is the lifetime decay method, in which the phosphorescence decay is monitored following excitation. Figure 1.11 compares the

representative decay characteristics of Europium-activated Lanthanum Oxysulfide (La_2O_2S:Eu) phosphor at different temperature [35]. The phosphorescence lifetime of La_2O_2S:Eu decreases with increasing temperature because of a charge transfer state [36]. The transient phosphorescence intensity after the excitation can be described by a single exponential function:

$$I(t) = I_0 e^{-t/\tau} \tag{1.3}$$

where I_0 is the initial intensity at $t = 0$ and τ is the life time of the phosphor. By calibrating the life time with corresponding temperature prior to the experiments, it is possible to find the temperature based on the measured intensity.

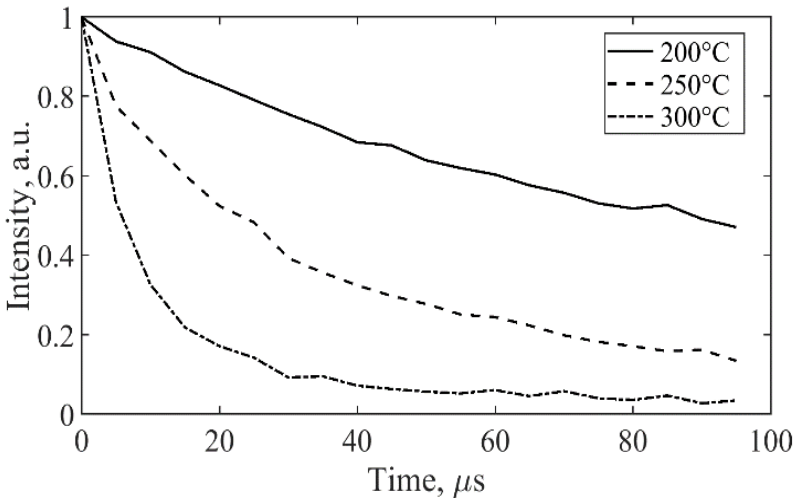

Figure 1.11. Intensity decay of La_2O_2S:Eu phosphor [35].

Earlier, the life time decay method was studied with the use of photomultiplier tubes or photodiodes [29 – 36], with most of the laser excitation systems operating at 10 Hz. With the development of improved high-speed camera systems, two-dimensional temperature imaging for temporally and spatially resolved detection of phosphorescence intensity became popular. In previous studies, the lifetime method was used to measure 2-D temperature fields with multiple CCD chips or single-chip CCD framing cameras [37 – 39] to capture different stages of the decay. These techniques only featured limited number of images that were insufficient to achieve decent

accuracy in the temperature. The application of high-speed CMOS cameras overcame some of the barriers and greatly improved the accuracy and sampling rate.

Recently, Ayers *et al.* [35] reported 100 kHz temperature measurement on a phosphor coated aluminum specimen using laser phosphorescence. The specimen was coated with La_2O_2S:Eu phosphor and placed inside an optically accessible furnace at controlled temperature. A burst-mode Nd:YAG laser at 355 nm was used to excite the specimen at 100 kHz. To obtain sufficient data points for the decay curve fit, the high-speed camera was operating at 1 MHz, capturing 10 images after each excitation. The decay history is presented in Figure 1.12. As stated above, the temperature filed measured from the lifetime decay method fully relies on the decay curve fit of multiple images. It is preferred that the object is stationary during these images so that proper pixel registration can be obtained during single decay. However, both displacement and deformation of a material are present during dynamic loading, which will result in incorrect temperature measurement. Therefore the lifetime decay method is not ideal to be used with dynamic testing of solid materials.

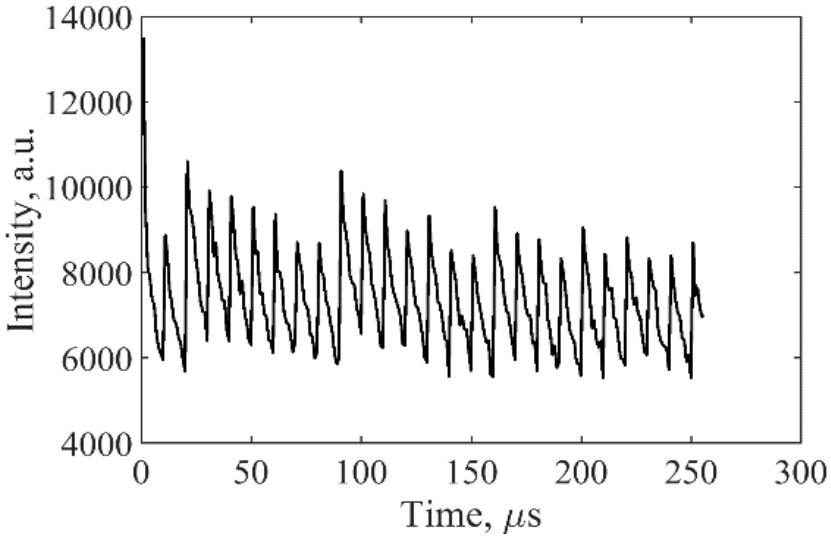

Figure 1.12. 100 kHz pixel intensity history of La_2O_2S:Eu phosphor at 260 °C [35].

Other than the time-resolved characteristics, the time-integrated phosphorescence intensity of phosphors is also temperature-dependent. The absolute intensity method using single spectral band requires the excitation source to be very consistent so that the emission intensity can be

calibrated with the temperature. Therefore it is not accurate for diagnostic purposes and has been rarely reported. The intensity ratio method is the only practical method when using laser phosphorescence with time-integrated strategy. This technique is initially used by Cundy *et al.* [48] in a heated nitrogen jet. Later, Abram *et al.* [49] performed high-speed measurement on gas-phase temperature field with laser phosphorescence. Prior to the experiment, $BaMgAl_{10}O_{17}:Eu^{2+}$ (BAM:Eu) phosphor particles were mixed with air streams and then excited with an 355 nm UV laser. BAM:Eu exhibits a red shift in the emission spectrum with increasing temperature, as illustrated in Figure 1.13. A two-color detection scheme can be designed so that the intensity in the low wavelength channel (shown within the blue line) changes monotonically while the intensity in the high wavelength channel (shown within the red line) is almost identical. And the intensity ratio of the two channels corresponds to the temperature. A schematic of the experimental setup is shown in Figure 1.14. Due to the required two-channel measurement, two cameras were synchronized to capture intensity images simultaneously with a beam splitter. The group of researchers reported temperature field measurement from room temperature to 500 K with a spatial resolution of 35 μm and a frame rate of 3 kHz. One of the advantages to use phosphor thermometry is that the temporal and special resolution are mainly determined by the high-speed camera without limited by the infrared characteristics or other means. Also, ratio method does not require decay curve fitting so that every pair of images taken represents the temperature field at the corresponding time. The object movement is no longer a concern, and the camera capability can be fully utilized. Currently the high-speed camera is reported to provide 10^1 μm resolution scale at 10^5 Hz frame rate as discussed, making this method a potential candidate to obtain temperature filed evolution during dynamic loading of materials.

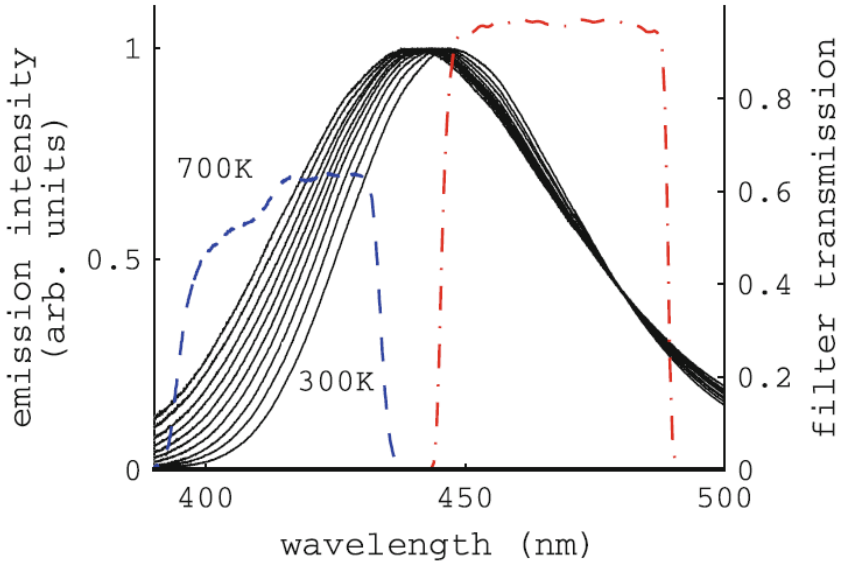

Figure 1.13. Normalized BAM:Eu emission spectral. Reproduced from [49].

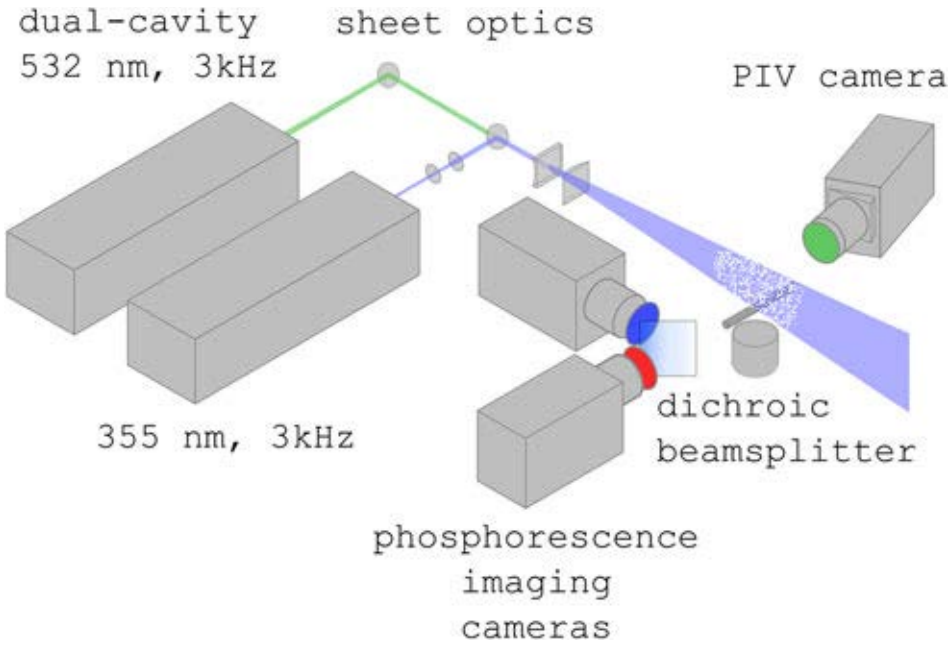

Figure 1.14. The experimental setup used by Abram *et al.* [49].

1.4 Objectives and research approach

Despite all the efforts in the previous chapters, the best spatial resolution of the aforementioned deformation measurements was only in the order of tens of microns [2, 8, 10–12]. Most of the reported research on dynamic ASB formation is still based on post-mortem analysis. Observation of ASB propagation in real time with higher resolution is still desired to pinpoint the critical conditions. Considering that the width of ASB reported in the literature is mainly in the order of 10^0 to 10^2 μm and the shear band speed can reach several thousand meters per second, a visualization method with both higher spatial resolution and higher frame rate is desired to better observe the local shear band propagation and locate the propagating band tip. However, it is challenging to further improve the spatial resolution. This is partially limited by the wave length of visible light and the short working distance from the specimen when a high magnification lens is used. An experimental technique has recently been introduced by Hudspeth *et al*. [50] where a Kolsky bar setup is synchronized with high-speed synchrotron X-ray imaging at Argonne National Laboratory. The technique incorporating X-ray Phase Contrast Imaging (X-ray PCI) was developed to capture the damage history during a dynamic experiment in real time. Parab *et al*. [51] and Nie *et al.* [52] utilized this technique to observe the crack propagation in glass and composite materials. The researchers showed the possibility for *in situ* observation of damage development inside certain opaque materials under dynamic loading. A spatial resolution of 1.6 μm can be achieved by using a magnification of 20× with a sufficient objective distance depending on the location of the scintillator. The temporal resolution can be at 200 ns or 5 million frames per second. This method offers a new opportunity in observing the initiation and propagation of an ASB in more details.

The temperature evolution during the ASB formation is also crucial as it is closely related to the mechanism of ASB. Many measurement using infrared detectors and cameras are available, but the frame rate and the spatial resolution are both limited to reveal the real temperature during the dynamic event. Therefore, a temperature measurement technique with spatial resolution higher than 10^1 μm scale and frame rate higher than 10^5 Hz is desired. With the development of the phosphor thermometry in temperature measurement on solids, the recent technique of high-speed temperature field measurement and the intensity ratio method provide new possibility in observing the temperature evolution during dynamic loading. In this study, we start with the state-of-the-art

technique of high-speed infrared camera. Then a high-speed laser phosphorescence thermal imaging system is developed and integrated with a compression Kolsky bar apparatus. This technique will be first applied to copper under dynamic compression to verify the temperature field measurement capability. And then the temperature evolution during shear band formation in aluminum will be investigated.

2. IN SITU OBSERVATION OF ADIABATIC SHEAR BAND FORMATION

The formation of adiabatic shear band has been found in many materials. During dynamic plastic deformation, the plastic work is mainly converted into heat over a very short time period, leading to temperature increase within the material. The focus of this chapter is to examine the effectiveness of using high-speed X-ray PCI and high-speed infrared thermal imaging to investigate ASB in metals. The results of deformation and temperature field measurement showing the ASB formation in aluminum alloy 7075-T6 and 6061-T6 are presented. Part of the work in this chapter is accepted and soon to be published by Experimental Mechanics, Springer Nature with article name *In situ Observation of Adiabatic Shear Band Formation in Aluminum Alloys* [53].

2.1 Materials and Methods

2.1.1 Materials and specimens

The materials used in this experiment were selected to be well-studied commercially available aluminum alloys 7075-T6 and 6061-T6. In order to image the shear band formation at a pre-determined location, a hat-shaped specimen geometry was adopted. This hat-shaped specimen method, introduced by Meyer *et al.* [54] and Hartmann *et al.* [55], has been widely used to study the shear localization of various metals [48 – 51]. The advantage of using this geometry is that shear bands can be generated in many ductile materials within the designated narrow region [60]. The versatility of the specimen geometry design enables precise control over the desired stress state with a conventional compression Kolsky bar setup. The deformation in the specimens can also be easily stopped at desired stages by having stoppers with proper thickness to collect the specimen before fracture.

Most of the hat-shaped specimens in previous research were designed in a cylindrical shape like a real “hat”. However, in this work, a flat hat-shaped specimen with thickness of 0.8 mm is used to facilitate *in situ* high-speed X-ray visualization. The specimen geometry is shown in Figure 2.1 and the dimensions are presented in Table 2.1. The punch width w_1 is designed to be larger

than the opening width w_2 to achieve a compression-shear stress state. This stress state prevents the material from experiencing early failure so that the adiabatic shearing can be visualized.

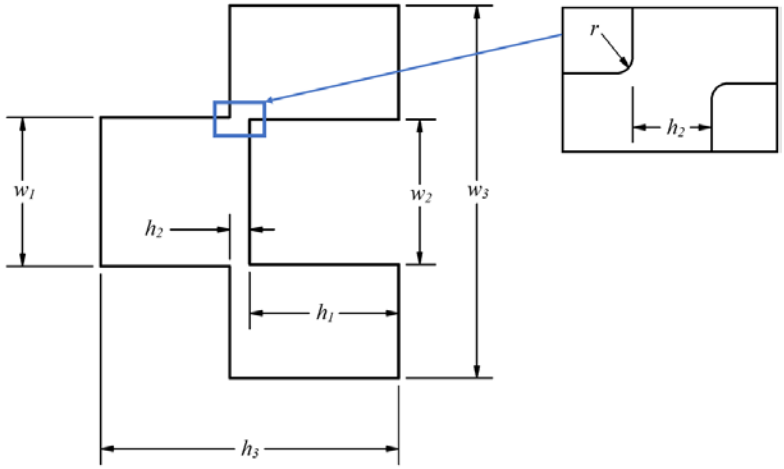

Figure 2.1. The geometry of hat-shaped specimen and the compression-shear region

Table 2.1 Dimensions of the hat-shaped specimen (mm)

w_1	w_2	w_3	h_1	h_2	h_3	r
7.62	7.42	19.05	7.62	1.02	15.24	0.25

The specimens were cut to dimensions from aluminum sheets with wire electrical discharge machining (EDM) to minimize the damage on the edges of the specimens. Then multiple vertical lines were carved within the compression-shear region of the specimens by a razor blade, providing sufficient contrast to reveal the localized shear deformation in the material. Because of the nature of the specimen dimension, plane stress condition is assumed so that the material is considered to be uniformly deformed through the thickness and only the surface deformation is measured.

2.1.2 Kolsky bar

A Kolsky bar, or split-Hopkinson pressure bar (SHPB), has been commonly used when investigating the material behaviors at $10^0 – 10^1$ m/s loading speed [61]. For this study, a miniature

compression Kolsky bar was used (Figure 2.2). The Kolsky bar was composed of a striker bar (diameter = 12.7 mm, length = 76 mm) and an incident bar (diameter = 12.7 mm, length = 1372 mm), both manufactured from a high strength steel alloy. The transmission bar in the conventional Kolsky bar apparatus was replaced with a load cell (Kistler 9212, Winterhur, Switzerland) mounted on a heavy aluminum backstop due to space constraints in the APS X-ray hutch. A specimen holder is designed to support the specimen in position and prevent buckling, as shown in Figure 2.3.

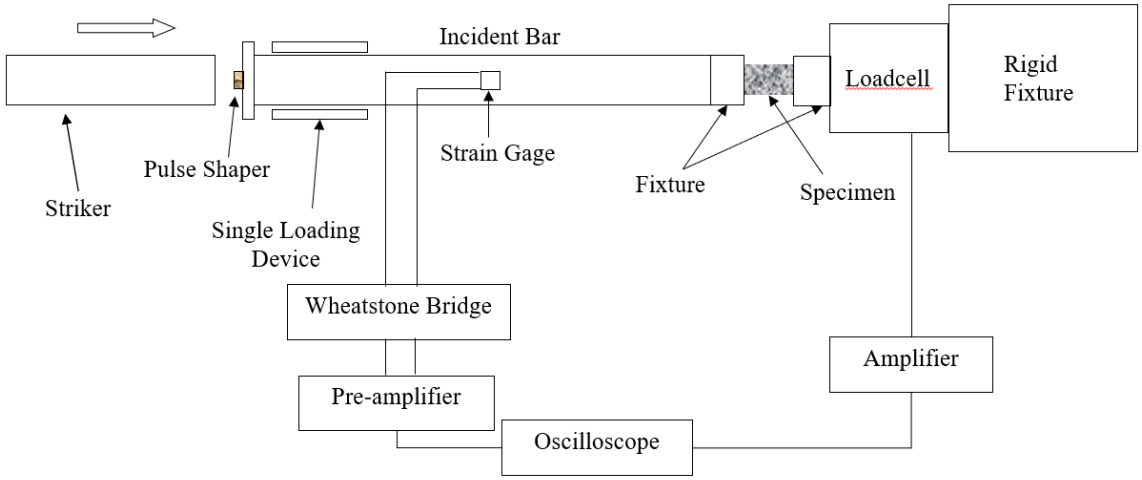

Figure 2.2. A schematic of the compression Kolsky bar setup

Figure 2.3. A photograph of the specimen section of the Kolsky bar setup

The firing system consisted of a zero-pass solid-state relay and a fast-response solenoid valve. This valve was located close to the inlet nozzle of the barrel assembly, allowing for the minimal ramp-up pressure needed to ensure consistent delay timing from solenoid trigger to striker-incident bar impact.

When the solenoid valve suddenly opens, the compressed air is released from the air tank into the barrel, pushing the striker to impact the incident bar. A compressive stress pulse is generated from the bar end and propagates along the incident bar towards the specimen. A certain pulse shaper is needed for generating the desired shape of the stress pulse. The material and dimension of the pulse shaper depend on the specimen properties and loading rate. In this work, three layers of masking tape are used as the pulse shaper. The stress pulse will be captured by a pair of strain gages attached to the bar as the incident pulse and then recorded by the oscilloscope. When this pulse reaches the specimen-bar interface, part of the stress will be reflected back and recorded as the reflected pulse. The rest of the stress pulse is transmitted through the specimen in the form of dynamic loading.

Two semi-conductor strain gauges (Kyowa KSP-2-1K-E4, Chofu, Japan) were attached diametrically to the surface of the incident bar and were connected in a half Wheatstone bridge configuration. The strain gauge assembly was used to record both the incident and reflected pulses. The load cell was used to record the force response of particles at the back end. Both the strain gauge signal and load signal were synchronized and collected via an oscilloscope (Tektronix DPO7104C, Beaverton, Oregon). The velocity at the bar end was calculated from the recorded strain signals using Equation (2.1).

$$v(t) = C_B(\varepsilon_i(t) - \varepsilon_r(t)) \tag{2.1}$$

where C_B represents the elastic wave velocity in the bar. ε_i and ε_r represent the incident and reflected strain values respectively. The bar end displacement was then calculated using Equation (2.2).

$$d(t) = \int_0^t v(\tau) d\tau \tag{2.2}$$

From the recorded strain gauge signals and the corresponding high-speed X-ray images, the loading velocity for the typical experiment was measured to be around 16 ± 2 m/s.

2.1.3 High speed synchrotron X-ray phase contrast imaging

The dynamic experiments with X-ray phase contrast imaging (PCI) were performed at beamline 32-ID-B of the Advance Photon Source (APS) at Argonne National Laboratory. The compression Kolsky bar described in the previous section is integrated with the synchrotron X-ray imaging setup, which was developed through collaboration between Purdue University and APS. A schematic of the experimental setup is presented in Figure 2.4. This method was discussed in more detail in [50].

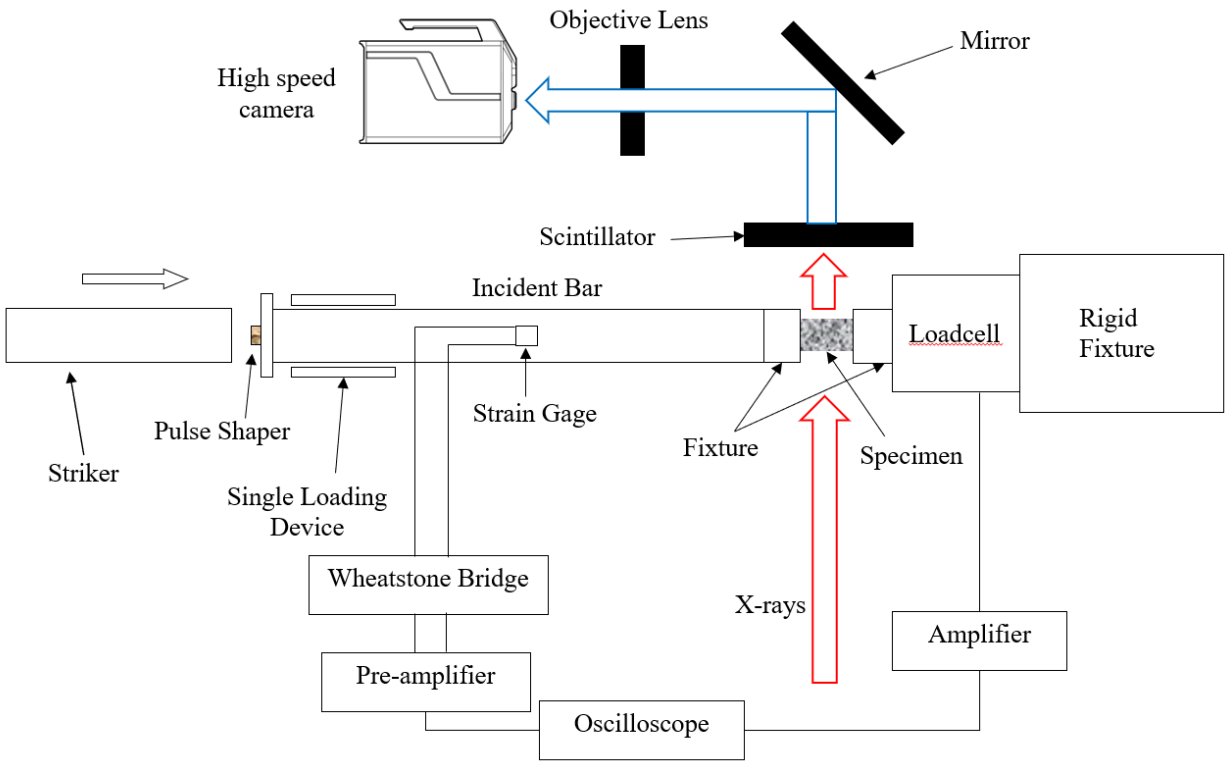

Figure 2.4. Dynamic compression setup with high-speed X-ray phase contrast imaging

The *in-situ* shear banding and crack propagation were recorded at 5 MHz frame rate with a Shimadzu HPV-X2 high-speed camera. Appropriate time delays need to be calibrated prior to the experiments to synchronize the camera with the start of the loading and passing of the X-rays through the specimen to capture the dynamic shear band forming event. The material deformation and shear banding are captured by a scintillator-camera system while the dynamic force history is recorded by the piezoelectric load cell.

2.1.4 Infrared thermal imaging

The temperature field measurements during the dynamic shearing event were performed separately with the same compression Kolsky bar setup. The experimental conditions were maintained the same so that the results can be directly related to the X-ray imaging experiments. A Telops FastM3k (Telops, Quebec City, Canada) infrared thermal camera with 1× lens was used to record the surface temperature distribution of the aluminum specimens at 64 kHz. The view window of the thermal camera is 1.6×0.4 mm and the pixel size of the image is 30 μm. A photograph of the experimental setup is shown in Figure 2.5. The thermal camera was pre-calibrated with a black body by the manufacturer before being used in this work. During the experiments, the lens of the camera is adjusted to focus on the surface of the specimen.

The true temperature is calculated from the radiance temperature with Equation (2.3):

$$T_{true} = \frac{T_{rad}}{\sqrt[4]{\varepsilon}} \tag{2.3}$$

where ε is the emissivity of the given material. Wen and Mudawar [62] performed an independent study on the emissivity of various aluminum alloys with different surface quality, temperature ranges and wavelength ranges. The results show that the emissivity of a certain aluminum alloy does not change significantly in 3 – 5 μm wavelength range and 600 – 800 K temperature range, which are our application ranges. The aluminum specimens used in this work were initially mirror polished, but due to exposure to air they quickly formed a visible oxide layer. During deformation, the material surface can gradually become rough, which leads to the change of the emissivity within 0.1 – 0.2. Figure 2.6 shows the relationship between true temperature calculated by Equation (2.3) and emissivity, given the radiance temperature of 450 K and 480 K. When the emissivity varies between 0.1 and 0.2, there will be approximately 10% error in the calculated true temperature. Taking all the aforementioned factors into account, an averaged constant emissivity of 0.15 is used for both aluminum alloys.

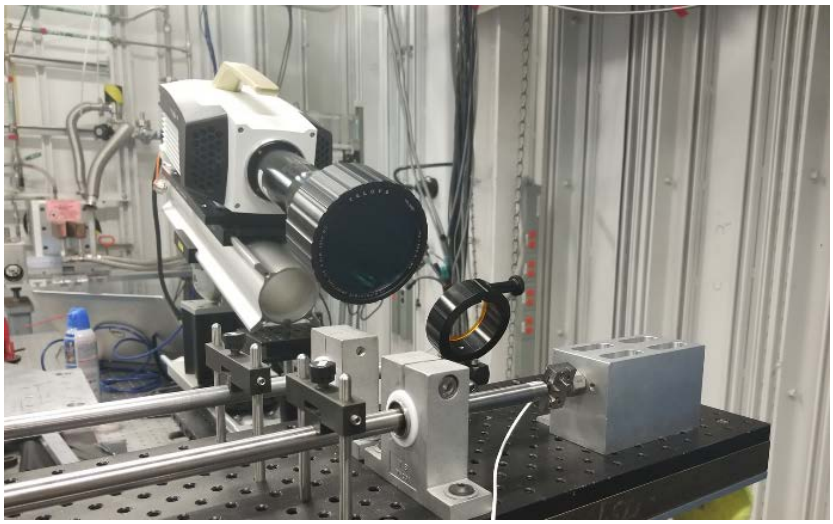

Figure 2.5. A photograph of experimental setup of high-speed infrared camera and Kolsky bar.

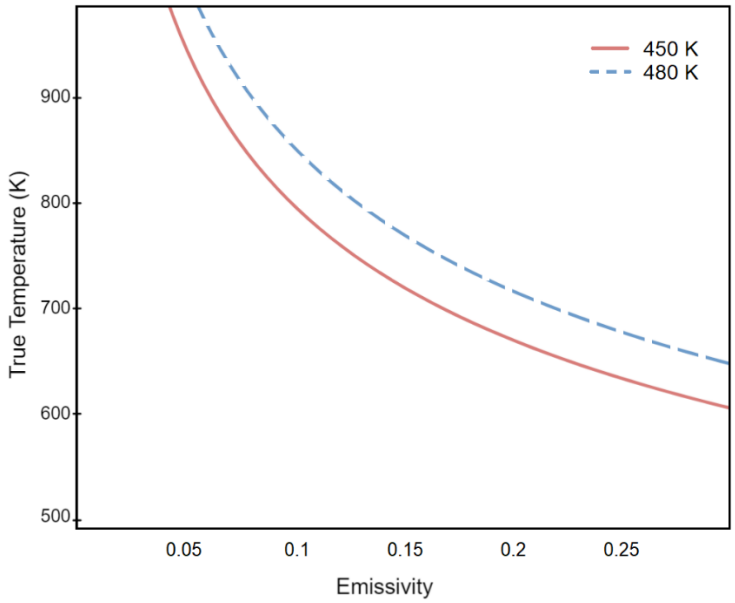

Figure 2.6. The true temperature–emissivity relationships at radiance temperature of 450 K and 480 K.

2.2 Experimental Results

2.2.1 Aluminum 7075-T6

The shear banding behaviors of the aluminum 7075-T6 under dynamic shear were studied in five hat-shaped specimens under repeated experimental conditions. The force-displacement relationship and the high-speed image sequence of a representative experiment are shown in Figure 2.7. An edge detection algorithm with polynomial curve fit is used to track the deformation of the blade carved lines from image 2 to 6. The gradient of these computer-generated lines represents the shear strain. When the hat-shaped specimen is compressed, the material in the desired shear region is subject to shear. The carved lines bend during the deformation and the distortion is most significant in the area where the maximum shear strain is located. By tracking the movement of the lines and calculating the gradients of the fitted curves, the approximate strain can be obtained, which is corresponding to the time sequence of the images. When the value of the maximum derivative along a line exceed 1.0, we consider a shear band formed. The points when the high-speed images were taken are marked on the force history plot.

In this particular experiment, the camera window is focus on the area that is shown in the close-up view in Figure 2.1. One of the corner edges of the specimen is just outside the left side of the camera imaging window of 0.64 mm by 0.4 mm. At t = 0 μs, the specimen starts being loaded. All of the razer-blade-carved parallel lines remain straight, showing no deformation in the material. At t = 16.8 μs, shear deformation can be observed within the designated gage section. However, by taking a close examination of the line gradients, we can find that the first line from the left has larger gradient than the other lines. The maximum local shear strain along this line is measured as 1.4, which indicates that the dynamic shear deformation is propagating along the loading direction, i.e., from left to right in the image. This shear deformation then becomes highly localized and starts to form a shear band in the image taken at t = 17.4 μs. At t = 18 μs, the maximum shear strains along the six lines range from 1.9 to 5.7. A crack initiation is also oberved, as marked by the arrow. This crack propagates along the same direction as the ASB (t = 18.6 μs), resulting in the discontinuity of the left two vertical lines. In this experiment, the force approaches its maximum at this point. But in some other experiments, the force was found to keep increasing after the shear band is initiated. This can be caused by the specimen geometry.

There are two shear regions on each specimen and which one fails first is random. At t = 19.2 μs, the crack causes the material to separate. The crack speed can be estimated from the images as ~1100 m/s. The entire fracture of the specimen occurs when the crack propagates through the gage section, which is not recorded in these images. During the entire recorded event, no significant shear strain is found in the vertical direction, as the horizontal carved lines remain straight in all six images.

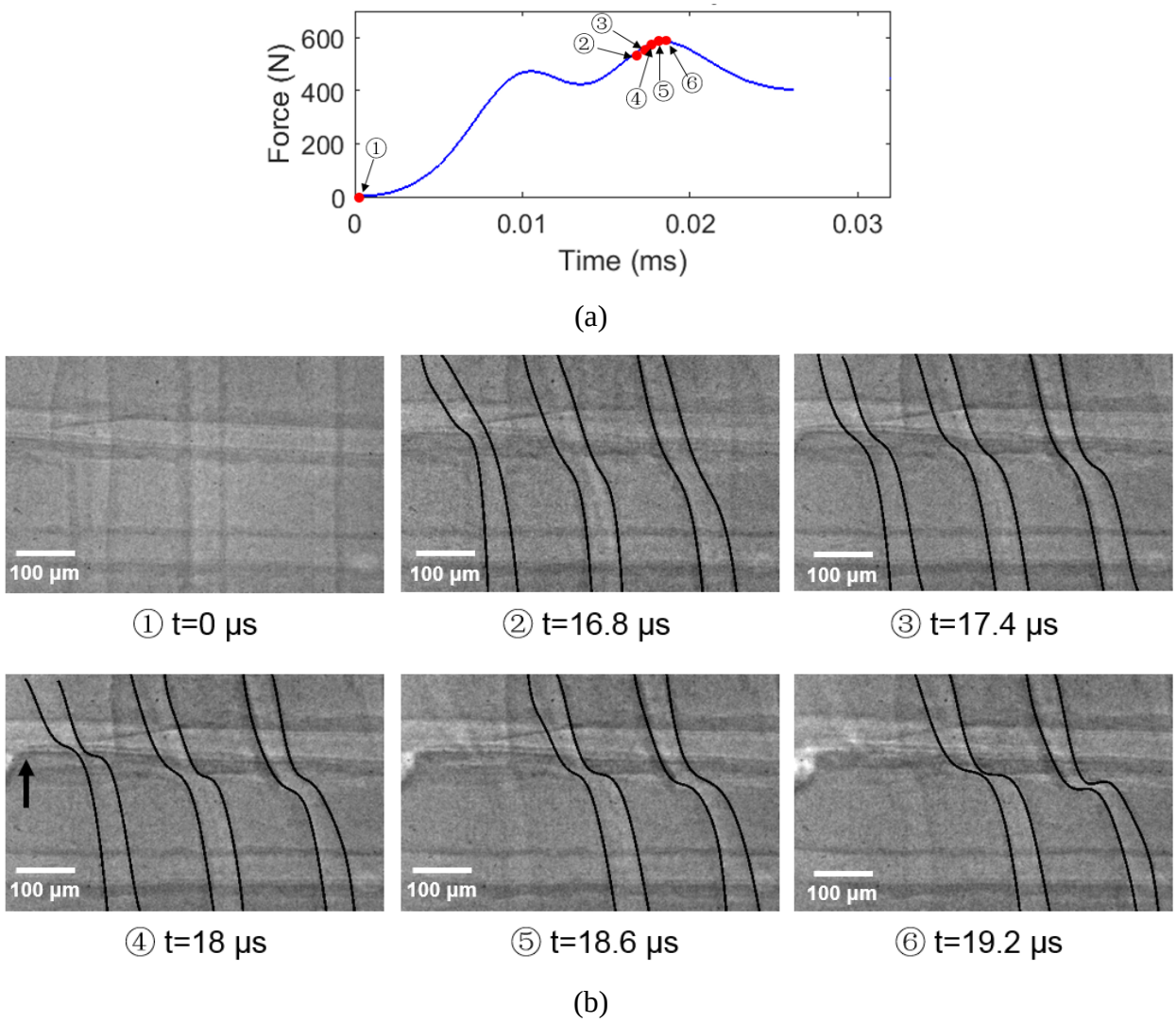

Figure 2.7. (a) The force-time graph and (b) the corresponding image sequence of a representative dynamic shear experiment on aluminum 7075-T6. Lines are tracked and marked to show the shear deformation.

The temperature field measurements on aluminum 7075-T6 during the dynamic shear were performed without X-ray PCI. The high-speed infrared camera measured the specimen temperature from the direction perpendicular to the specimen plane and the loading direction. The experimental conditions were identical to the experiments as shown in Figure 2.7. The results on the temperature field evolution on the shear band are shown in Figure 2.8. Due to the limitation in the frame rate, only two to three images are captured during the loading phase. The loading begins at t = 0 μs. At t = 16 μs, a thin band of temperature increase can be observed initiating from both edges of the specimen due to the shear deformation. The temperature is approximately 450 K along the region. At t = 31 μs, the image shows a peak temperature of 720 K in the center of the gage section. From Figure 2.7 we know that the shear band has already formed at this strain level. Therefore, even though the number of thermal image frames is still limited, the images in Figures 2.7 and 2.8 indicate that the shear bands initiate from both edges, propagate towards each other, and meet at the center, where the peak temperature is captured. At t = 47 μs, the high temperature zone has split into two in the vertical direction, which indicates that the material has separated across the shear band. The force history also shows the material has already failed at this time. The residual heat requires time to dissipate into the material, which results in a gradually decreasing temperature and a shrinking zone in the last two images, when the force has already reached zero.

The thermal experiments are repeated four times, whereas, as mentioned earlier, the X-ray imaging experiments on aluminum 7075-T6 are repeated five times. The force-displacement behaviors for the experiments are presented in Figure 2.9. Although the graph shows a scatter of ~20%, all the results show a similar trend. The shear bands initiate when the displacement is approximately 0.2 mm, where the force has not reached the maximum. The observed failure modes are consistent among all the experiments. For the temperature field measurements, the images are not directly comparable with the X-ray images, since the time when recording starts varies from each experiment and the images are captured at different time frame during the loading. However, all the results indicate the same band width of ~100 μm in which the temperature is over 600 K.

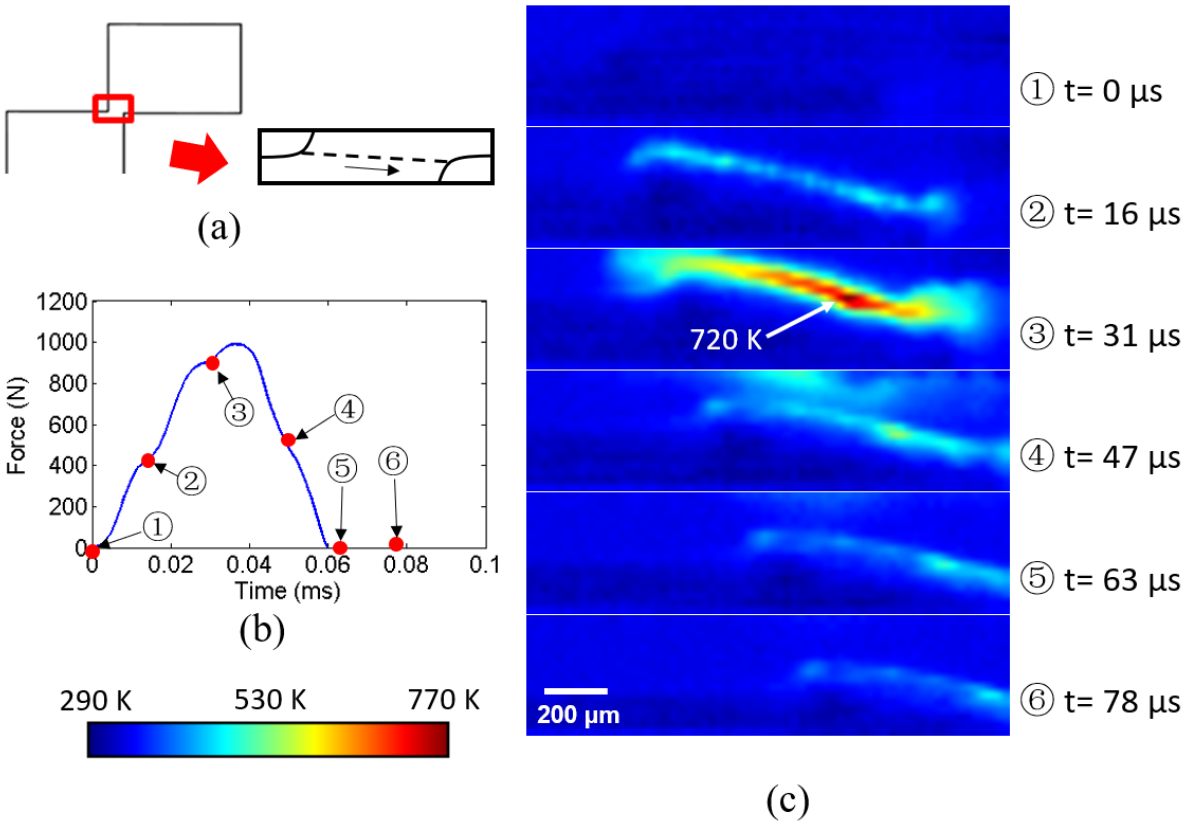

Figure 2.8. A representative force-time relationship and the corresponding thermal image sequences of aluminum 7075-T6. (a) The location of the camera window. (b) The force-time graph. (c) The thermal image sequence showing the temperature field on the material surface.

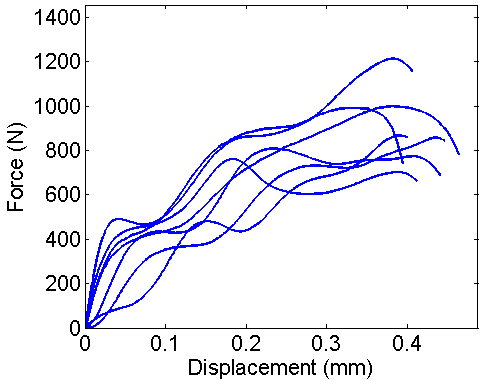

Figure 2.9. The force-displacement curves of aluminum 7075-T6.

2.2.2 Aluminum 6061-T6

Experiments under identical conditions were conducted on aluminum 6061-T6 to compare the material properties with 7075-T6. The force-displacement relationship and the high-speed image sequence of a representative experiment are presented in Figure 2.10. When loading starts, the specimen first adjust itself for better contact with the bar end and the fixture. At t = 16.4 μs, the material deforms uniformly and the maximum shear strains along all lines are measured as approximately 0.9. At t = 17.8 μs, the shear deformation becomes localized along the left two lines, showing the shear strain of 1.4. When loading continues, the shear band can be clearly seen initiating from the left side referring to the razor-blade carved grooves (t =19.2 μs). At t = 20.4 μs, the shear band is horizontal in the lower area of the image, with the average maximum shear strain of 3.2 along the band. A crack also initiates from the location indicated with an arrow. This crack later propagates along the shear direction (t = 21.6 μs). The force reaches a small plateau at this point, but has not reached the maximum of the entire loading history. Similar to the experiments with 7075-T6, no significant shear deformation is found in vertical direction according to the straight horizontal lines in all six images.

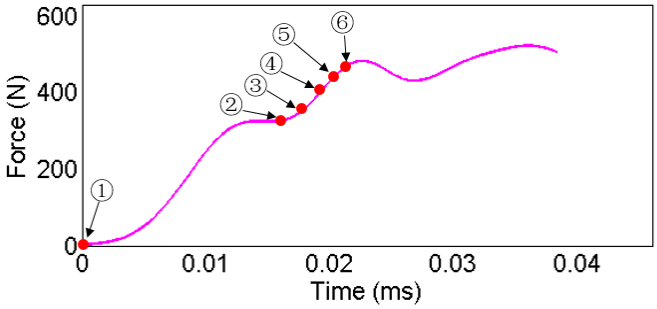

(a)

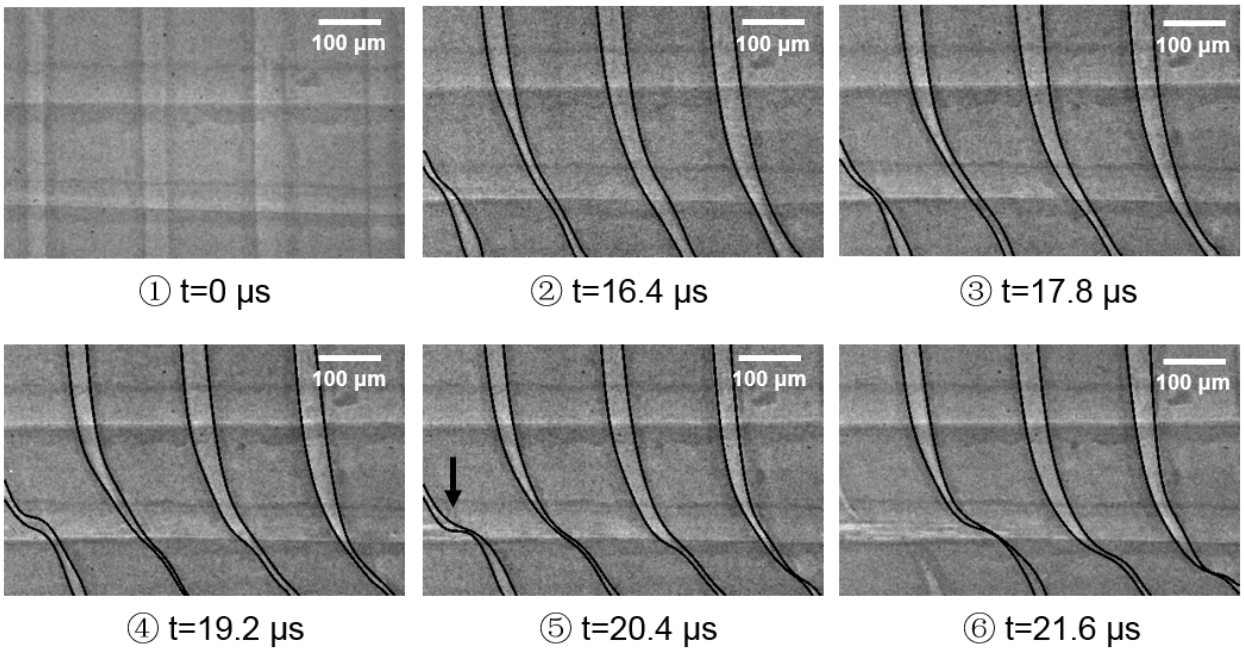

(b)

Figure 2.10. (a) The force-time graph and (b) the corresponding image sequence of a representative dynamic shear experiment on aluminum 6061-T6. Lines are tracked and marked to show the shear deformation.

The infrared thermal imaging results of 6061-T6 are arranged in Figure 2.11. The compression loading begins at t = 0 μs. At t =16 μs, there emerge two high temperature zones from both edges of the specimen with almost the same temperature of around 600 K. These two peaks propagate towards each other and become closer at t = 31 μs. This observation again reveals the processes of shear band formation and propagation. The calculated temperature also reaches a maximum of 770 K where the two tips meet. Then at t = 47 μs, the force reaches the maximum and the material fails. The heat can be seen gradually dissipating to the adjacent regions in the last 4 images. The lower part of the specimen is pushed out of the window by the incident bar.

Note that only one representative experimental result of aluminum 6061-T6 from five repeated experiments is presented here. The force-displacement curves are shown in Figure 2.12, which show good repeatability among the results. The measured temperature fields were also consistent across the repeated experiments. The highest calculated temperature is in the range of 600 K to 770 K and the band width is ~160 μm in which the temperature is over 600 K.

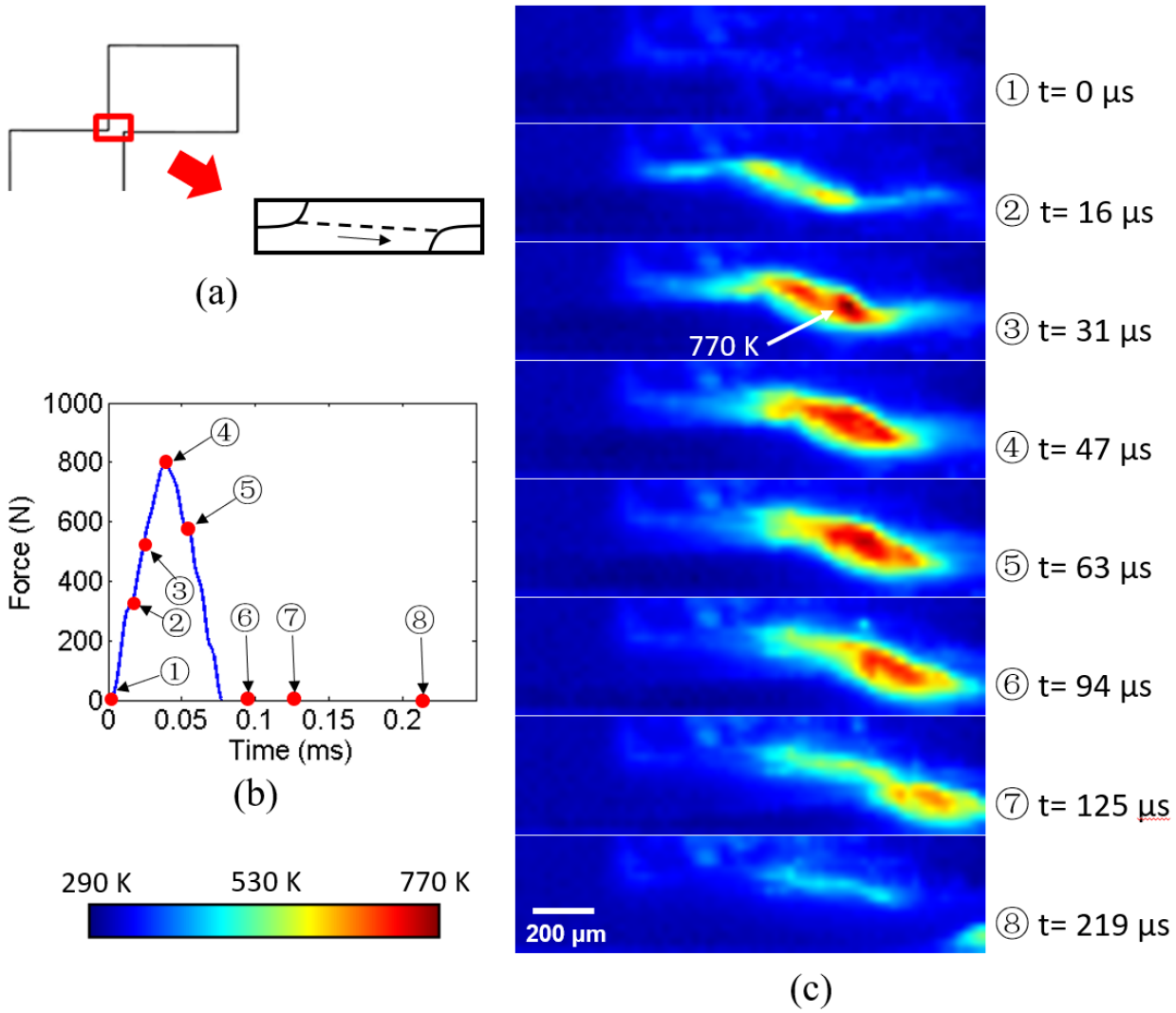

Figure 2.11. A representative force-time relationship and the corresponding thermal image sequences of aluminum 6061-T6. (a) The location of the camera window. (b) The force-time graph. (c) The thermal image sequence showing the temperature field on the material surface.

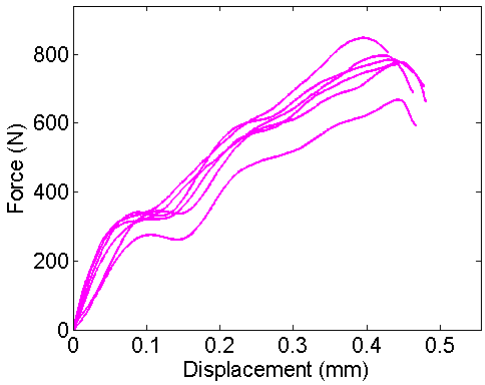

Figure 2.12. The force-displacement curves of aluminum 6061-T6.

2.3 Discussion

In order to estimate the thermal conduction near the localized shear zone, the temperature in the shear band can be assumed uniform. Therefore heat diffusion is only considered in the normal direction away from the shear band. The condition is then simplified as one-dimensional. The simplified heat equation is given as

$$\alpha \frac{\partial^2 T}{\partial x^2} = \frac{\partial T}{\partial t} \tag{2.4}$$

where T is the temperature and α is the thermal diffusivity of the material. For the aluminum 7075-T6, the thermal diffusivity is reported to vary from 0.65 to 0.75 cm^2/s when temperature is changing from 300 K to 800 K [63]. Here α is chosen as 0.7 cm^2/s. Similarly, α can be estimated as 0.75 cm^2/s for aluminum 6061-T6. To simulate the case where the shear band has been fully developed, the boundary condition is taken as infinite long solid with no heat generation inside. Considering the extreme case that the temperature is initially equal to the peak temperature found in the infrared experimental results, the heat equation has the following solution:

$$T(x,t) = T_s + \frac{T_0 - T_s}{2\sqrt{\alpha \pi t}} \int_{-1}^{1} \exp\left[-\frac{(x/d - u)^2}{4\alpha t} \right] du \tag{2.5}$$

where T_0 is the peak temperature, T_s is room temperature and d is the half shear band width. Figures 2.13 and 2.14 show the heat distribution within 7075-T6. Although it is initially room temperature outside the shear band, the heat conduction to the adjacent area is negligible given that the shear band formation takes less than 100 μs. Therefore the adiabatic condition applies. The result for 6061-T6 is very similar since the material properties and peak temperature are close to those for 7075-T6. The temperature dependence is discussed in [1] that the material will show lower stress in adiabatic condition than in isothermal condition. Given temperature rise close to the material melting temperature, the material is considered to undergo significant thermal softening.

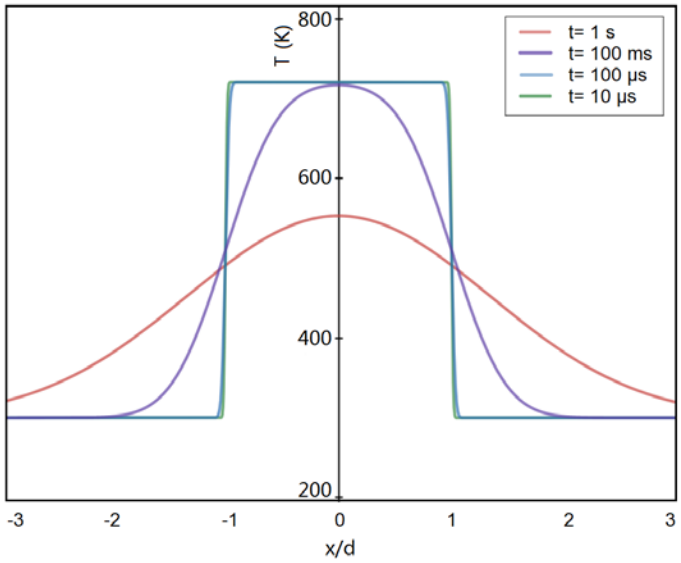

Figure 2.13. Temperature distribution in aluminum 7075-T6 at different time after the adiabatic shear band formation. *d* is half of the shear band width.

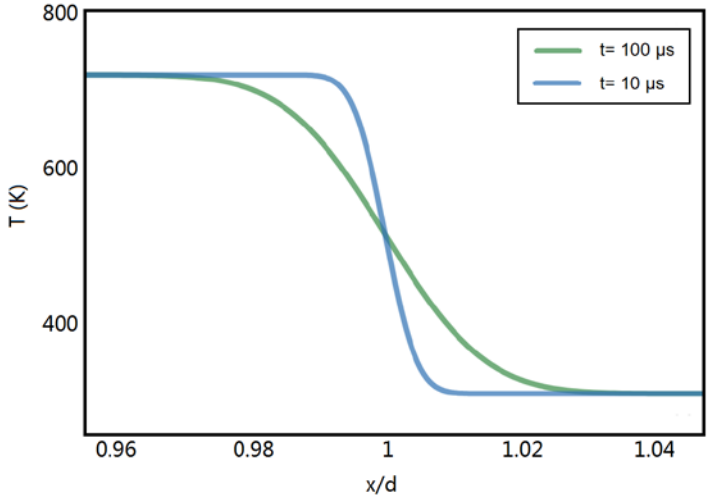

Figure 2.14. A detailed view of the temperature distribution in aluminum 7075-T6 at 10 µs and 100 µs after the adiabatic shear band formation. *d* is half of the shear band width.

Both 7075-T6 and 6061-T6 show shear banding behaviors and similar temperature response. Based on the high-speed X-ray images, 7075 is found to be more brittle than 6061 under dynamic shear. In 7075, the shear bands and cracks initiate shortly after localized shear

deformation is present, while 6061 exhibit larger shear strain than 7075 when the shear band forms. The shear banding behaviors are found before the force reaches the maximum. These findings are in accordance with the thermal images, where 7075 has a peak temperature at t = 31 μs and 6061 still has two peaks propagating in the same time frame. By correlating the timing of X-ray and thermal images for both aluminum alloys, the temperature can be shown to reach peak values after the observation of shear bands, which is considered to be the result of the insufficient thermal camera frame rate. Considering the nature that the events of maximum temperature and shear band formation are very close to each other, a higher frame rate for temperature measurement is desired to determine the exact time of the temperature rise.

Both aluminum alloys reach very high temperature during the dynamic loading with 720 K for 7075 and 770 K for 6061. As shown in Figure 2.6, the emissivity is taken as a constant of 0.15. Considering that the melting point for 7075-T6 is approximately 750 K and 850 K for 6061-T6, the materials were locally close to melting status. The difference in melting points can also be a reason that 7075 showed lower overall temperature response than 6061. The shear band width is also an important quantity to study. However, both materials exhibit very narrow ASB. The precise measurement is difficult due to the limit of the spatial resolution. Based on the presented X-ray and thermal images, the shear band width can be safely estimated as 20-50 μm for 7075-T6 and 30-70 μm for 6061-T6 before cracks form. Since the formation of the shear band takes less than 100 μs, the thermal conduction length can be found to be 0.01 – 0.02 of the half shear band width *d*, according to Figure 2.14. The thermal conduction length is in the order of 10^2 nm. This thermal conduction length is so small that the material inside the shear band is considered to be in adiabatic condition. The induced strain softening makes the material locally weaker than the adjacent area that are unaffected by the temperature rise. Therefore the deformation is concentrated within this localized region, forming the adiabatic shear band.

2.4 Summary

Aluminum 7075-T6 and 6061-T6 were studied in this chapter under dynamic shear loading. The flat hat-shaped specimen geometry was adopted with an impact speed of ~16 m/s. Both materials presented the trend of uniform shear deformation, formation of shear bands, cracking and then shear failure. 6061-T6 is more ductile and requires larger strain to form ASB. The temperature fields were measured using a high-speed infrared thermal camera. By assuming the emissivity to be 0.15, the maximum temperature during the loading was found to be 720 K for 7075-T6 and 770 K for 6061-T6. This heat accumulation and the corresponding thermal instability during dynamic loading were found to be closely related to the formation of the ASB. Both X-ray and thermal imaging in this research give useful information in determining the shear band width and tip location. The shear band width is estimated as 20-50 μm for 7075-T6 and 30-70 μm for 6061-T6. The cracks initiate after shear bands form and propagate in the same tracks as the shear bands at approximately 1100 m/s.

3. DYNAMIC TEMPERATURE EVOLUTION USING LASER PHOSPHORESCENCE THERMAL IMAGING: LIFETIME METHOD

Considering the limit of spatial and temporal resolution of infrared techniques, high-speed laser phosphorescence becomes widely used in measuring temperature field in both fluids and solids. The spatial resolution is no longer limited by the infrared wavelength, but solely depends on the high-speed optical camera, which can easily reach kHz or MHz frame rate with current technology. The temporal resolution is dependent on the high-speed camera, the laser pulse rate and the luminescence properties of the phosphor. In this chapter, an experimental technique which synchronizes laser phosphorescence with a compression Kolsky bar setup is developed for the thermometry during dynamic loading of aluminum alloys. Europium-activated Lanthanum Oxysulfide (La_2O_2S:Eu) phosphor is used with lifetime method to investigate the temperature evolution of aluminum alloy 7075-T6 under dynamic shearing. The results shows temperature response with large error after the image processing, which is mainly caused by the specimen motion during the dynamic loading. Finally, the capability and limit of this lifetime method is discussed.

3.1 Experimental Methods

3.1.1 Specimen preparation

The material and specimen studied in the dynamic shearing experiments is flat hat-shaped aluminum alloy 7075-T6, which is identical to the specimen information discussed in Chapter 2.1.1. Prior to the experiments, the specimens are coated with La_2O_2S:Eu phosphor powder (Phosphor Technologies Ltd., Stevenage, UK) on the imaging surface. The phosphor is first evenly mixed with HPC Binder (ZYP Coatings, Inc.) with a mass ratio of 1:5. An Iwata airbrush (Anest Iwata-Medea, Inc, Portland, OR) is used to uniformly spray the mixture with compressed air onto the specimen surfaces for 5 seconds. The specimens are then left to dry for 24 hours so that the moisture is evaporated and only the phosphors are attached to the material surface securely.

3.1.2 Phosphor thermography

Europium-activated Lanthanum Oxysulfide (La_2O_2S:Eu) is chosen as the thermographic phosphor material due to its high sensitivity when used with lifetime method to investigate the temperature evolution of aluminum alloy 7075-T6 under dynamic shearing. The phosphor is excited with the third harmonic of an custom-built Q-switched Nd:YAG burst-mode laser at 355 nm using 10 ns pulses. La_2O_2S:Eu is shown to give a strong temperature sensitivity at low temperature of emission at 514 nm, 538 nm and 624 nm when transiting from the $^5D_2$, $^5D_1$ and $^5D_0$ states, respectively [64]. Figure 3.1 shows the emission intensity of La_2O_2S:Eu versus the excitation spectra at different wavelengths. It is clear that the emission at 624 nm has the highest intensity in the excitation range of 200 – 400 nm. The laser wavelength of 355 nm is near the highest intensity possible. Therefore the 355 nm laser with 624 nm phosphorescence emission are chosen in this study so that the signal strength can be maximized for emission collection. When further taking an observation in the temperature domain, as shown in Figure 3.2, the 624 nm emission wavelength of La_2O_2S:Eu is sensitive from 200 – 300 °C. Although this temperature range does not cover the entire desired measuring range starting from room temperature, it should still show high temperature peaks. The laser beam is adjusted through a 355 nm notch filter and a UV fused silica diffuser prior to reaching the specimen so as to create a uniformly distributed beam profile. The energy of the laser burst is measured and averaged over ten bursts to calculate the average laser pulse energy delivered to the specimen. The average burst energy is then divided by the number of pulses in the burst to determine an average pulse energy. For the experiments in this chapter, the laser is operated at 20 kHz and the average pulse fluence is maintained below 7 $\mu J/cm^2$.

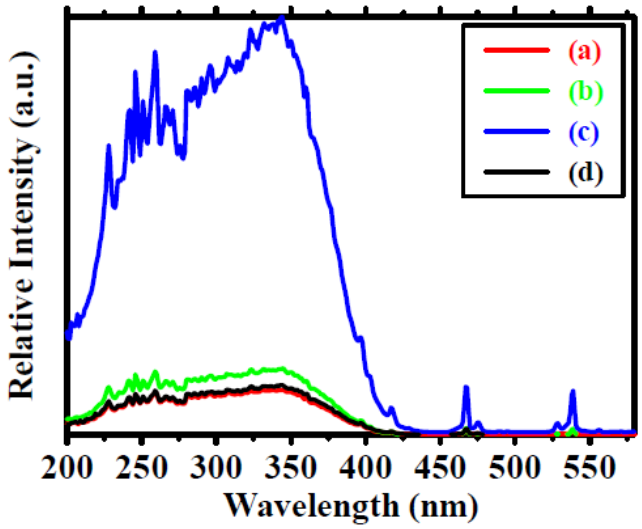

Figure 3.1. Excitation spectra of the (a) 594 nm, (b) 616 nm, (c) 624 nm and (d) 704 nm emission lines of La_2O_2S:Eu [65].

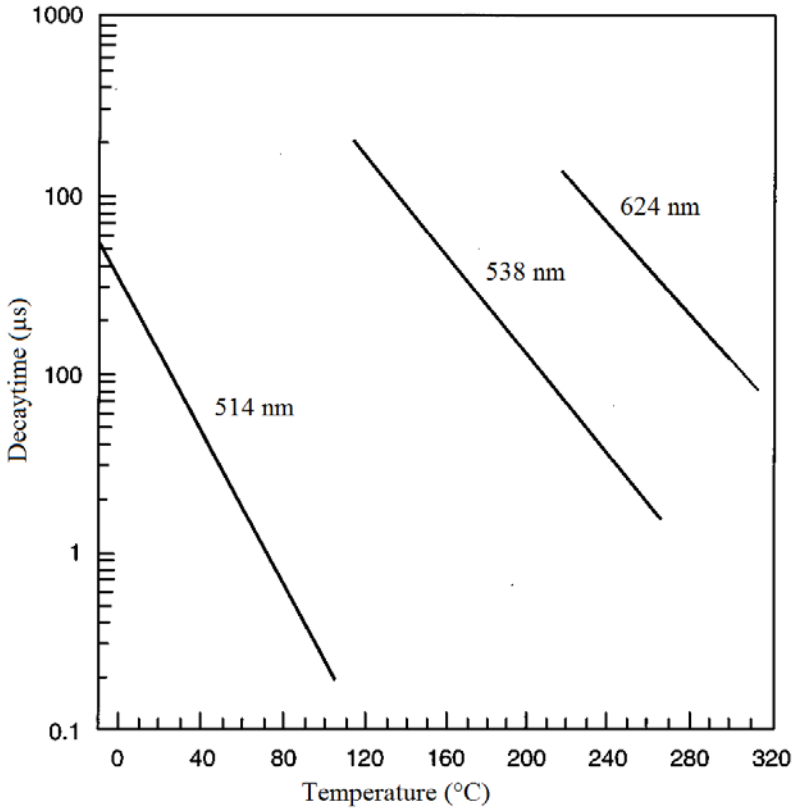

Figure 3.2. Fluorescence decay time vs temperature for La_2O_2S:Eu. Reproduced from [34]

3.1.3 Dynamic loading with laser phosphorescence thermal imaging

The dynamic loading of the material is realized by employing a compression Kolsky bar. This experimental setup for the Kolsky bar part is identical to the setup introduced in Chapter 2.1.2. The Kolsky bar in this chapter is developed to synchronize with the laser and the imaging system, as shown in Figure 3.3. The system is built and aligned on an aluminum base as a station for the ease of setting up. The incoming laser is reflected by the mirrors and through a diffuser prior to exciting on the phosphor coated specimen. The emitted light is passed through a 10× lens and a high speed IRO intensifier (LaVision GmbH, Göttingen, Germany) so that sufficient signal can be collected by the camera. Finally, a Shimadzu HPV-X2 high-speed camera is used to capture the phosphorescence images at 200 kHz with 4 μs exposure time. This frame rate is ten times higher than the laser pulse frequency so that after each laser excitation, ten images will be taken to fit the decay curve at corresponding temperature. A photograph of experimental setup is presented in Figure 3.4.

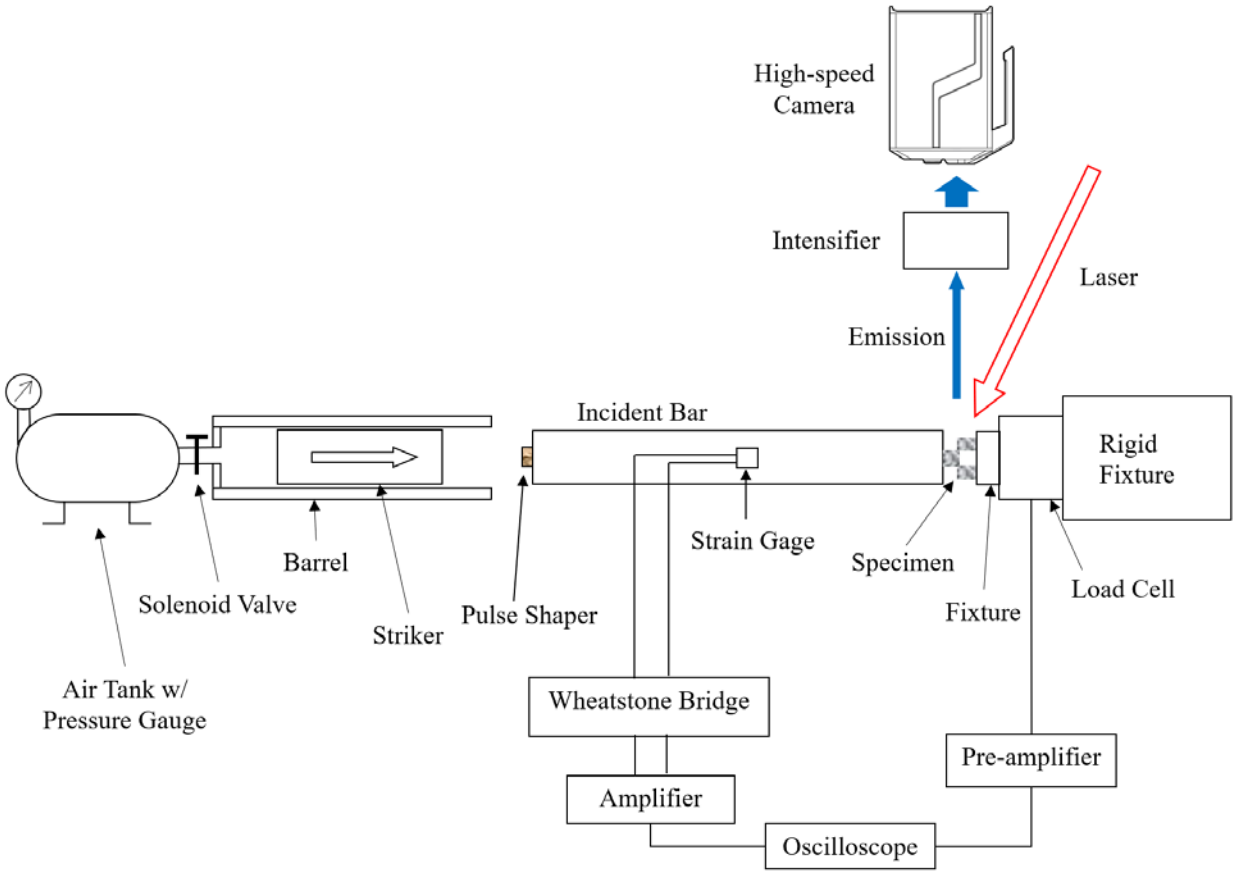

Figure 3.3. Kolsky bar setup with high-speed laser phosphorescence thermal imaging.

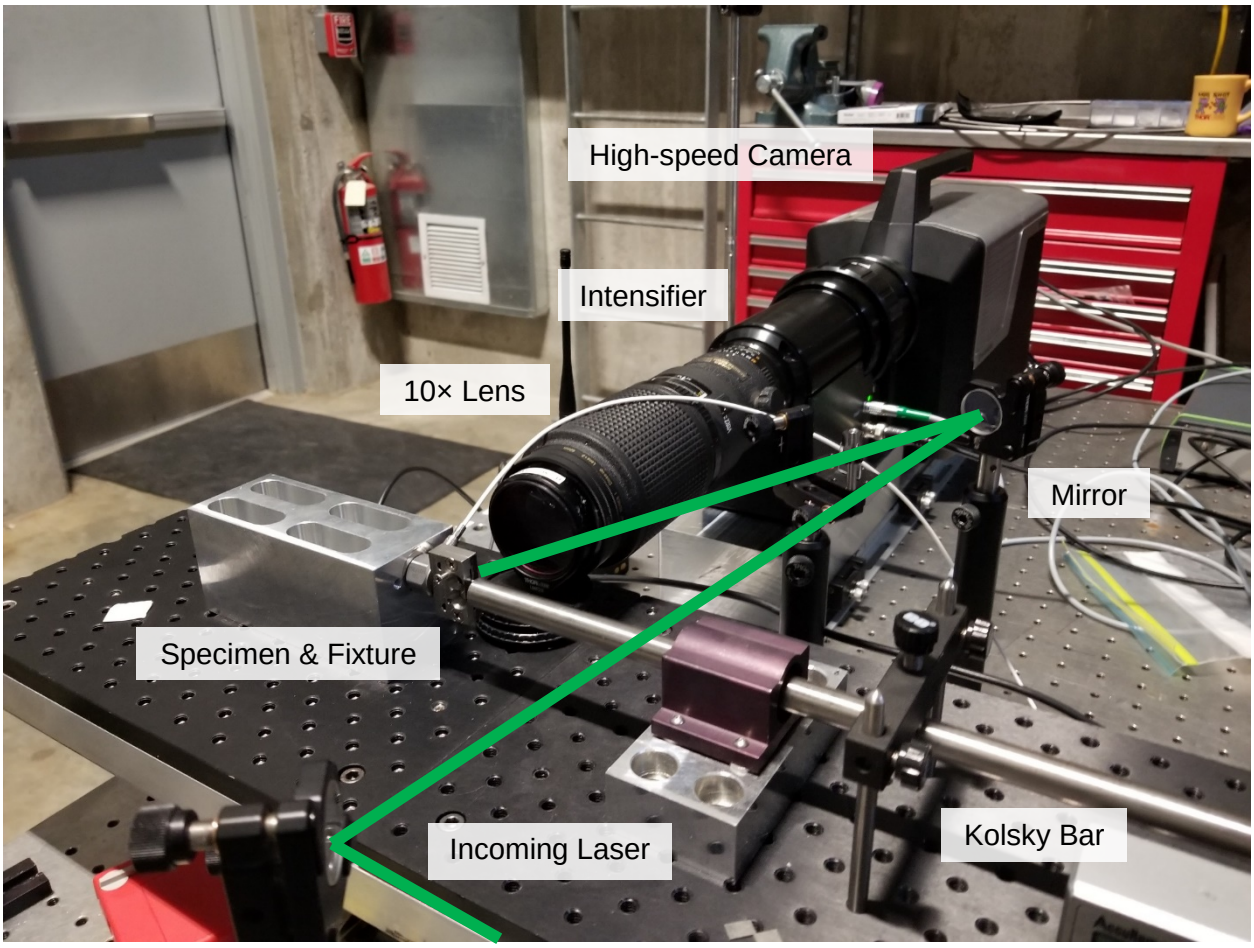

Figure 3.4. A photograph showing the laser and imaging system setup with Kolsky bar.

3.1.4 Temperature calibration and image processing

A proper temperature calibration is necessary to process the measured temperature results. As presented in Figure 3.5, an aluminum calibration specimen, after coated with La_2O_2S:Eu, is placed inside a temperature controlled oven. The oven is optical accessible with quartz window on each side. The incoming laser is 90° to the camera central axis while the specimen surface is approximately 45° to either of them. The camera frame rate and exposure time are kept the same as the experimental values in order to simulate the real experimental condition. The specimen temperature is monitored with a type K thermocouple as the intensity decay are measured at different oven temperatures. The thermocouple is kept in contact with the specimen surface and oven temperatures are allowed to stabilize before the images are taken.

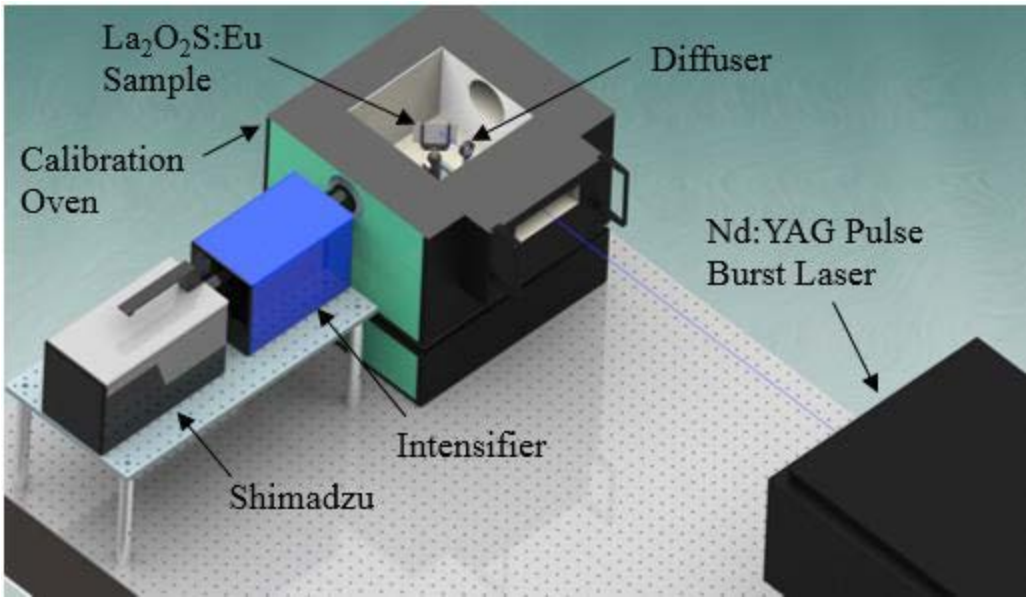

Figure 3.5. The setup for temperature calibration of lifetime method.

3.1.5 Image processing

The 256 images taken for each experiments are first divided into 25 groups with every ten images after a laser pulse in each group. The first several frames displayed increased signal intensity, resulting in a decreased time constant and higher temperature. Therefore the first set of tem images are discarded in each experiments. The images are then normalized by the static images to account for the spatial irregularities. An image registration code is used to register each pixel through the ten images according to its relative location. Then each set of the pixel values are fitted into one single exponential decay curve. By using Equation (1.2), the lifetime τ of the phosphor at the specific pixel location is calculated. Finally, the lifetime τ at each pixel is related to the corresponding temperature value with the calibration curve.

3.2 Experimental Results

The temperature field measurement during shear banding is investigated in this chapter using phosphorescence lifetime method with aluminum alloy 7075-T6. A representative experimental record from oscilloscope is illustrated in Figure 3.6 and the corresponding force-time and force-displacement history are presented in Figures 3.7 and 3.8, respectively. The specimen was loaded at 16 m/s and the force response reaches 650 N at 25 μs. It can be observed from the laser pulse that only one temperature measurement is made during the dynamic loading due to the pulse rate of the laser.

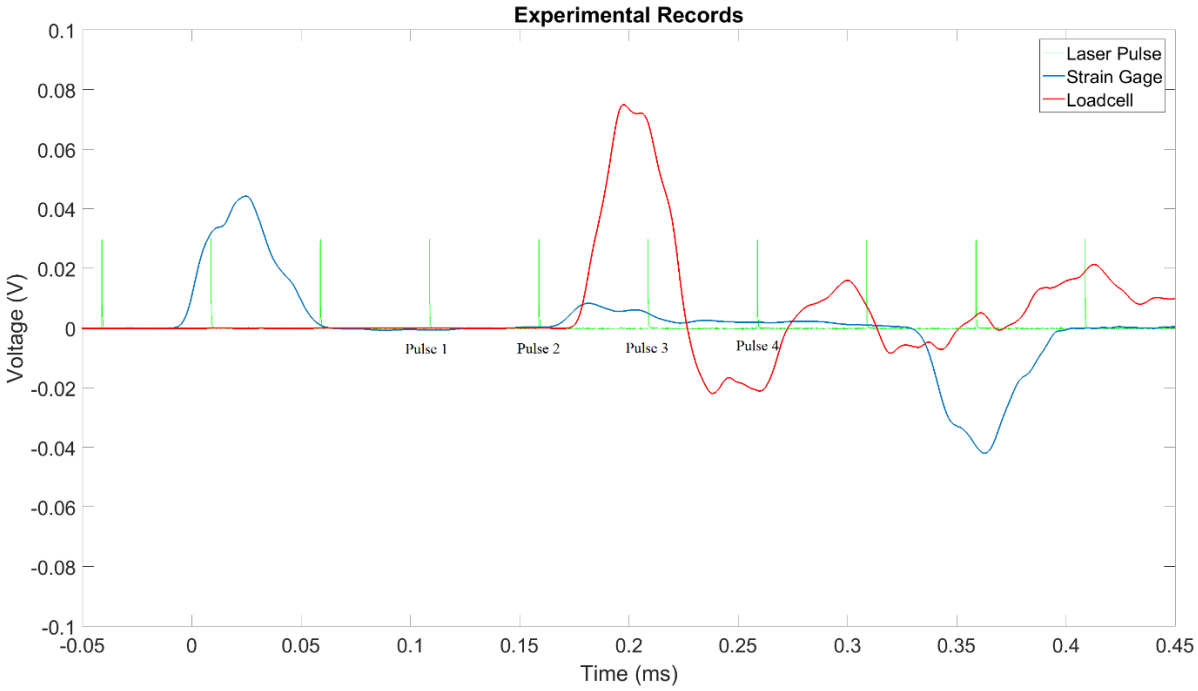

Figure 3.6. A typical experimental record showing strain gage, load cell and laser signals.

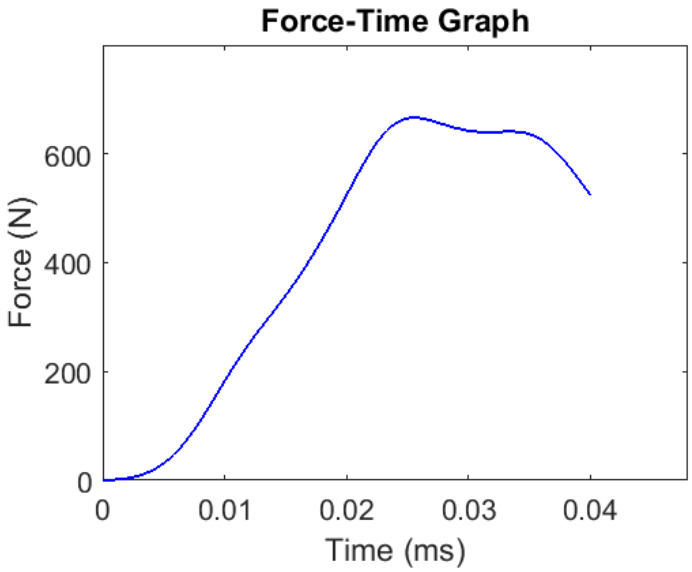

Figure 3.7. A representative force-time relationship of aluminum 7075-T6.

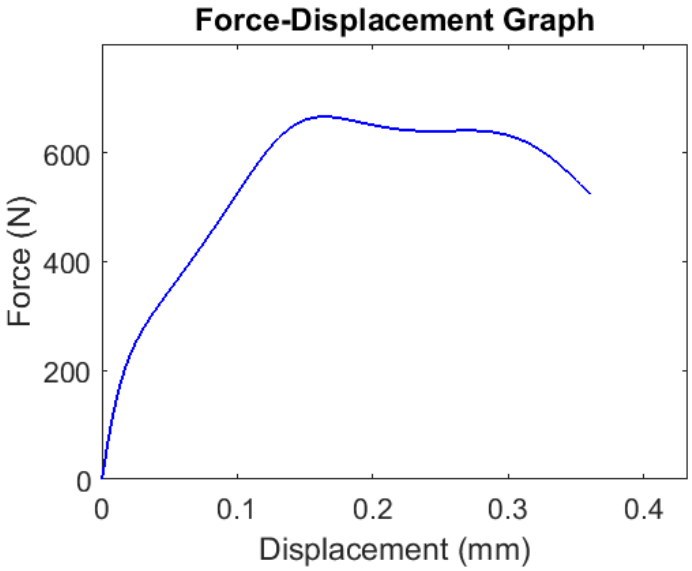

Figure 3.8. A representative force-displacement relationship of aluminum 7075-T6.

The results of temperature field measurement during shear banding is presented in Figure 3.9, where the image numbers are indicated in Figure 3.6. Figure 3.9(a) clarifies the location of the image window, which is at the lower connection area of the specimen. During the loading, the upper side shown in the images will be moving due to the impact and the lower side is supported by the fixture to the right of the image. The image of Pulse 1 represents the initial temperature

field before the dynamic loading, a nearly constant temperature distribution is observed among the surface, despite some pixels showing high temperature on the edge, which is believed to be the error caused by boundary effect. The temperature field of Pulse 2 is integrated during the entire dynamic loading. The specimen undergoes large deformation of 0.15 mm during the ten high-speed image frames used for the integration, according to Figure 3.8. This deformation is equivalent to 20 pixels during the ten frames, or 2 pixels/frame. The image registration is unable to account for this change in the relative pixel position from frame to frame. Although temperature increase is detected within the shear zone, incorrect pixel values are taken and the temperature field shows high temperature distribution even in the adjacent areas far from the shear zone. At Pulse 3, the material undergoes unloading and more areas show missing pixels. The absence of the pixels in the image indicates either the saturation of pixel values or the failure in fitting the decay curve to find the temperate, which is more likely to be the latter in this case. At Pulse 4, loading is finished and the specimen has failed a larger area of pixel absence is present and the temperature within the shear zone of interest is unreadable. Note that the temperature showing are in the range of 150 – 280 °C, which is the sensitive range of the La2O2S:Eu phosphor. Temperature below this range still shows the lower bound because the lifetime of the phosphors is no longer in the proportional region as Figure 3.2 shows. Temperature above the sensitive range is shown as absent pixels because the program is unable to find lifetime using curve fitting.

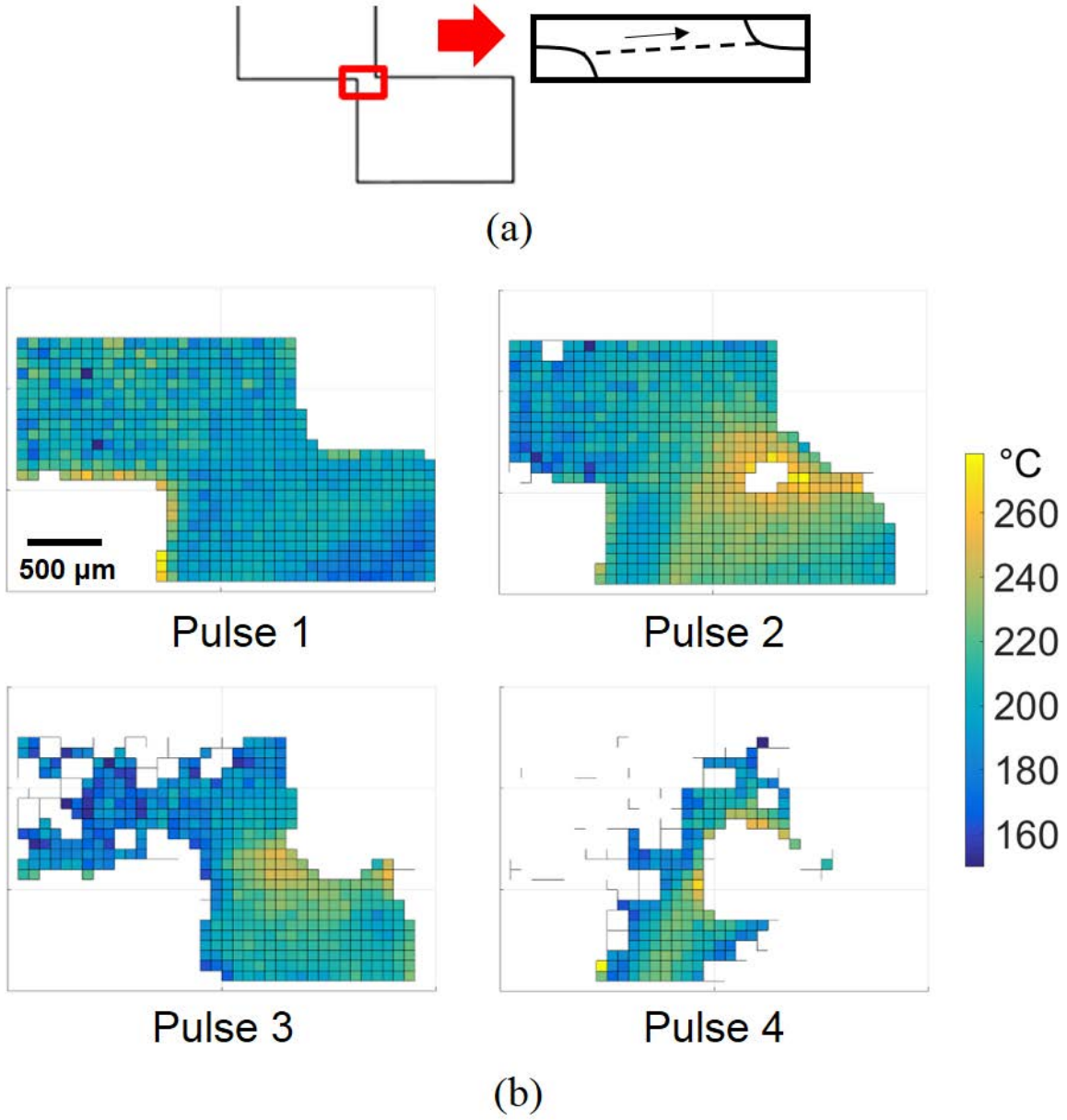

Figure 3.9. A representative temperature field image sequences of aluminum 7075-T6. (a) The location of the camera window. (b) The thermal image sequence showing the temperature field.

3.3 Discussion

The results of the temperature field measurement during dynamic shear of aluminum 7075-T6 show temperature increase but with a large error. When using lifetime method of phosphorescence, multiple image frames are to be taken in order to find the lifetime of one temperature point. For a temperature field measurement, each pixel is a temperature point. This means the local temperature or the lifetime of a specific location represented by a pixel need to be kept consistent during the set of image frames, which consists of 10 frames in this work. However, a displacement of approximately 2 pixels/frame is measured in Figure 3.9(b) and the temperature should be moving with the material. The pixels in the same position from the subsequent frame do not represent the same location on the material surface, nor the same temperature. Furthermore, the loading speed is increasing in the beginning and then reaches the maximum speed, leading to a change in the pixel movement amount. The nonuniform deformation field on the material surface also add up the uncertainty of pixel movement. Therefore having a proper registration of pixels with specimen movement is very challenging.

Measuring temperature of a high-speed moving object using ratio method is rarely reported in the literature. One representative technique is introduced by Allison et al. [37]. In order to measure the temperature of a motor spinning at an angular speed of 650 Hz, a ring of phosphor is applied to the rotor surface. As shown in Figure 3.10, the laser source is fixed at a certain location, followed by the fluorescence collecting fiber. After the excitation, the phosphor will emit light while moving into, through and out of the collecting region, which takes 10 – 30 μs. The measured emission intensity will decay during this time period, but follows a different decay curve, as shown in Figure 3.11. The curve of the rotating case is not only temperature-dependent but also angular speed-dependent. However, by calibrating the efficiency factor and correcting the experimental result with the calibrated curve, a decay curve which is only temperature-dependent can be achieved. The temperature of this rotating object can then be determined.

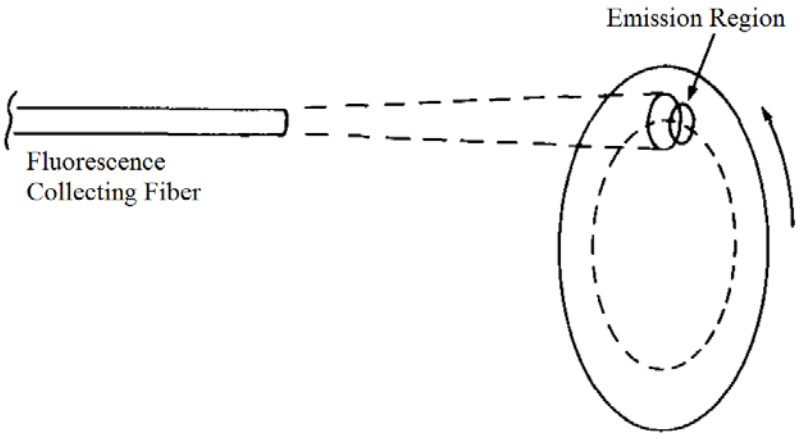

Figure 3.10. The rotation of the rotor causes the fluorescing spot to move with respect to the fluorescence collection fiber's input aperture. Reproduced from [37].

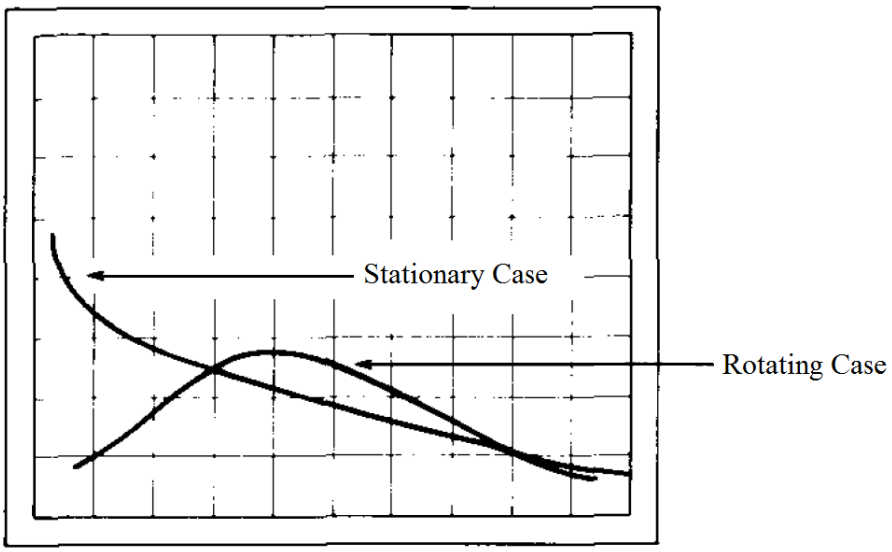

Figure 3.11. Qualitative oscilloscope signals of the fluorescence intensity from a stationary phosphor target and from the rotating target. Reproduced from [37].

The aforementioned technique solves the pixel motion issue by introducing a time-dependent efficiency factor to correct the decay curve. However, limitations are still present when applying this technique to our experiments. First of all, in the literature the measurement can be regarded as only one pixel, meaning that no phosphor is excited outside this pixel. In our case, the measurement is a temperature field consists of an array of pixels. Although the material of a certain

temperature is moving out of a certain pixel area, the adjacent material will move into and fulfill this pixel subsequently, with a possibly different temperature, which makes the correction not consistent as the adjacent phosphor has also been excited and emits light. Second, the rotating speed in the literature is a known constant. But the deformation speed in our case is time-dependent and also not uniform on the material surface. Finally, the temperature in this study keeps changing during every set of ten image frames, leading to additional challenges in curve fitting. With all being listed, the aforementioned technique is still deficient in providing an acceptable solution to the object movement issue associated with the lifetime method used in this work.

The limitation in the sensitive range of the phosphor is another issue. In Chapter 2.2, the maximum temperature during ASB formation in aluminum alloys are reported as 700 – 800 K. The thermal quenching region of La_2O_2S:Eu phosphor only covers 400 – 600 K range at 624 nm wavelength, according to Figure 3.2, meaning that the sensitive range is not wide enough for this application. Also, the camera frame rate is limited to 200 kHz due to the length of exposure needed. Then the laser pulse rate has to be reduced to 20 kHz so that ten images can be taken for each temperature measurement. This is a sacrifice of the capability of the high-speed camera. All in all, although lifetime method is more accurate in the temperature measurement, this method is not an ideal candidate for measuring the surface temperature field evolution during dynamic loading of solid materials.

3.4 Summary

The temperature field measurement of aluminum 7075-T6 during dynamic shearing is performed with laser phosphorescence. La_2O_2S:Eu phosphor material with lifetime method is used in this study. A 355 nm laser is used as the excitation source with a pulse rate of 20 kHz. The results show large error in the measured temperature, which is primarily caused by two reasons. One is the deformation of the specimen which results in the error in pixel registration to find the intensity decay curve. The other reason is the inadequate sensitive range of the phosphor material which provides only part of the temperature reading with regard to the real temperature field evolution. Further, lifetime method requires that the temperature can only be measured at a reduced rate of the frame rate of the high-speed camera, which greatly limit the improvement of the

temperature recording speed with the existing equipment. Therefore lifetime method is not suitable for measuring the surface temperature field evolution during dynamic loading of solid materials. A method that is not time-resolved and can accommodate the temperature increase from room temperature to 800 K is highly desired.

4. DYNAMIC TEMPERATURE EVOLUTION USING LASER PHOSPHORESCENCE THERMAL IMAGING: INTENSITY RATIO METHOD

Considering the limit of spatial and temporal resolution of infrared techniques, high-speed laser phosphorescence becomes widely used in measuring temperature field in both fluids and solids. An experimental technique which synchronizes laser phosphorescence with a compression Kolsky bar setup is developed for the thermometry during dynamic loading of metallic materials. In the previous chapter, high-speed temperature field measurement using lifetime method was studied but the results showed that the method was not ideal for use with dynamic loading of solid materials. In this chapter, another method — intensity ratio method of laser phosphorescence is studied. The temperature results of a C101 copper material under dynamic compression and aluminum alloy 7075-T6 and 6061-T6 under dynamic shearing are shown and discussed. Along with the experimental results, a temperature correction method is also proposed to correct the delayed measurement caused by the thermal conduction within the phosphor coating.

4.1 Materials and Methods

4.1.1 Materials and specimens

This chapter (Chapter 4) includes dynamic compression of copper and dynamic shear of aluminum alloys. For the compressive experiments, the material chosen is the commercially available C101 copper (United States Brass & Copper, Downers Grove, Illinois). Some of the material properties of C101 are summarized in Table 4.1. The material is cut into 2.5 × 6.35 × 6.35 mm blocks as specimens using an IsoMet™ 1000 precision sectioning saw (Buehler, Lake Bluff, Illinois). The loading direction is along the 6.35 mm dimension. For the shearing experiments, the specimens are the same as introduced in Chapter 2.1.1.

Table 4.1 Material properties of C101 copper

Density	8940 kg/m^3
Melting point	1356 K
Thermal conductivity	391.1 W/m·K
Surface hardness	Rockwell F75

Prior to the experiments, the specimens are coated with $BaMgAl_{10}O_{17}:Eu^{2+}$ (BAM:Eu) phosphor powder (Phosphor Technologies Ltd., Stevenage, UK) on the imaging surface. The phosphor is first evenly mixed with HPC Binder (ZYP Coatings, Inc.) with a mass ratio of 1:5. An Iwata airbrush (Anest Iwata-Medea, Inc, Portland, OR) is used with compressed air to uniformly spray the mixture onto the specimen surfaces for 5 seconds. The specimens are then left to dry for 24 hours so that the water-based solvent is evaporated and only the phosphors are attached to the material surface securely. Figure 4.1 shows the cross-sectional area of one of the aluminum 7075-T6 specimens. The phosphor coating layer can be observed evenly attached to the material surface. The thickness of the coating is measured as approximately 7 μm for all aluminum specimens and 5 μm for all copper specimens. This coating thickness is consistent among all the specimens examined with the scanning electron microscope (SEM).

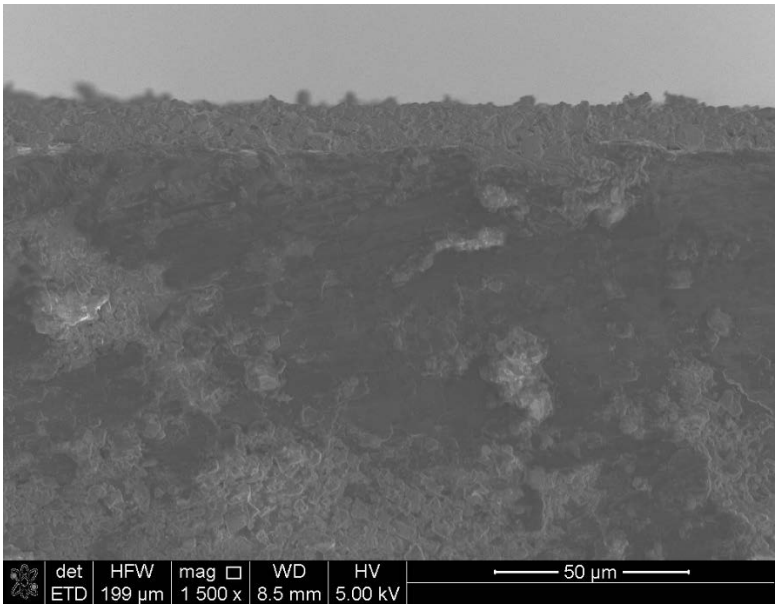

Figure 4.1. A microscopic image showing the phosphor coating layer.

4.1.2 Phosphor thermography

The phosphor chosen for this study is $BaMgAl_{10}O_{17}:Eu^{2+}$ (BAM:Eu) due to its wide temperature sensitivity range and relatively short lifetime of 1 µs at room temperature [66]. Upon excitation from a UV light source, BAM:Eu displays a broad phosphorescence peak, centered around 450 nm. The low-wavelength side of the spectrum blueshifts with increasing temperature, creating an opportunity for spectral ratio-based thermography. In this work, two filters are chosen at 400 ± 25 nm and 450 ± 5 nm and placed in a custom image doubler, attached to a high-speed CMOS camera. Figure 4.2 illustrates the image doubler layout, designed to divide the camera chip into two identical images of the same scale. As the phosphor temperature increases, the ratio of intensities imaged through the 400 nm filter to the intensities imaged through the 450 nm filter also increases. Given a known spectral response to temperature, the ratio can be correlated to temperature.

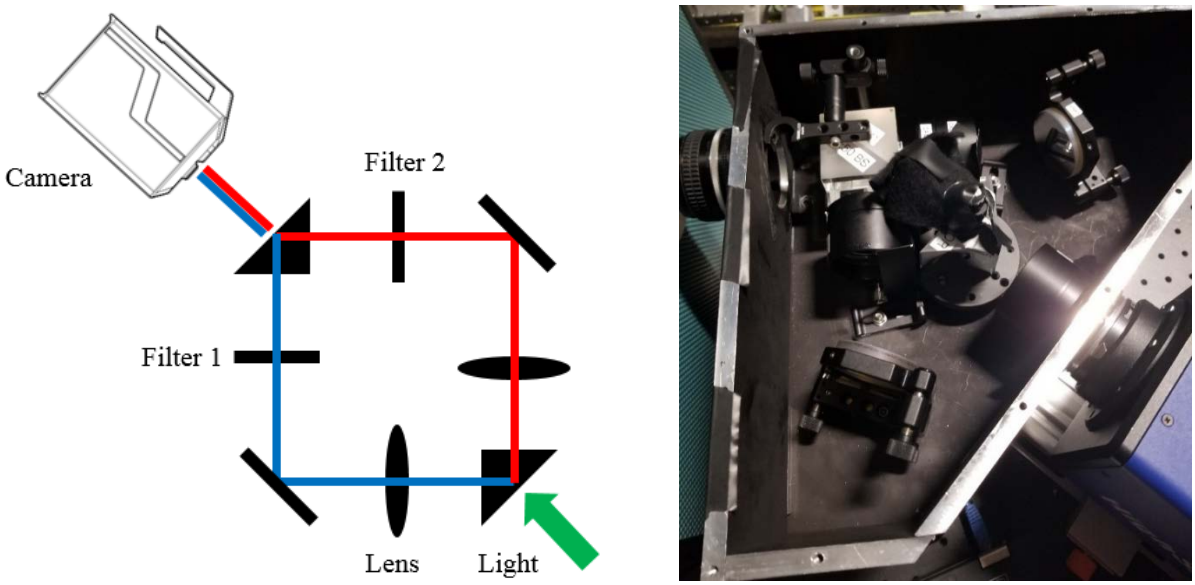

Figure 4.2. A schematic and a photograph showing the image doubler

The phosphor is excited using 10 ns pulses from the third harmonic of an in-house built Q-switched Nd:YAG burst-mode laser. The laser beam is directed through a top-hat UV fused silica ground glass diffuser prior to reaching the specimen in order to create an even beam profile. To

calculate the average laser pulse energy delivered to the specimen, the laser burst energy is measured over ten bursts and the readings are averaged. The average burst energy is then divided by the number of pulses in the burst to determine an average pulse energy. For the experiments in this study, the laser fluence is kept constant at ~ 93 μJ/cm^2.

4.1.3 Synchronization of the Kolsky bar and the laser phosphorescence thermal imaging

The dynamic loading of the materials is realized by employing a compression Kolsky bar. This experimental setup is the same as the Kolsky bar in Chapter 2.1.2. The Kolsky bar in this chapter is developed to synchronize with the laser and the imaging system, as shown in Figure 4.3. The system is built and aligned on an aluminum base as a station for the ease of setting up. A photograph of experimental setup is shown in Figure 4.4.

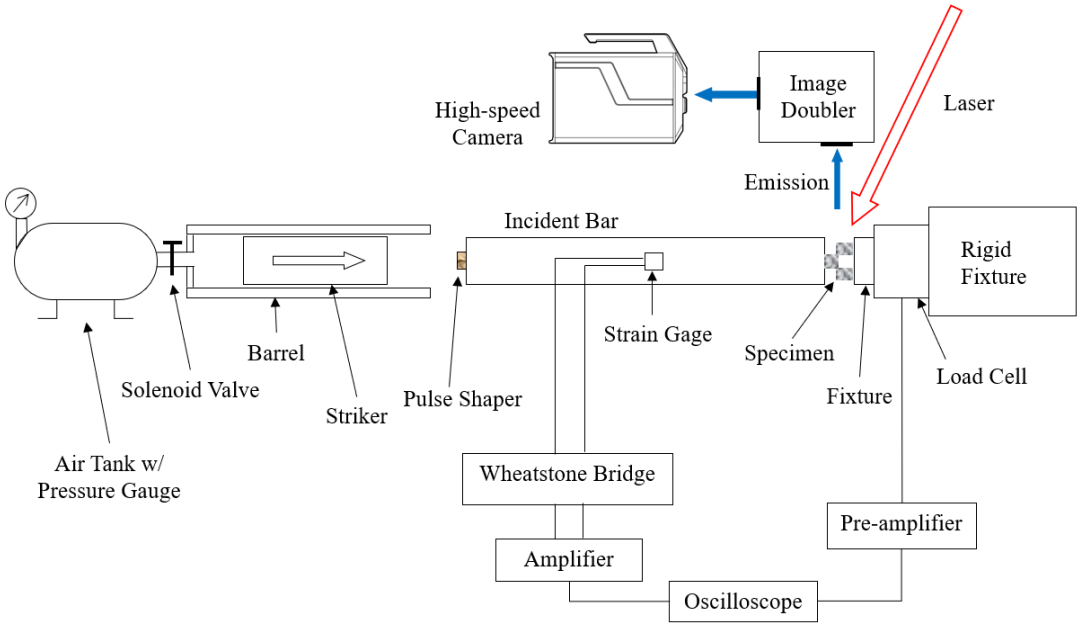

Figure 4.3. Dynamic compression setup with high-speed laser phosphorescence thermal imaging.

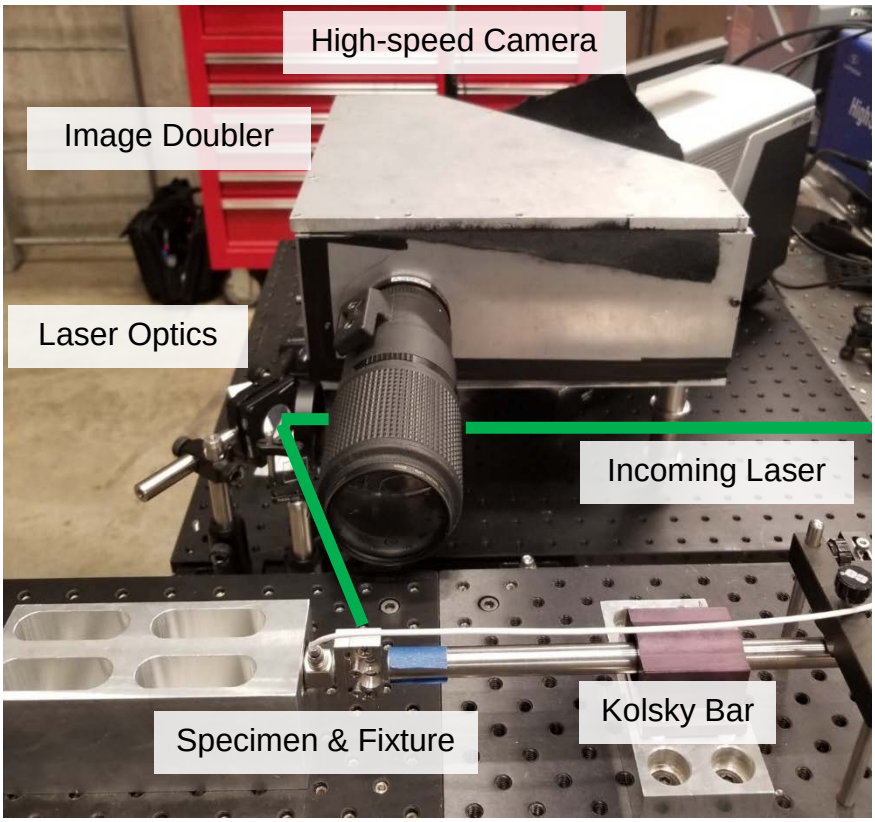

Figure 4.4. A photograph of compression Kolsky bar setup for laser phosphorescence thermal imaging.

The successful operation of the entire system is based on a carefully designed timing sequence of laser on/off window, Kolsky bar firing, loading event and camera triggering. The detailed the timing sequence is shown in Figure 4.5 and will be described as follows:

At t_0, a firing signal is sent from the control box to the FIRE solenoid valve to release the compressed air. This signal is also sent to the laser controller after a certain delay t_1-t_0 to trigger the laser. The laser pulses start at t_1 and will take t_2-t_1 to reach the designated energy. The t_2-t_1 here is found to be approximately 3 ms. Meanwhile, the striker moves and impacts the incident bar. At t_3, the strain gages record the incident pulse. This strain gage signal, together with the laser pulses, are both sent to the camera. The camera is triggered only when receiving the first laser pulse after the strain gage signal, which is at t_4. To obtain a decent image intensity, the camera frame need to be synchronized precisely with each laser pulse with a delay time t_5-t_4. This is realized by having a set delay time in the camera control software between the input trigger signal and the camera

triggering. Since the camera is operating at 200 kHz and can only record 256 images. The recording length t_8-t_5 = 1.28 ms, which is long enough to cover the loading of the specimen from t_6 to t_7. At last, the laser burst will stop when it reaches 10 ms, which indicates that t_9-t_1 = 10 ms. Therefore, as long as this 10 ms laser burst covers the specimen event, the experiment is well synchronized. However, the movement of the sticker is inevitably different from time to time, causing an uncertainty between t_3 and t_0, which further has an effect on the location of loading event regarding to the laser burst. Although the delay t_1-t_0 can be chosen by finding the statistical value of t_3, there still exists extreme cases that the t_3 is so large that it causes $t_6 > t_9$, meaning no images will be taken (t_3-t_0 is in the scale of 100 ± 7 ms).

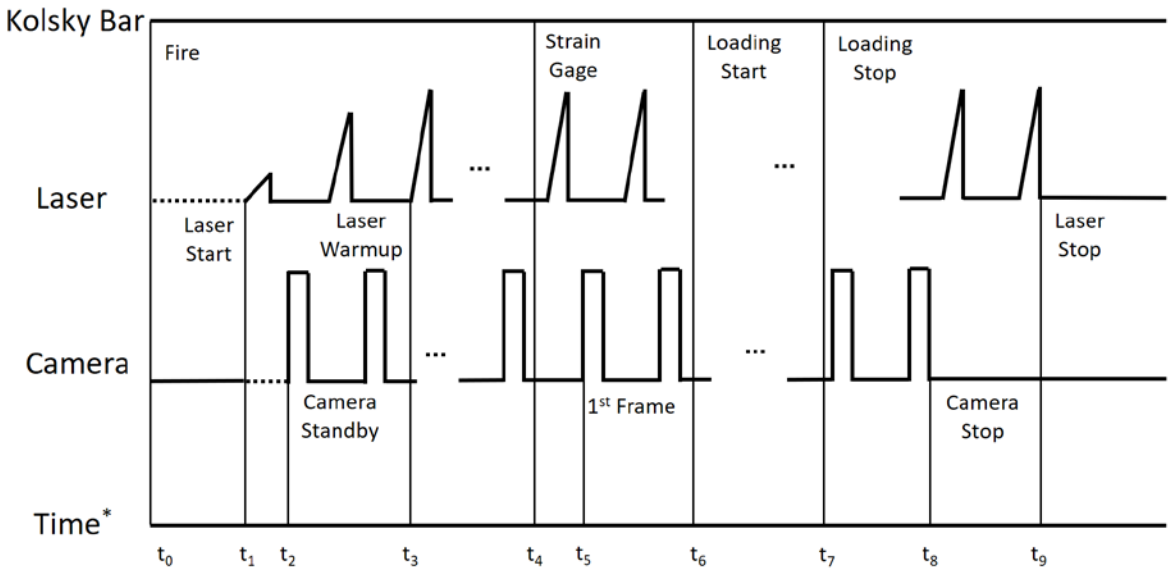

Figure 4.5. The timing sequence of the Kolsky bar experiment with laser phosphorescence. * Timeline is not to scale.

4.1.4 Temperature calibration

A temperature calibration is carried out by first placing one of the aluminum specimens from the loading experiments inside an optically accessible Mellen MV box furnace. The specimen temperature is then monitored with a type K thermocouple as spectral ratio measurements are made

at different oven temperatures. The thermocouple is kept in contact with the specimen surface and oven temperatures are allowed to stabilize before the ratio measurements are conducted. The ratio measurements are normalized by a room temperature measurement case to account for spatial variations in the measured ratio that may be caused by irregularities in the phosphor coating thickness, the laser beam profile, or differential collection efficiency between the two legs of the image doubler. For the calibration and dynamic loading experiments, the camera exposure is begun 100 ns after the start of the laser pulse. A linear curve fit is applied to the oven data to create a calibration curve. The normalized calibration curve, collected at a fluence of 93 μJ/cm^2, is given in Figure 4.6 with error bars representing the average standard deviation on either side of the mean. The average standard deviation in ratio measurements at room temperature is 3%, but increases to as much as 6.7% at higher temperatures.

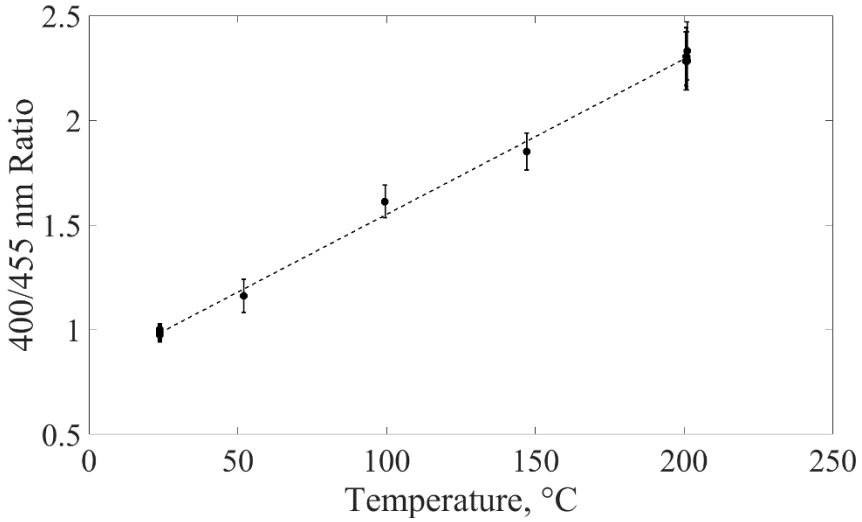

Figure 4.6. Calibration curve acquired at 93 μJ/cm^2 with a 4 μs camera exposure.

In order to further ensure that changes in local laser fluence would have no effect on the measurement, calibration data was also taken at average pulse fluence levels of 42 and 76 μJ/cm^2. Figure 4.7 shows that fluctuations in laser fluence have no appreciable effect on the measured ratios at these fluence levels. The curve fit from Figure 4.6 is reprinted here for comparison.

The experiments were conducted using both 2 and 4 μs camera exposures. In order to ensure that the exposure time did not affect the temperature correlation curve, calibration data are collected using a 2 μs exposure. Figure 4.8 provides both the 2 and 4 μs data, collected with a laser

fluence of 93 μJ/cm^2, as functions of temperature. Again, the curve printed here is fit to only the 4 μs data. The maximum deviation from the 4 μs calibration curve in the 2 μs data is 4.9%, but the curve lies within one standard deviation of the mean for all data points.

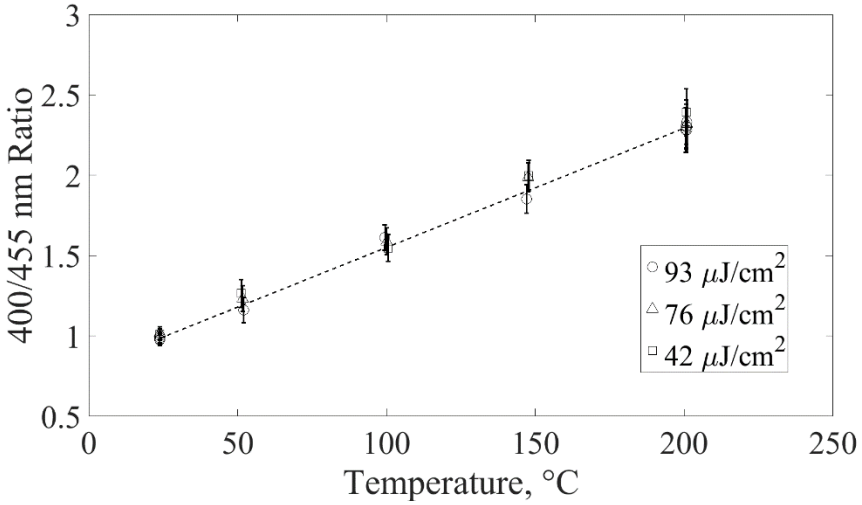

Figure 4.7. Ratio measurements at different average pulse fluence levels.

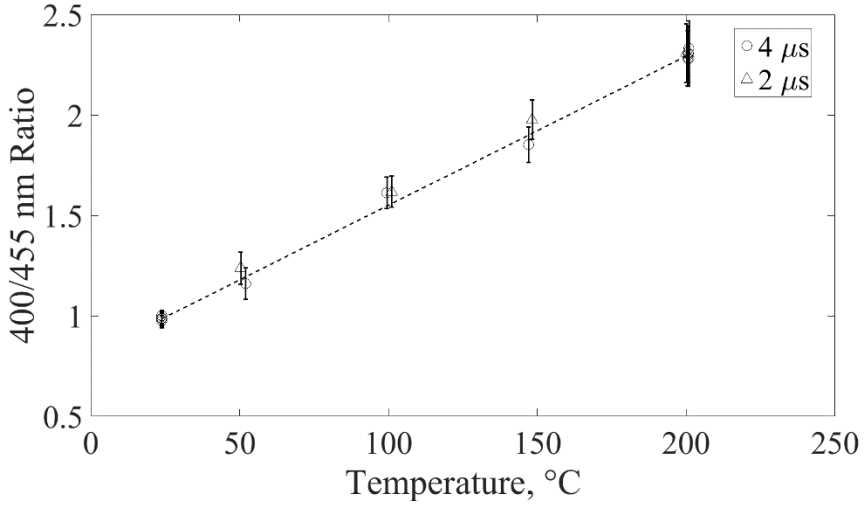

Figure 4.8. Ratio measurements using different camera exposures and constant pulse fluence.

4.1.5 Image processing

Image processing begins with obtaining the image registration matrix, which is performed by using an image registration code to overlay the two halves of the images. The image used for registration purpose is taken with the identical experimental setup but without laser or any filter. An intensity threshold of 50% of the maximum intensity in an image is set in order to eliminate pixels with a low signal-to-noise ratio. A Gaussian smoothing operation with a standard deviation of seven pixels is applied to the images to further eliminate the effects of camera noise. The ratio of the two images is then taken to render a ratio image. Phosphorescence images of the static specimen are captured without any loading applied before each experiment. The ratio images that are captured during dynamic loading are then normalized by the static ratio images to account for the spatial irregularities, discussed in the description of the calibration procedure. Finally, using the calibration curve, each pixel's ratio is converted to a temperature.

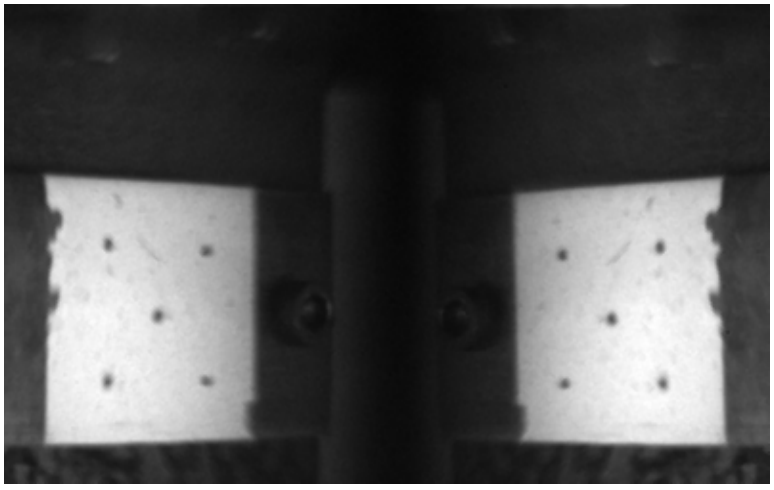

Figure 4.9. A representative image used for image registration.

4.2 Dynamic Compression of Copper

4.2.1 Experimental results

The temperature response of copper under dynamic compression was studied with five specimens. A typical experimental record from the oscilloscope is presented in Figure 4.10. The pulse signals showing in magenta represents the timing of each camera frame. In this experiment, the high-speed camera is operating at 100 kHz and starts to send frame signals when the laser starts. When receiving the trigger signal from the strain gages, the camera records the first frame. The recording stops automatically when 256 images are taken. With this camera frame information, the loading history can be directly correlate to the temperature images frame-to-frame.

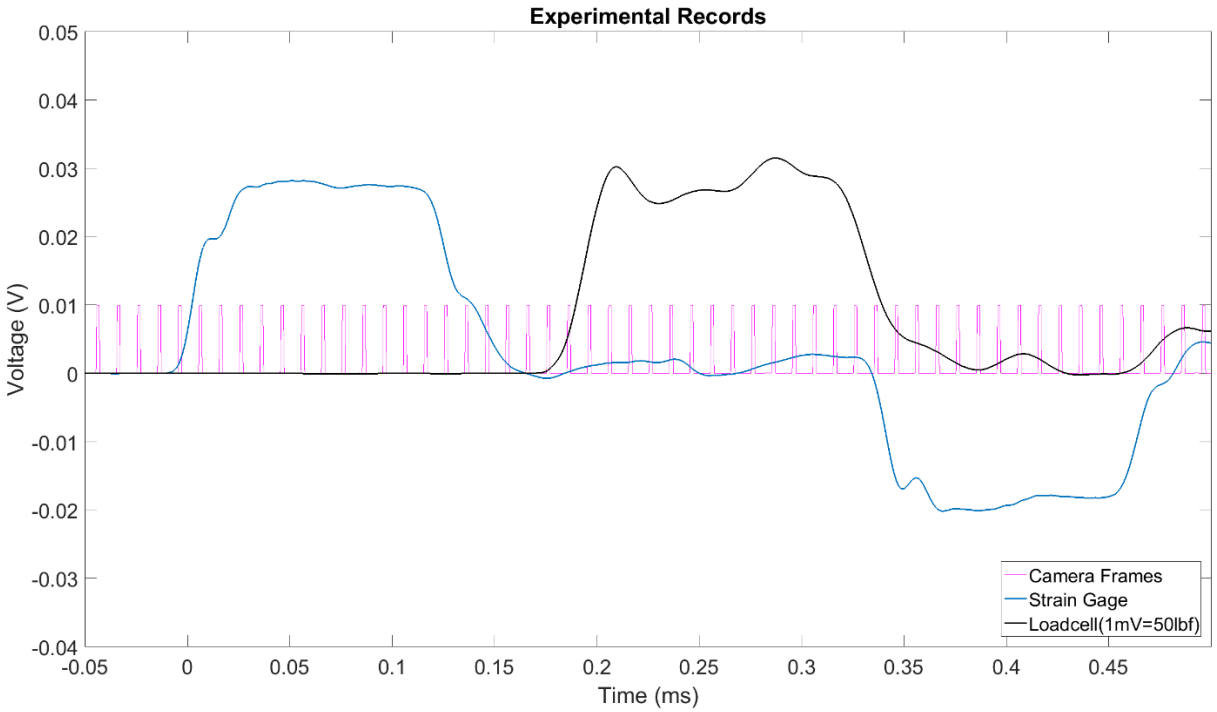

Figure 4.10. A typical experimental record showing strain gage, load cell and camera frame signals.

Figure 4.11 shows the images captured directly from the camera. With the image doubler, the field of view is divided in the middle, showing the specimen in a mirrored view. The brighter

side on the left is the light path with 450 nm filter and the dimmer side on the right corresponding to the light path with 400 nm filter. The curved edge of the specimen is due to the shadow of the fixture on the load cell side. The temperature fields after image processing are shown in Figure 4.12. At t = 0, loading begins and the incident bar starts to move towards right. The material surface temperature is the same as room temperature 300 K. At t = 40 μs, the material is deforming dynamically at 1000 /s strain rate. A slight overall temperature increase among the surface can be measured. Note that the high temperature zone close to the left edge of the specimen is due to the error of boundary effect during the image processing and should be discarded. Referring to Figure 4.13, the loading stops at t = 120 μs. The specimen is observed to undergo plastic deformation from the images. A drum shape can be seen on the top and bottom edges due to the material's Poisson's ratio. The surface temperature continues increasing. There are some phosphor debris falling off from the material surface due to large deformation, resulting in the absence of some pixel values in the temperature field. At t = 200 μs, loading has stopped after the first stress pulse. Phosphor coating can be observed to crack in the center of the material, causing corresponding discontinuity in the temperature field. During the first loading pulse, the temperature was found to increase by less than 5 K. But the temperature continues increasing after the loading stops, which indicating a delay between the measurement and the real temperature of the material surface.

By taking an area average within the boxed area showing in Figure 4.12, the complete temperature history is plotted in Figure 4.14. The loading lasts only for 0.12 ms but the temperature rise can be seen delayed until 0.5 ms, with the peak temperature measured at 312 K. This delay is most likely resulted from the heat conduction from the phosphor-specimen interface to the phosphor surface. Considering that the time scale of these dynamic experiments are 10^0 – 10^1 μs, the heat transfer is not fast enough to reach a steady state.

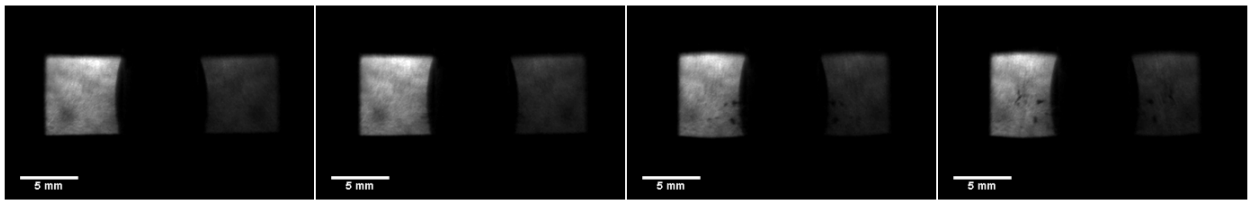

Figure 4.11. A representative sequence of raw images captured from the high-speed camera.

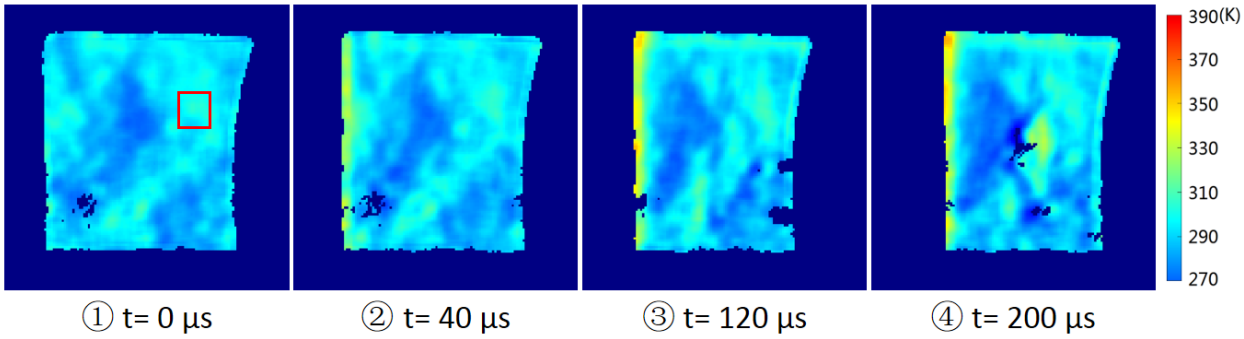

Figure 4.12. A representative image sequence of the temperature field of copper during dynamic compression.

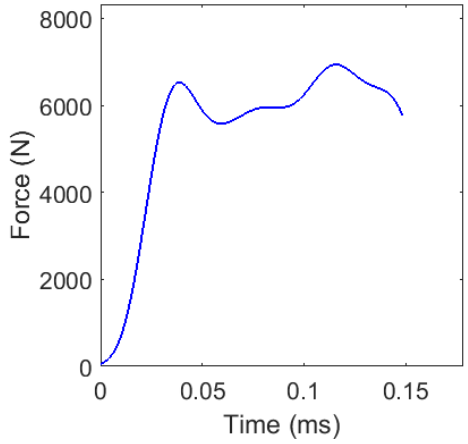

Figure 4.13. A representative force – time relationship of copper during dynamic compression. The time is in accordance with the high-speed images.

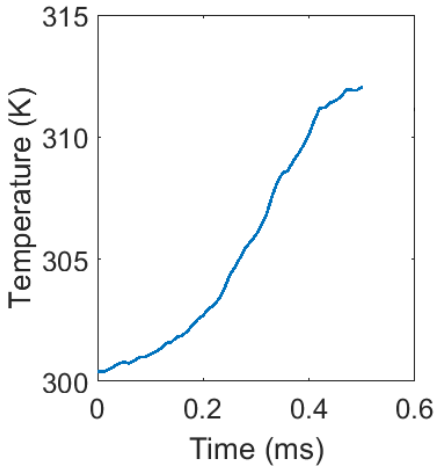

Figure 4.14. The average temperature history inside the boxed area shown in Figure 4.12

4.2.2 Discussion

The copper material shows a uniform surface temperature increase during the dynamic compression. Although the temperature reaches 312 K after the loading, the temperature measured is unsynchronized with the loading history. To further verify the aforementioned temperature results, additional dynamic compression experiments with identical loading condition with a thermocouple attached to the material surface are performed. Before the experiment, a small hole of ⌀0.3×0.5 mm is drilled in the same location as the boxed area shown in Figure 4.12. Then a fast response type-T thermocouple (Omega Engineering Inc., Norwalk, Connecticut) is inserted into the hole to measure the temperature close to the material surface so that a secure contact between the thermocouple and the material can be ensured. The diameter of the thermocouple wire used in this chapter is 0.076 mm and the temperature of the thermocouple reference junction is 296 K.

The temperature history of the thermocouple is presented in Figure 4.15. The temperature starts to increase shortly after the loading starts when a tight contact is established between the thermocouple and the specimen. The maximum temperature is measured as 317 K at 0.12 ms, which is very similar to the temperature peak of 312 K shown in Figure 4.14. The timing of the temperature rise is also in good agreement with the timing of the force history displayed in Figure 4.13. The thermocouple experiments were repeated four times and all results are consistent. Therefore the temperature measurement using the laser phosphorescence is valid despite the temporal delay.

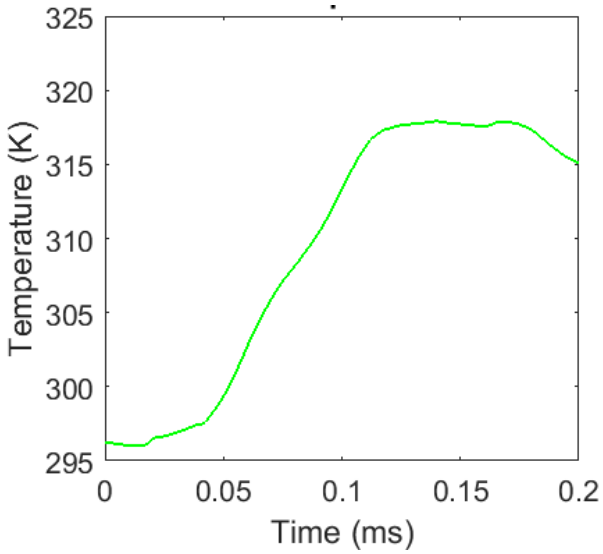

Figure 4.15. Temperature – time history of the thermocouple attached to the copper during a dynamic compression experiment.

4.3 Dynamic Shear of Aluminum Alloys

4.3.1 Experimental results

The temperature field evolution during shear banding is studied in this chapter using laser phosphorescence with aluminum alloy 7075-T6 and 6061-T6, respectively. The raw images of 7075-T6 taken from the high-speed camera are presented in Figure 4.16 and the thermal images after processing are shown with the corresponding force history in Figure 4.17. When the loading starts at t = 0, there is no temperature rise in the first 15 μs. Then there is a local hot spot forming close to the left edge. Simultaneously, the area near the right edge also shows slight temperature rise. There are some absent pixels in the images shown due to the local saturation of the pixel values, which is further caused by the fluctuation of the laser intensity. At t = 35 μs, the temperature reaches its peak of 313K at the location indicated by the square box. A shear band has formed and propagates towards the right edge along the gage section. Meanwhile the force reaches the maximum as well. At t = 40 μs, the high temperature zone is connected into a line. At t = 45 μs, some phosphor in the shear zone fall off from the specimen surface due to the large shear deformation (Figure 4.16). It is in accordance with the thermal image that the high temperature

zone can be seed separated with material fracture already happen. It can be found there is clearly a temporal delay in the temperature response, as there is no temperature increase until the t = 15 μs. The abnormally low temperature can also be resulted from this delay, which is possibly caused by the heat conduction from the phosphor-specimen interface to the phosphor surface.

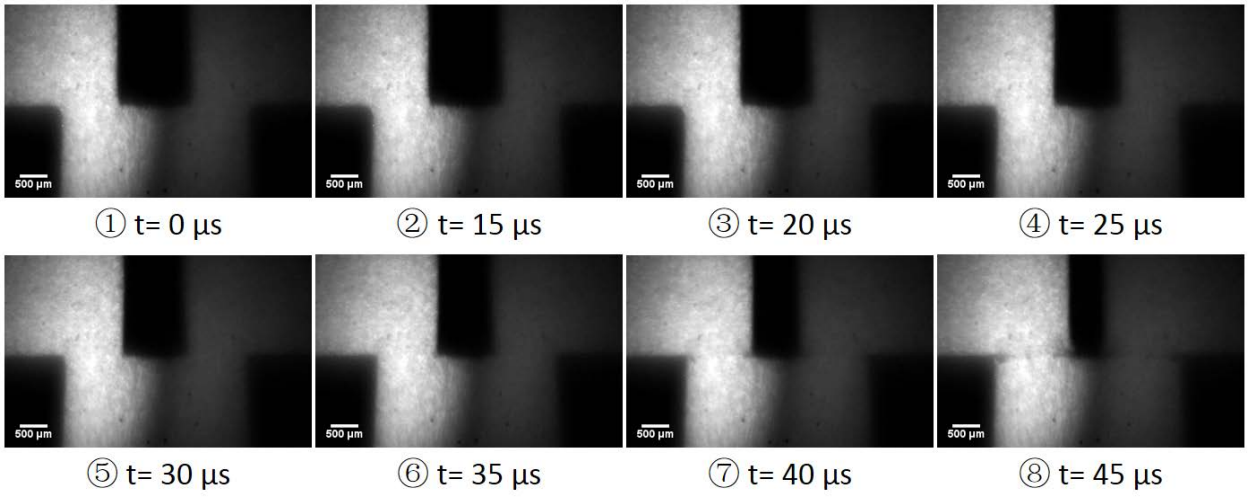

Figure 4.16. A representative sequence of raw images showing material deformation and phosphorescence of 7075-T6

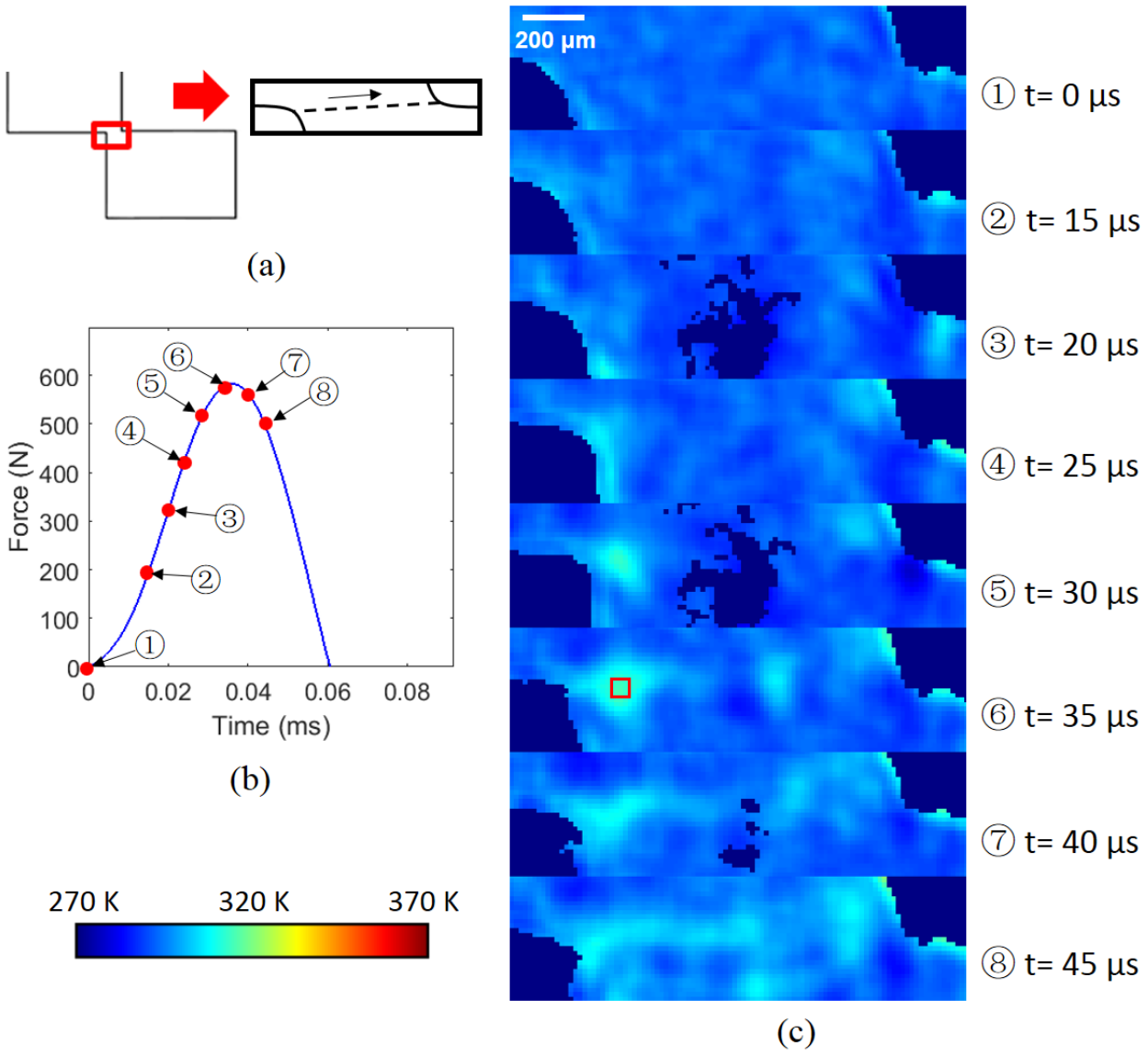

Figure 4.17. A representative force-time relationship and the corresponding thermal image sequences of aluminum 7075-T6. (a) The location of the camera window. (b) The force-time graph. (c) The thermal image sequence showing the temperature field evolution.

The temperature field evolution of 6061-T6 is similar to 7075-T6. Figure 4.18 shows the raw images of phosphorescence and the processed thermal images are shown with the corresponding force history in Figure 4.19. The shear loading starts at t = 0. But temperature response is delayed for three frames after the loading starts, which is at t = 15 μs. At t = 20 μs, hot spots can be observed forming near both left and right edges. The temperature at these two locations continues to increase (t = 25 – 35 μs) and the one on the right reaches the maximum of

321 K at t = 45 µs. The hot spot is enlarging and heat is dissipating to the adjacent areas. According to Figure 4.18, a crack can be observed having propagated along the gage section at t = 45 µs and the material is separated after this moment. The force is also at its maximum of 590 N. The material fracture leads to the breakage of the phosphor coating. Therefore the temperature within the shear zone is not measurable afterwards. Same as the 7075 results, the thermal response of 6061 also exhibits a delay of ~15 µs.

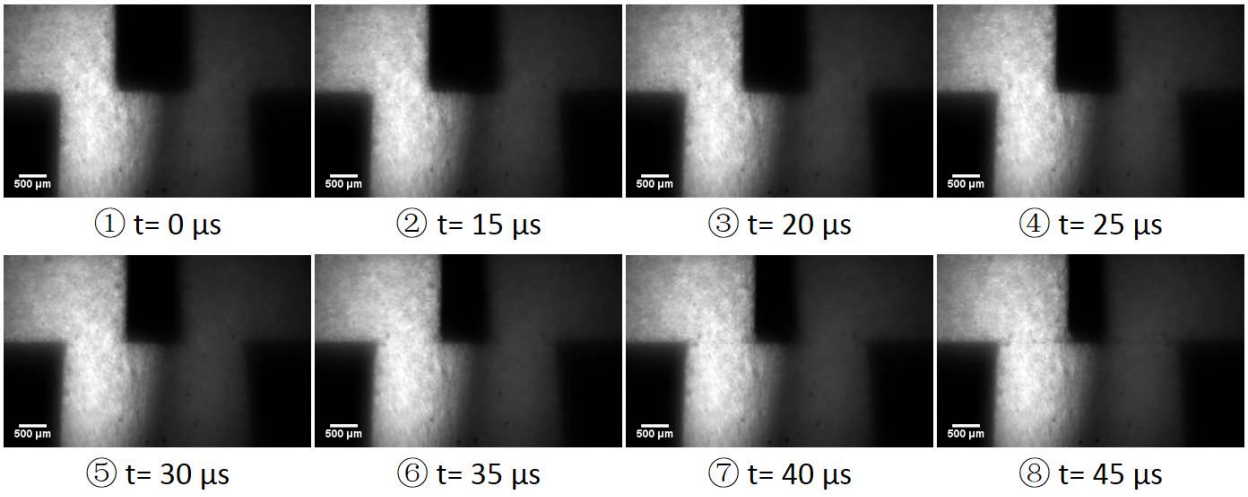

Figure 4.18. A representative sequence of raw images showing material deformation and phosphorescence of 6061-T6

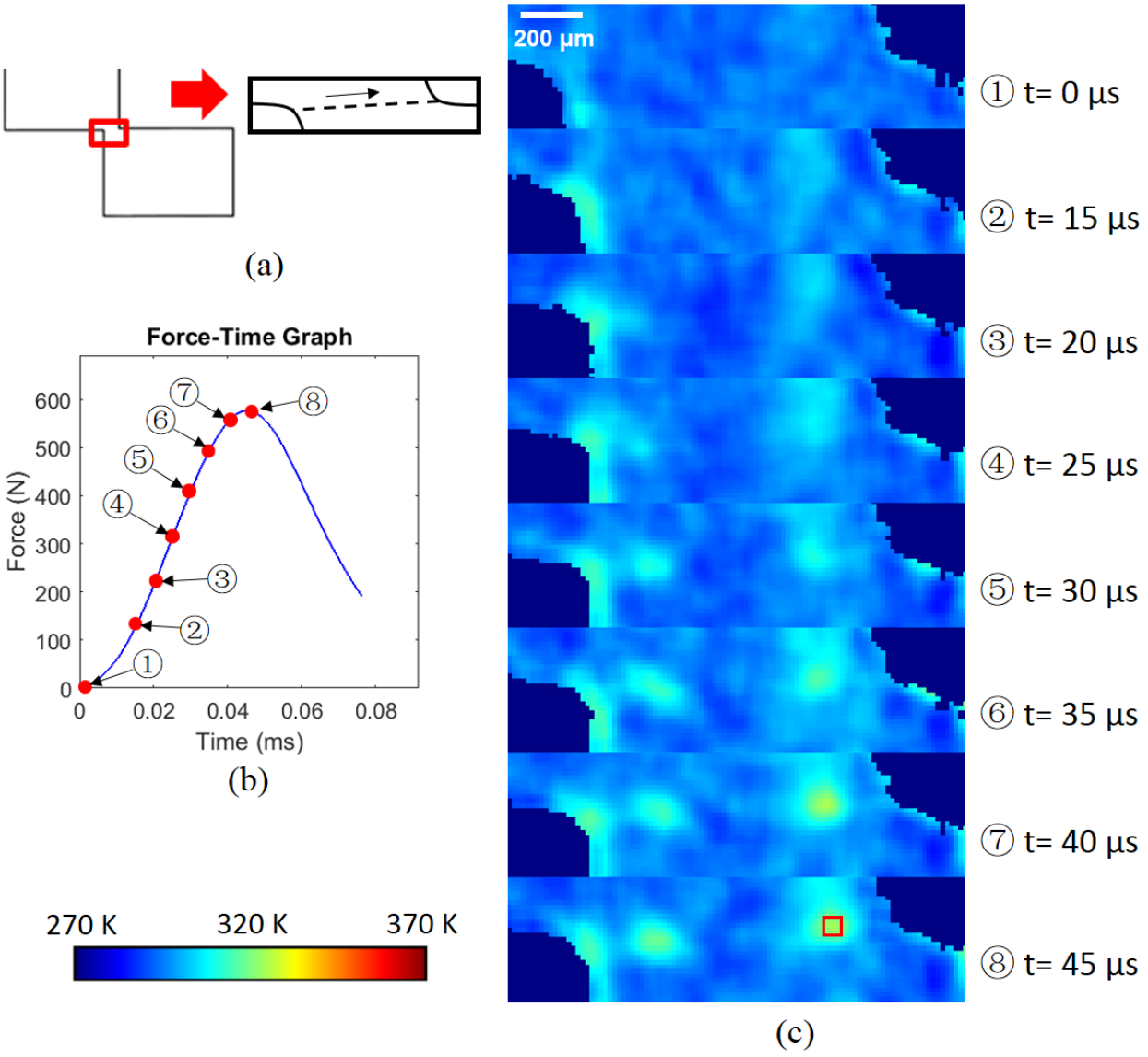

Figure 4.19. A representative force-time relationship and the corresponding thermal image sequences of aluminum 6061-T6. (a) The location of the camera window. (b) The force-time graph. (c) The thermal image sequence showing the temperature field evolution.

4.3.2 Discussion

The results of the temperature evolution during shear band formation in aluminum 7075-T6 and 6061-T6 show very similar trend of a the results in Chapter 2.2. However, the temperature measured is much lower in this group of experiments, which is not likely to be the real temperature

in the specimen. Unlike the results of copper compression in which the phosphors stay on the material after the first loading pulse, the aluminum specimens fail during the first pulse. Due to the fracture and absence of the phosphor coating within the shear banding area, there is not sufficient time for the temperature to reach the specimen surface temperature. Knowing that transient thermal conduction is the major cause to this issue, it is beneficial to have temperature correction for these cases, which can be achieved by having a transient heat transfer study.

Considering a one-dimentional condition that the heat is transferring from the interface between the specimen and the phosphor through the thickness of the phosphor coating to the outside surface. The entire transient thermal conduction in the aforementioned experiments can be divided into three stages, as illustrated in Figure 4.20. In the first stage, the temperature starts to rise in the specimen but the heat has not yet transferred to the outside surface of the phosphor, so there is no temperature change on the phosphor surface. The duration of this stage equals to the delay time discussed in the previous chapter, which can be obtained by comparing the start points of the force – time curve and the temperature image, then taking the time difference between them. The delay time t is found as 15 μs for aluminum shear experiments and 20 μs for copper compression. In the second stage, the temperature continues to increase in the back of the phosphor and starts to show up on the outside surface as well. However, the increase rate outside the phosphor is relatively slow due to the nature of the thermal conduction. Stage 2 ends when the temperature in the specimen reaches the maximum, where the third stage follows. While no more heat is generating in the specimen material, the outside temperature continues to increase until it reaches a steady state, in which the temperature is the same as inside. Apparently, stage 2 is where the temperature correction is focused on.

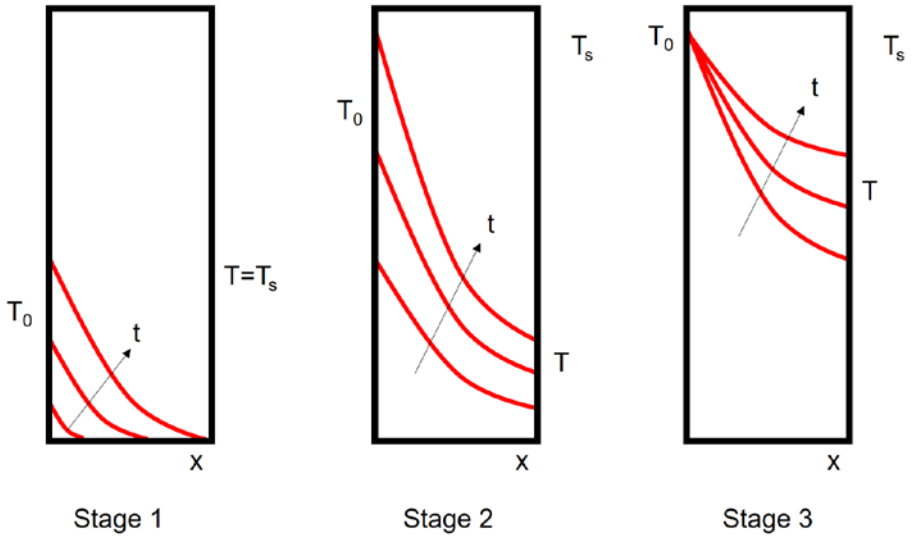

Figure 4.20. The three stages of transient thermal conduction with an increasing T_0.

The simplified equation for 1-D heat transfer is given as

$$\alpha \frac{\partial^2 T}{\partial x^2} = \frac{\partial T}{\partial t} \tag{4.1}$$

where T is the temperature and α is the thermal diffusivity of the material. For the $BaMgAl_{10}O_{17}:Eu^{2+}$ phosphor powder, there is no existing information on the thermal diffusivity or conductivity. Since the material mainly consists of Al_2O_3, the diffusivity is estimated to be the same as Al_2O_3, which is calculated as 4.3×10^{-7} m^2/s [67]. To simulate the stage 2 of the aforementioned transient thermal conduction, the boundary condition is taken as semi-infinite long solid with elevated temperature inside the phosphor coating. The heat equation has the following solution:

$$T = T_s + (T_0 - T_s)\left(1 - \frac{2}{\sqrt{\pi}} \int_0^{\frac{x}{2\sqrt{\alpha t}}} e^{-u^2} du\right) \tag{4.2}$$

where T_0 is the temperature inside the phosphor coating, T_s is the room temperature and T is the temperature at given location x and time t. If x is the thickness of the phosphor coating and t is the delay time in the previous paragraph, then T becomes the temperature on the outside surface of the

phosphor coating, which is known from the thermal images. Then this solution can be used to solve for the unknown T_0, given the known thermal conduction length x and time t:

$$T_0 = T_s + \frac{T - T_s}{1 - \frac{2}{\sqrt{\pi}} \int_0^{\frac{x}{2\sqrt{\alpha t}}} e^{-u^2} du} \tag{4.3}$$

The thermal conduction length in this case is the thickness of the phosphor coating layer. The scanning electron microscopic (SEM) image (Figure 4.21) shows the cross-sectional area of the specimen with a uniformly coated phosphor layer, which is measured as 7 μm in thickness.

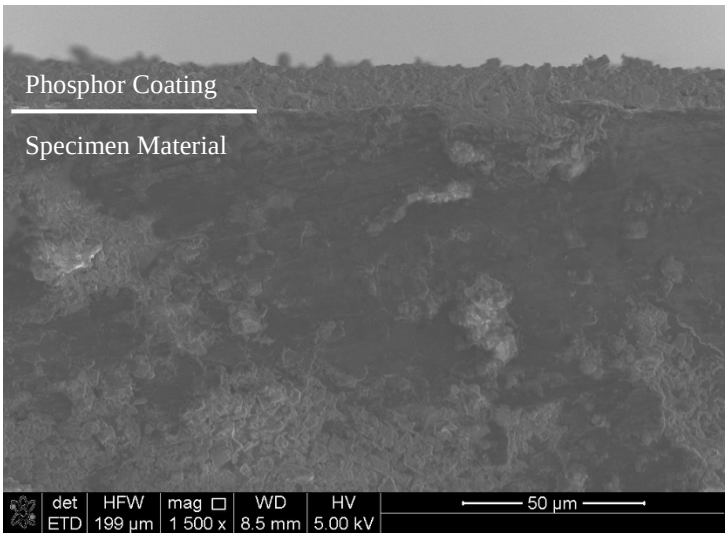

Figure 4.21. A scanning electron microscopic image showing the phosphor coating on an aluminum specimen

Based on Equation (4.3), the corrected temperature for the specimen at designated locations can be calculated. Figure 4.22 compares the original measured temperature and the corrected temperature for 7075-T6, with (a) showing the average temperature history within the boxed area from Figure 4.17(c) and (b) showing the corrected temperature on the aluminum surface. The small region consists of 16 pixels and represents one of the hot spots on the surface. After the correction, the delay issue is eliminated and the temperature reaches its peak at approximately the same time as the force is the maximum, as presented in Figure 4.17(b). This indicates that the temperature increase is resulted from the material deformation. When the material fails, heat dissipation

dominates and no more heat is generated. The maximum temperature is found at around 650 K. Similarly, the temperature curves for 6061-T6 before and after correction are plotted in Figure 4.23 with area of interest specified in Figure 4.19(c). This temperature history is also in good accordance with the force-time graph shown in Figure 4.19(b) with its peak at approximately 800 K.

Note that this temperature correction method can also be applied to the copper compression results by taking the corresponding room temperature, delay time and phosphor thickness into Equation (4.3). However, according to Figures 4.13 and 4.14, the loading is finished at 0.15 ms while the surface temperature increases by less than 2 K. Considering that the measuring error from the system is in the same order, the error will be significantly magnified and bring large uncertainty to the final results.

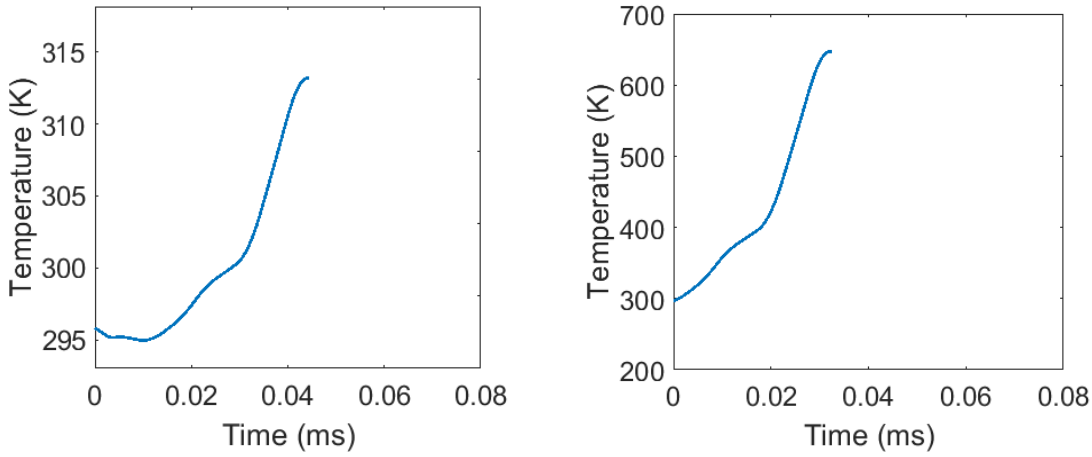

Figure 4.22. The average temperature – time history of aluminum 7075-T6 in the boxed area shown in Figure 4.17 (a) before the temperature correction. (b) after the temperature correction.

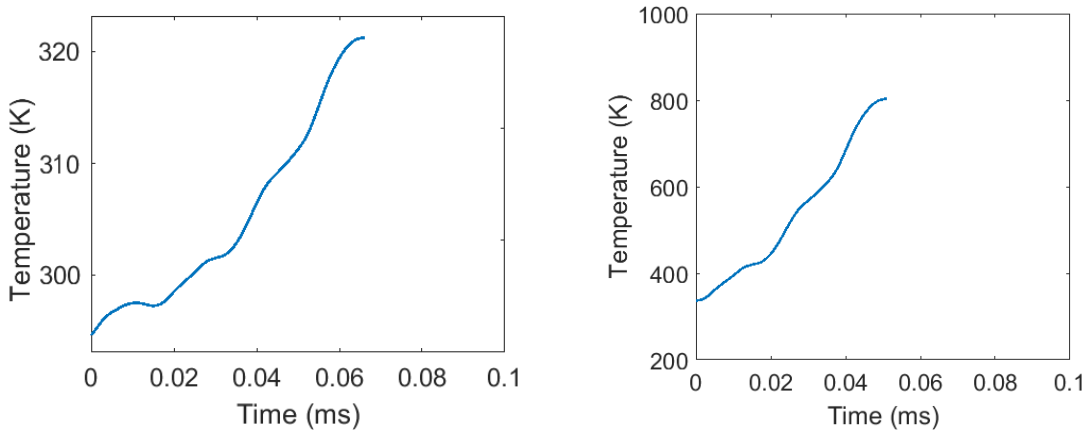

(a) (b)

Figure 4.23. The average temperature – time history of aluminum 6061-T6 in the boxed area shown in Figure 4.19 (a) before the temperature correction. (b) after the temperature correction.

Both aluminum 7075 and 6061 show very high temperature during the dynamic shear band formation. The maximum surface temperature of 650 K for 7075 and 800 K for 6061 is close to the melting points of the corresponding aluminums, which are 750 K and 850 K, respectively. These temperature results are also in good agreement with the infrared results and with improved spatial and temporal resolution. For both aluminums, the ASB formation starts before the force reaches its maximum value, according to Figures 2.7 and 2.10. Solely from the previous infrared images, high temperature is only observed after the shear band forms due to the limited number of images taken. With the laser thermometry, the temperature field evolution during the loading can be better revealed. The temperature increases with the load, and maintains increasing after the formation of ASB until the fracture of the material. By comparing the X-ray PCI images with Figures 4.22(b) and 4.23(b), it can be found the ASB forms at the temperature of approximately 400 K for 7075-T6 and 440 K for 6061-T6. Traditionally the ASB formation is generally accepted as a result of thermal softening, which means the high temperature is the cause of ASB formation. But there are also research findings showing opposite thermal behaviors that the development of the ASB further induces the rise of the temperature [23]. In this study, the temperature is shown to increase before the ASB forms. Therefore the rise of the temperature is not completely a consequence of the ASB formation, but rather a result throughout the entire plastic deformation. Since the temperature when the ASB forms is much lower than the maximum temperature, it is

reasonable that the thermal softening is not the dominant reason for the formation of the ASB. As mentioned in [68], the voids and defects in the material can play an important role in these experiments.

4.4 Summary

In this study, the high-speed laser phosphorescence thermal imaging technique is developed and integrated with the compression Kolsky bar setup. The temperature field measurement during dynamic loading of materials are performed at 100 – 200 kHz frame rate with a spatial resolution of 13 μm/pixel. In the dynamic compression of copper at a strain rate of 1000 /s, the material shows an overall temperature increase on the surface during the deformation. The maximum temperature is found at 312 K. The thermocouple results confirm the measurement of the laser phosphorescence. The results also reveal the thermal conduction issue caused by the phosphor coating, which leads to a delay in the temperature response. In the dynamic shear banding of aluminum alloys, multiple local high temperature spots are observed in both 7075-T6 and 6061-T6. A temperature correction method is proposed to estimate the real temperature on the specimen surface under the phosphor coating. After the correction, the results are in good agreement with the infrared measurements discussed in Chapter 2 despite of the experimental error. However, the temporal and spatial resolution are both improved so that more detailed information on the ASB formation is revealed. The ASB formation is found after the temperature starts to increase, but still at a relatively low temperature of 400 K and 440 K for 7075-T6 and 6061-T6, respectively. Therefore thermal softening is not considered as the main cause of the ASB formation due to this fact. Finally, the maximum temperature is measured as 650 K for 7075-T6 and 800 K for 6061-T6.

5. FUTURE WORKS

The current work on the laser phosphorescence is successful in measuring the temperature field evolution during dynamic compression of copper and the ASB formation in aluminum alloys at 100 – 200 kHz frame rate by using the intensity ratio method. However, the measured temperature behaviors exhibit temporal delay, which is mainly due to the thermal conduction through the phosphor coating material. Although a temperature correction is proposed to estimate the real temperature behind the phosphor, it inevitably increases the uncertainty of the results. If the phosphor coating can be reduced to 10^1 – 10^2 nm scale without sacrificing the emission intensity, the overall temperature response will be remarkably improved. Currently the BAM:Eu phosphor used are commercial available products with mean diameter at 2.4 μm [69]. Figure 5.1 shows the shapes and sizes of the phosphor particles used in this work, which in consistency with the reported values. Apparently, it is not realistic to have a sub-micron scale uniform coating layer of the phosphor with this product, as the particle size effect will become significant when thickness is further reduced below 7 μm.

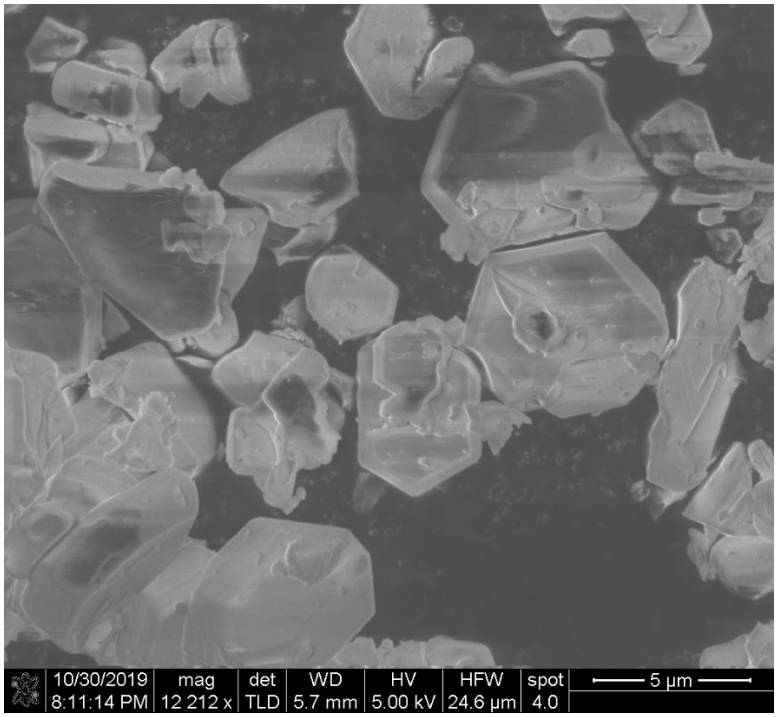

Figure 5.1. A microscopic image showing the size distribution of BAM:Eu phosphor particles.

Recently, Sharma et al. [70] developed a nano-sized BAM: Eu^{2+} phosphor with particle size at 15 – 40 nm using Sol–Gel method. The synthesis process is demonstrated in Figure 5.2. In a typical synthesis process, the metal nitrates (Ba^{2+}:0.09 M, Al^{3+}:1.0 M, Mg^{2+}:0.1 M) are first dissolved in distilled water. Europium doping concentration is controlled as 5% of the Ba^{2+} ion concentration. Citric acid with equal weight of all metal precursors are then added for chelation with a proper amount of ethylene glycol for gel formation. The solution needs to be continuously stirred and heated at 100 °C while it is clear solution. After the vaporization of the excess water, the mixture was heated at 300 °C for 1.5 hours, leaving phosphor gels in white color. The fine-sized powders are collected by grinding the gel. Finally, the phosphor powders are annealed at temperatures from 400 – 1200 °C for 4 hours in reducing atmosphere. The TEM image of this BAM:Eu phosphor shows the particle shape is uniform and the size is approximately 10 – 40 nm (Figure 5.3).

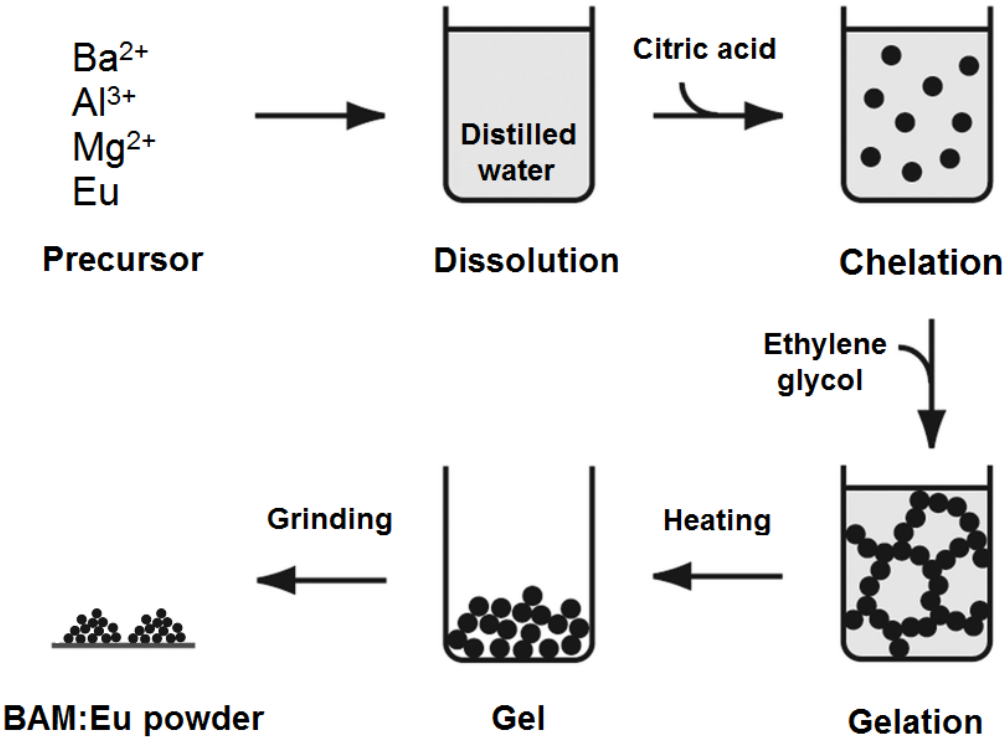

Figure 5.2. Synthesis process of nano-sized BAM:Eu phosphor.

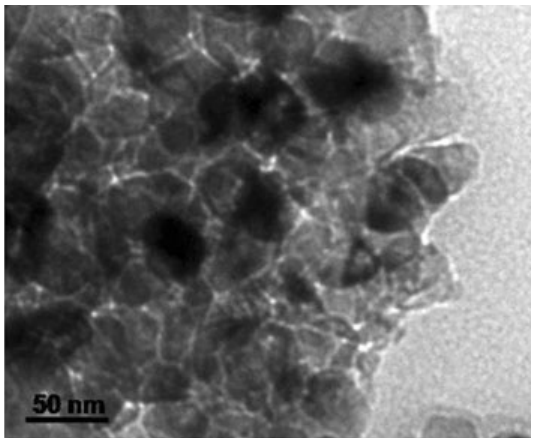

Figure 5.3. A TEM image and morphology of the BAM:Eu annealed at 1200 °C [70].

With the nano-sized phosphor powder, it is possible to obtain a thinner coating layer. The heat conduction through this phosphor layer can then be calculated with Equation (4.1) under the same 1-D simplification and boundary conditions illustrated in Figure 4.20. If the temperature at the interface of the phosphor and the specimen T_0 is given, the temperature to be measured on the outside surface of the phosphor T can be calculated using Equation (4.2). A temperature-time graph is presented in Figure 5.4 to compare the effect of the coating thickness d, assuming T_0 = 700 K at t= 0 and room temperature T_s = 300 K. Note that the curve of d = 7 μm is the experimental condition discussed in Chapter 4. It is clear that reducing thickness will significantly reduce the delay caused by heat conduction. A detailed view of the temperature-time curves are presented in Figure 5.5. With a coating thickness of 200 nm, the temperature difference between the phosphor surface and the specimen surface at t = 0.005 ms is 20 K, which is equal to 5% of the temperature rise from T_s to T_0. If repeating the aluminum shear banding experiment in Chapter 4.3, then this temporal delay will be equivalent to only one frame at 200 kHz frame rate. If further reducing the coating thickness to 20 nm, the temperature rise will be even faster and the difference can be observed negligible even at t = 0.001 ms, meaning that performing temperature measurement at 1 MHz or higher is theoretically feasible.

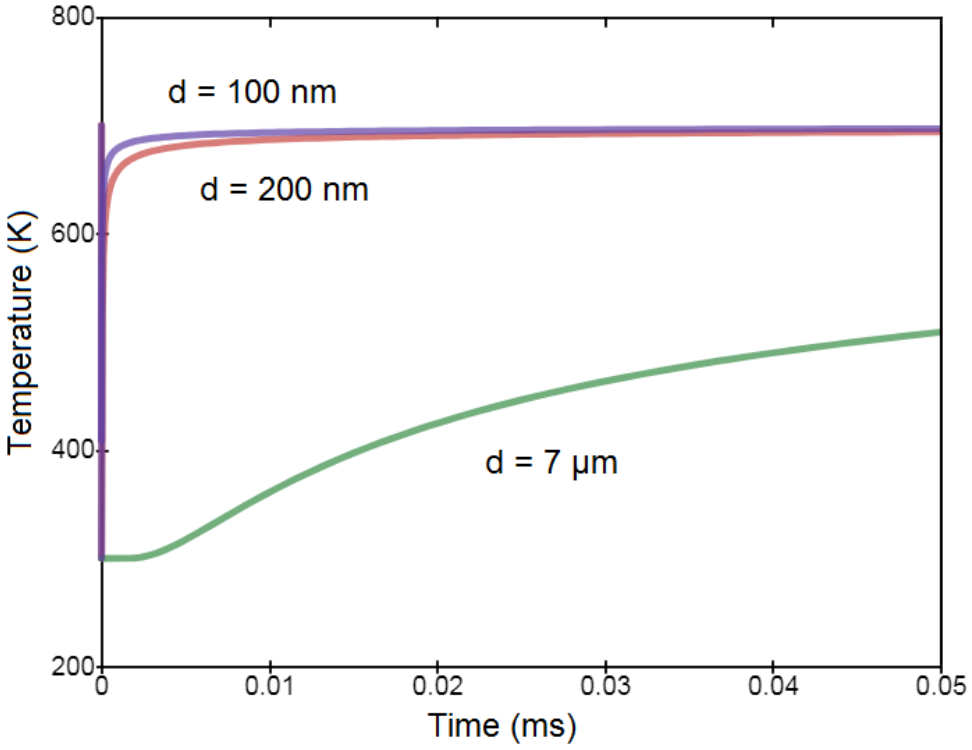

Figure 5.4. Temperature rise vs time at outside surface of the phosphor with different coating thickness, given T_0 = 700 K at t = 0 and room temperature T_s = 300 K.

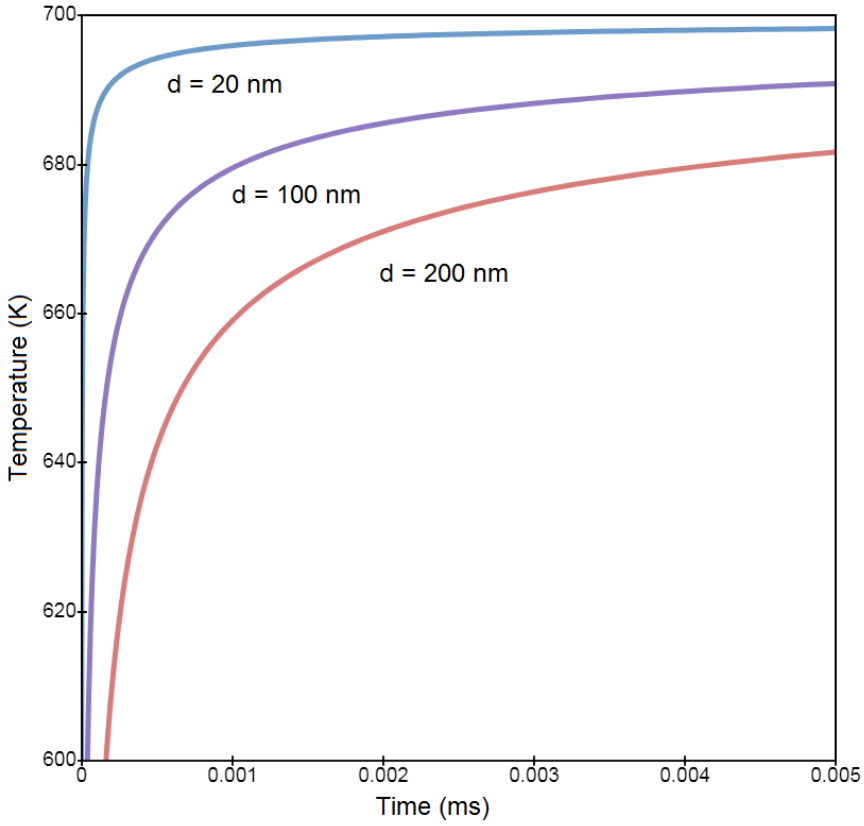

Figure 5.5. A detailed view of the Temperature rise vs time at outside surface of the phosphor with different coating thickness, given T_0 = 700 K at t = 0 and room temperature T_s = 300 K.

After overcoming the temporal delay of the temperature measurement, there are still other issues to be addressed to improve the temperature recording speed. The current high-speed imaging technology is capable to realize MHz or higher frame rate measurement, which should not be a limitation to this high-speed laser phosphorescence technique in the near future. However, the laser energy will need to be significantly increased if operating at high pulse rate, because the exposure of each frame has to be reduced. With a shorter time between frames, the lifetime of the phosphor material will play an increasingly important role in the emission profile as the phosphor can be excited before the previous phosphorescence mostly decays. Therefore a systematic calibration on the relationship of phosphorescence intensity and the higher laser fluence is necessary. It is also beneficial to explore the other potential phosphor materials that features both shorter lifetime and proper sensitive range of temperature.

6. CONCLUSION

In this dissertation, the deformation and temperature field evolution of dynamic shear band formation in aluminum alloys and the temperature field of copper under dynamic compression were investigated. A Kolsky bar setup was synchronized with X-ray PCI in Argonne National Laboratory to observe the ASB formation of aluminum 7075-T6 and 6061-T6 in real time. A high-speed camera with 20× lens was used to capture images during dynamic loading at 5 MHz. A flat hat-shaped specimen geometry was adopted with an impact speed of ~16 m/s. Both materials exhibited the trend of uniform shear deformation, formation of shear bands, cracking and then shear failure. 6061-T6 was found to be more ductile and formed ASB at larger strain. The temperature fields were measured using a high-speed infrared thermal camera at 64 kHz. The maximum temperature was found to be 720 K for 7075-T6 and 770 K for 6061-T6. This heat accumulation and the corresponding thermal instability during dynamic loading were found to be closely related to the formation of the ASB. The shear band width is estimated as 20 – 50 μm for 7075-T6 and 30 – 70 μm for 6061-T6. The cracks initiate after shear bands form and propagate in the same tracks as the shear bands at approximately 1100 m/s.

To further break the barrier of high-speed temperature field measurement, a high-speed laser phosphorescence thermal imaging technique was developed and integrated with the compression Kolsky bar setup. The temperature field measurement during dynamic loading of materials were performed at 100 – 200 kHz frame rate with a spatial resolution of 13 μm/pixel. $BaMgAl_{10}O_{17}:Eu^{2+}$ thermographic phosphor material was chosen due to its wide sensitive range and unique emission spectral suitable for the intensity ratio method. In the dynamic compression of copper at a strain rate of 1000 /s, the material showed an overall temperature increase on the surface during the deformation. The maximum temperature was found at 312 K. The thermocouple results confirmed the maximum temperature measured by the phosphor thermometry. The results also raised the thermal conduction issue caused by the phosphor coating, which led to a delay in the temperature response. In the dynamic shear banding of aluminum alloys, multiple local high temperature spots were observed in both 7075-T6 and 6061-T6. A temperature correction method was then proposed to estimate the real temperature on the specimen surface under the phosphor coating. After the correction, the maximum temperature was found as 650 K for 7075 and 800 K for 6061, which

agreed with the infrared measurements discussed in Chapter 2 despite of the experimental error. Furthermore, the temporal and spatial resolution were both improved so that more detailed information on the ASB formation was revealed. The ASB formation was found shortly after the temperature started to increase, at 400 K and 440 K for 7075 and 6061, respectively. The low temperature indicated that thermal softening was not the major cause of the ASB formation due to this fact. The voids and defects in the materials could assist the shear localization and the ASB formation.

REFERENCES

[1] Zener, C. and Hollomon, J. H., “Effect of strain rate upon plastic flow of steel,” *J. Appl. Phys.*, vol. 15, no. 1, pp. 22–32, 1944.

[2] Li, D. H., Yang, Y., Xu, T., Zheng, H. G., Zhu, Q. S., and Zhang, Q. M., “Observation of the microstructure in the adiabatic shear band of 7075 aluminum alloy,” *Mater. Sci. Eng. A*, vol. 527, no. 15, pp. 3529–3535, Jun. 2010.

[3] Dormeval, R. and Stelly, M., “Study of adiabatic shear bands by means of dynamic compressive tests,” in *International high energy rate fabrication conference*, 1981.

[4] Li, J. C., Chen, X. W., and Huang, F. L., “FEM analysis on the ‘self-sharpening’ behavior of tungsten-fiber/metallic glass matrix composite long rod,” *Int. J. Impact Eng.*, vol. 86, pp. 67–83, 2015.

[5] Timothy, S. P., “The structure of adiabatic shear bands in metals: A critical review,” *Acta Metall.*, vol. 35, no. 2, pp. 301–306, Feb. 1987.

[6] Xu, Y., Zhang, J., Bai, Y., and Meyers, M. A., “Shear localization in dynamic deformation: Microstructural evolution,” *Metall. Mater. Trans. A Phys. Metall. Mater. Sci.*, vol. 39 A, no. 4, pp. 811–843, Apr. 2008.

[7] Dodd, B. and Bai, Y., *Adiabatic shear localization: frontiers and advances*. Elsevier, 2012.

[8] Marchand, A. and Duffy, J., “An experimental study of the formation process of adiabatic shear bands in a structural steel,” *J. Mech. Phys. Solids*, vol. 36, no. 3, pp. 251–283, 1988.

[9] Luz, F. S. da, Junior, L., Pereira, E., Louro, L. H. L., and Monteiro, S. N., “Ballistic test of multilayered armor with intermediate epoxy composite reinforced with jute fabric,” *Mater. Res.*, vol. 18, pp. 170–177, 2015.

[10] Leech, P. W., “Observations of adiabatic shear band formation in 7039 aluminum alloy,” *Metall. Trans. A*, vol. 16, no. 10, pp. 1900–1903, 1985.

[11] Owolabi, G. M., Odeshi, A. G., Singh, M. N. K., and Bassim, M. N., “Dynamic shear band formation in Aluminum 6061-T6 and Aluminum 6061-T6/Al2O3 composites,” *Mater. Sci. Eng. A*, vol. 457, no. 1–2, pp. 114–119, May 2007.

[12] Rosakis, A. J., Mason, J. J., and Ravichandran, G., “The conversion of plastic work to heat around a dynamically propagating crack in metals,” *J. Mech. Behav. Mater.*, vol. 4, no. 4, pp. 375–386, 1993.

[13] Mason, J. J., Rosakis, A. J., and Ravichandran, G., “On the strain and strain rate dependence of the fraction of plastic work converted to heat: an experimental study using high speed infrared detectors and the Kolsky bar,” *Mech. Mater.*, vol. 17, pp. 135–145, 1994.

[14] Zhang, T., Guo, Z.-R., Fu, ·, Yuan, P., Zhang, · Hu-Sheng, and Zhang, H.-S., “Investigation on the plastic work-heat conversion coefficient of 7075-T651 aluminum alloy during an impact process based on infrared temperature measurement technology,” *Acta Mech. Sin.*, vol. 34, no. 2, pp. 327–333, 2018.

[15] Liu, Y. G., Tang, Z. P., and Cui, S. T., “Real-time measuring methods for transient temperature under shock loading,” *Explos. Shock Waves*, vol. 34, no. 4, pp. 471–475, 2014.

[16] Taylor, G. I. and Quinney, H., “The Latent Energy Remaining in a Metal after Cold Working,” *Proc. R. Soc. A Math. Phys. Eng. Sci.*, vol. 143, no. 849, pp. 307–326, Jan. 1934.

[17] Bever, M. B., Holt, D. L., and Titchener, A. L., “The stored energy of cold work,” *Prog. Mater. Sci.*, vol. 17, pp. 5–177, Jan. 1973.

[18] Hartley, K. A., Duffy, J., and Hawley, R. H., “Measurement of the temperature profile during shear band formation in steels deforming at high strain rates,” *J. Mech. Phys. Solids*, vol. 35, no. 3, pp. 283–301, 1987.

[19] Duffy, J. and Chi, Y. C., “On the measurement of local strain and temperature during the formation of adiabatic shear bands,” *Mater. Sci. Eng. A*, vol. 157, no. 2, pp. 195–210, Oct. 1992.

[20] Zhou, M., Rosakis, A. J., and Ravichandran, G., “Dynamically propagating shear bands in impact-loaded prenotched plates—I. Experimental investigations of temperature signatures and propagation speed,” *J. Mech. Phys. Solids*, vol. 44, no. 6, pp. 981–1006, Jun. 1996.

[21] Mercier, S. and Molinari, A., “Steady-State shear band propagation under dynamic conditions,” *J. Mech. Phys. Solids*, vol. 46, no. 8, pp. 1463–1495, Aug. 1998.

[22] Guduru, P. ., Rosakis, A. ., and Ravichandran, G., “Dynamic shear bands: an investigation using high speed optical and infrared diagnostics,” *Mech. Mater.*, vol. 33, no. 7, pp. 371–402, Jul. 2001.

[23] Guo, Y., Ruan, Q., Zhu, S., Wei, Q., Chen, H., Lu, J., Hu, B., Wu, X., Li, Y., and Fang, D., "Temperature Rise Associated with Adiabatic Shear Band: Causality Clarified," *Phys. Rev. Lett.*, vol. 122, no. 1, Jan. 2019.

[24] OMEGA, "The Temperature Handbook."

[25] Farahmand, K. and Kaufman, J. W., "Experimental measurement of fine thermocouple response time in air," *Exp. Heat Transf.*, vol. 14, no. 2, pp. 107–118, 2001.

[26] Rittel, D., "Transient temperature measurement using embedded thermocouples," *Exp. Mech.*, vol. 38, no. 2, pp. 73–78, 1998.

[27] Kapoor, R. and Nemat-Nasser, S., "Determination of temperature rise during high strain rate deformation," *Mech. Mater.*, vol. 27, pp. 1–12, 1998.

[28] Gilat, A., Kuokkala, V.-T., Seidt, J. D., and Smith, J. L., "Full-Field Measurement of Strain and Temperature in Quasi-Static and Dynamic Tensile Tests on Stainless Steel 316L," *Procedia Eng.*, vol. 207, pp. 1994–1999, Jan. 2017.

[29] Guduru, P. R., Zehnder, A. T., Rosakis, A. J., and Ravichandran, G., "Dynamic full field measurements of crack tip temperatures," *Eng. Fract. Mech.*, vol. 68, no. 14, pp. 1535–1556, Sep. 2001.

[30] Zehnder, A. T. and Rosakis, A. J., "On the temperature distribution at the vicinity of dynamically propagating cracks in 4340 steel," *J. Mech. Phys. Solids*, vol. 39, no. 3, pp. 385–415, 1991.

[31] Zehnder, A. and Rosakis, A., "Temperature rise at the tip of dynamically propagating cracks: measurements using high-speed infrared detectors," *Exp. Tech. Fract.*, pp. 125–169, 1993.

[32] Guduru, P. R., Ravichandran, G., and Rosakis, A. J., "Observations of transient high temperature vortical microstructures in solids during adiabatic shear banding," *Phys. Rev. E - Stat. Physics, Plasmas, Fluids, Relat. Interdiscip. Top.*, vol. 64, no. 3, p. 6, 2001.

[33] Brübach, J., Pflitsch, C., Dreizler, A., and Atakan, B., "On surface temperature measurements with thermographic phosphors: A review," *Prog. Energy Combust. Sci.*, vol. 39, no. 1, pp. 37–60, Feb. 2013.

[34] Allison, S. W. and Gillies, G. T., "Remote thermometry with thermographic phosphors: Instrumentation and applications," *Rev. Sci. Instrum.*, vol. 68, no. 7, pp. 2615–2650, Jul. 1997.

[35] Ayers, Z. M., Fisher, J. M., Brown, A., Son, S. F., and Meyer, T. R., “KHz-rate temperature imaging using time-domain thermographic phosphorescence,” in *AIAA Scitech 2019 Forum*, 2019.

[36] Fonger, W. H. and Struck, C. W., “Eu+3 5D Resonance Quenching to the Charge-Transfer States in Y2O2S, La2O2S, and LaOCl,” *J. Chem. Phys.*, vol. 52, no. 12, pp. 6364–6372, Jun. 1970.

[37] Allison, S. W., Cates, M. R., Noel, B. W., and Gillies, G. T., “Monitoring permanent-magnet motor heating with phosphor thermometry,” *IEEE Trans. Instrum. Meas.*, vol. 37, no. 4, pp. 637–641, 1988.

[38] Tobin, K. W., Allison, S. W., Cates, M. R., Capps, G. J., and Beshears, D. L., “High-temperature phosphor thermometry of rotating turbine blades,” *AIAA J.*, vol. 28, no. 8, pp. 1485–1490, 1990.

[39] Noel, B. W., Borella, H. M., Lewis, W., Turley, W. D., Beshears, D. L., Capps, G. J., Cates, M. R., Muhs, J. D., and Tobin, K. W., “Evaluating thermographic phosphors in an operating turbine engine,” in *ASME 1990 International Gas Turbine and Aeroengine Congress and Exposition*, 1990, pp. 113–242.

[40] Feist, J. P., Heyes, A. L., and Seefelt, S., “Thermographic phosphor thermometry for film cooling studies in gas turbine combustors,” *Proc. Inst. Mech. Eng. Part A J. Power Energy*, vol. 217, no. 2, pp. 193–200, 2003.

[41] Husberg, T., Gjirja, S., Denbratt, I., Omrane, A., Aldén, M., and Engström, J., “Piston temperature measurement by use of thermographic phosphors and thermocouples in a heavy-duty diesel engine run under partly premixed conditions,” *SAE Tech. Pap.*, 2005.

[42] Brübach, J., Zetterberg, J., Omrane, A., Li, Z. S., Aldén, M., and Dreizler, A., “Determination of surface normal temperature gradients using thermographic phosphors and filtered Rayleigh scattering,” *Appl. Phys. B*, vol. 84, no. 3, p. 537, May 2006.

[43] Brübach, J., Van Veen, E., and Dreizler, A., “Combined phosphor and CARS thermometry at the wall–gas interface of impinging flame and jet systems,” *Exp. Fluids*, vol. 44, no. 6, p. 897, Dec. 2007.

[44] Fuyuto, T., Kronemayer, H., Lewerich, B., Brübach, J., Fujikawa, T., Akihama, K., Dreier, T., and Schulz, C., “Temperature and species measurement in a quenching boundary layer on a flat-flame burner,” *Exp. Fluids*, vol. 49, no. 4, pp. 783–795, Oct. 2010.

[45] Omrane, A., Ossler, F., and Aldén, M., “Two-dimensional surface temperature measurements of burning materials,” *Proc. Combust. Inst.*, vol. 29, no. 2, pp. 2653–2659, Jan. 2002.

[46] Omrane, A., Ossler, F., and Aldén, M., “Temperature measurements of combustible and non-combustible surfaces using laser induced phosphorescence,” *Exp. Therm. Fluid Sci.*, vol. 28, no. 7, pp. 669–676, Sep. 2004.

[47] Khalid, A. H. and Kontis, K., “2D surface thermal imaging using rise-time analysis from laser-induced luminescence phosphor thermometry,” *Meas. Sci. Technol.*, vol. 20, no. 2, p. 25305, 2009.

[48] Cundy, M., Trunk, P., Dreizler, A., and Sick, V., “Gas-phase toluene LIF temperature imaging near surfaces at 10 kHz,” *Exp. Fluids*, vol. 51, no. 5, pp. 1169–1176, Nov. 2011.

[49] Abram, C., Fond, B., Heyes, A. L., and Beyrau, F., “High-speed planar thermometry and velocimetry using thermographic phosphor particles,” *Appl. Phys. B Lasers Opt.*, vol. 111, no. 2, pp. 155–160, May 2013.

[50] Hudspeth, M., Claus, B., Dubelman, S., Black, J., Mondal, A., Parab, N., Funnell, C., Hai, F., Qi, M. L., Fezzaa, K., Luo, S. N., and Chen, W., “High speed synchrotron x-ray phase contrast imaging of dynamic material response to split Hopkinson bar loading,” in *Review of Scientific Instruments*, 2013, vol. 84, no. 2, p. 025102.

[51] Parab, N. D., Black, J. T., Claus, B., Hudspeth, M., Sun, J., Fezzaa, K., and Chen, W. W., “Observation of Crack Propagation in Glass Using X-ray Phase Contrast Imaging,” *Int. J. Appl. Glas. Sci.*, vol. 5, no. 4, pp. 363–373, Dec. 2014.

[52] Nie, Y., Parab, N. D., Chu, J. M., Kim, G., Sun, T., Fezzaa, K., Sterkenburg, R., and Chen, W. W., “Dynamic crack propagation from a circular defect in a unidirectional carbon fiber reinforced plastic composite,” *J. Compos. Mater.*, vol. 52, no. 25, pp. 3539–3547, Oct. 2018.

[53] Nie, Y., Claus, B., Gao, J., Zhai, X., Kedir, N., Chu, J. M., Sun, T., Fezzaa, K., and Chen, W. W., “In situ Observation of Adiabatic Shear Band Formation in Aluminum Alloys,” *Exp. Mech.*, pp. 1–11, 2019.

[54] Meyer, L. W., Staskewitsch, E., and Burblies, A., “Adiabatic shear failure under biaxial dynamic compression/ shear loading,” *Mech. Mater.*, vol. 17, no. 2–3, pp. 203–214, Mar. 1994.

[55] Hartmann, K. H., Kunze, H. D., and Meyer, L. W., “Metallurgical Effects on Impact Loaded Materials,” in *Shock Waves and High-Strain-Rate Phenomena in Metals: Concepts and Applications*, M. A. Meyers and L. E. Murr, Eds. Boston, MA: Springer US, 1981, pp. 325–337.

[56] Chen, R. W. and Vecchio, K. S., “Microstructural characterization of shear band formation in Al-Li alloys,” *Le J. Phys. IV*, vol. 4, no. C8, pp. C8–459, 1994.

[57] Beatty, J. H., Meyer, L. W., Meyers, M. A., and Nemat-Nasser, S., “Formation of controlled adiabatic shear bands in AISI 4340 high strength steel,” 1990.

[58] Meyers, M. A., Subhash, G., Kad, B. K., and Prasad, L., “Evolution of microstructure and shear-band formation in α-hcp titanium,” *Mech. Mater.*, vol. 17, no. 2–3, pp. 175–193, Mar. 1994.

[59] Xue, Q., “Spatial evolution of adiabatic shear localization in stainless steel, titanium, and titanium-aluminum-vanadium alloy.,” University of California, San Diego, 2001.

[60] Meyer, L. W. and Krüger, L., “Shear testing with hat specimen,” *ASM Handbook, Mech. Test. Eval. ASM Int. Mater. Park. Ohio*, vol. 8, pp. 451–452, 2000.

[61] Chen, W. W. and Song, B., *Split Hopkinson (Kolsky) bar: design, testing and applications*. Springer Science & Business Media, 2010.

[62] Wen, C.-D. and Mudawar, I., “Emissivity characteristics of polished aluminum alloy surfaces and assessment of multispectral radiation thermometry (MRT) emissivity models,” *Int. J. Heat Mass Transf.*, vol. 48, no. 7, pp. 1316–1329, Mar. 2005.

[63] Mills, K. C., *Recommended values of thermophysical properties for selected commercial alloys*. Woodhead Publishing, 2002.

[64] Särner, G., “Laser-induced emission techniques for concentration and temperature probing in combustion,” Lund University, 2008.

[65] Erasmus, L. J. B., Swart, H. C., Terblans, J. J., and Kroon, R. E., “Measuring the optical thermometry properties of La2O2S:Eu phosphor material,” in *Annual Conference of SA Institute of Physics*, 2015.

[66] Yen, W. M. and Yamamoto, H., *Fundamentals of phosphors*. CRC press, 2006.

[67] Huang, L. and El-Genk, M. S., “Thermal conductivity measurements of alumina powders and molded Min-K in vacuum,” *Energy Convers. Manag.*, vol. 42, no. 5, pp. 599–612, Mar. 2001.

[68] Jiang, M. Q. and Dai, L. H., “On the origin of shear banding instability in metallic glasses,” *J. Mech. Phys. Solids*, vol. 57, no. 8, pp. 1267–1292, Aug. 2009.

[69] Fond, B., Abram, C., and Beyrau, F., “Characterisation of the luminescence properties of BAM:Eu^{2+} particles as a tracer for thermographic particle image velocimetry,” *Appl. Phys. B*, vol. 121, no. 4, pp. 495–509, 2015.

[70] Sharma, P. K., Dutta, R. K., and Pandey, A. C., “Performance of YAG:Eu^{3+} , YAG:Tb^{3+} and BAM:Eu^{2+} plasma display nanophosphors,” *J. Nanoparticle Res.*, vol. 14, no. 3, p. 731, 2012.

PUBLICATIONS

Journal Articles

[1] **Nie, Y.**, Claus, B., Gao, J., Zhai, X., Kedir, N., Chu, J., Sun, T., Fezzaa, K. and Chen, W.W.,d In Situ Observation of Adiabatic Shear Band Formation in Aluminum Alloys. *Experimental Mechanics*, pp.1-11. (2019)

[2] **Nie, Y.**, Parab, N.D., Chu, J.M., Kim, G., Sun, T., Fezzaa, K., Sterkenburg, R. and Chen, W.W., Dynamic crack propagation from a circular defect in a unidirectional carbon fiber reinforced plastic composite. *Journal of Composite Materials*, *52*(25), pp.3539-3547. (2018)

[3] **Nie, Y.**, Liao, H. and Chen, W.W., Cyclic tensile response of a pre-tensioned polyurethane. *Mechanics of Time-Dependent Materials*, *22*(2), pp.207-219. (2018)

[4] Parab, N.D., Xiong, L., Guo, Q., Guo, Z., Kirk, C., **Nie, Y.**, Xiao, X., Fezzaa, K., Everheart, W., Chen, W.W. and Chen, L., Investigation of dynamic fracture behavior of additively manufactured Al-10Si-Mg using high-speed synchrotron X-ray imaging. *Additive Manufacturing*, *30*, p.100878. (2019)

[5] Zhai, X., Gao, J., **Nie, Y.**, Guo, Z., Kedir, N., Claus, B., Sun, T., Fezzaa, K., Xiao, X. and Chen, W.W., Real-time visualization of dynamic fractures in porcine bones and the loading-rate effect on their fracture toughness. *Journal of the Mechanics and Physics of Solids*, *131*, pp.358-371. (2019)

[6] Kirk, C.D., Parab, N.D., Kedir, N., Guo, Z., **Nie, Y.**, Paulson, S., Thomas, J., Fezzaa, K., Sun, T. and Chen, W., In-Situ Visualization of Tensile Failure in Additively Manufactured 316 L Stainless Steel. *Experimental Mechanics*, *59*(6), pp.805-818. (2019)

[7] Zhai, X., Guo, Z., Gao, J., Kedir, N., **Nie, Y.**, Claus, B., Sun, T., Xiao, X., Fezzaa, K. and Chen, W.W., High-speed X-ray visualization of dynamic crack initiation and propagation in bone. *Acta biomaterialia*, *90*, pp.278-286. (2019)

[8] Lim, B.H., Chu, J.M., Gao, J., Claus, B., **Nie, Y.** and Chen, W., The Effect of Projectile Nose Shape on the Critical Velocity of High-Performance Yarn. *Fibers*, *7*(4), p.29. (2019)

[9] Zhai, X., Nauman, E.A., **Nie, Y.**, Liao, H., Lycke, R.J. and Chen, W.W., Mechanical Response of Human Muscle at Intermediate Strain Rates. *Journal of biomechanical engineering*, *141*(4), p.044506. (2019)

[10] Gao, J., **Nie, Y.**, Lim, B.H., Kedir, N. and Chen, W., A Microscopic Experimental Method Transversely Loading on Single High-Performance Fibers. *Experimental Mechanics*, pp.1-11. (2019)

[11] Lim, B., Chu, J.M., Claus, B., **Nie, Y.** and Chen, W., Critical Velocity of High-Performance Yarn Transversely Impacted by Razor Blade. *Fibers*, *6*(4), p.95. (2018)

[12] Levine, S., **Nie, Y.** and Chen, W., Dynamic transverse debonding of a single fiber. *Journal of Dynamic Behavior of Materials*, *2*(4), pp.521-531. (2016)

Conference Proceedings

[1] **Nie, Y.**, Parab, N.D., Chu, J.M., Sun, T., Fezzaa, K., and Chen, W.W., Crack Propagation from a Circular Defect in a Unidirectional CFRP Composite under Dynamic Tension. In *Proceedings of the American Society for Composites—Thirty-second Technical Conference*. (2017)

[2] Gao, J., Guo, Z., **Nie, Y.**, Hernandez, J., Lim, B.H., Kedir, N., Tallman, T. and Chen, W., Transverse Impact on a Single Layer S-Glass/SC15 Epoxy Composite Strip. In *Proceedings of the American Society for Composites—Thirty-fourth Technical Conference*. (2019)